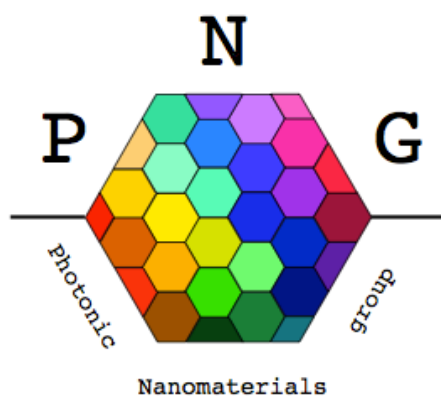


CONSTRUCTING A **P**ROBE **M**MAGNETOMETER USING **N**ITROGEN VACANCY CENTRES IN **N**ANODIAMOND

A Part II Thesis submitted for the Honour School of
Materials Science



University of Oxford

By Katherine Hazelton

Supervised by Dr Jason Smith

ACKNOWLEDGEMENTS

First and foremost I would like to thank my supervisor Dr Jason Smith, for his patience as I grasped the theory and practical work involved in this project, and for his invaluable advice throughout the course of the year. His recommendations for both lab work and in the writing of this thesis have been very helpful.

I am grateful to all members of the Photonic Nanomaterials Group, and in particular to Sam Johnson and Dr Phil Dolan, for sharing their knowledge on NV centres and practical experience in optics, and also for general go-to advice. Without them I would have run into some serious setbacks. Thanks to Dr Aurelien Trichet for his help on optics theory and setup alignment, and to Matthew Wincott, for his renowned ability in Labview programming. Alex Powell, Robin Patel and Lucas Flatten were great for lab sharing: working in darkness is a tough task for many. Thank you also to my fellow part II students, Laiyi Weng and Sarah Connolly.

Finally, I would like to acknowledge the Department of Materials, Oxford University, for giving me the opportunity to be regarded as a member of the research community as part of my undergraduate degree. It has been an incredible experience.

ABSTRACT

In this thesis, adhesion of a 200nm detonation nanodiamond to a 4 μ m optical fiber core is proved to be a viable method of creating a probe magnetometer. The spin triplet state of the negatively charged nitrogen vacancy centre in diamond is sensitive to local magnetic fields. A change in field may be read-out as a change in photoluminescence intensity.

A confocal setup with scanning piezo stage is constructed and optimized using a Ronchi grating. Collection of photoluminescence from a CdSe quantum dot confirms the feasibility of fiber excitation and fluorescence collection. A single 200nm nanodiamond is located and a spectrum from an ensemble of nitrogen vacancy centres within the nanodiamond taken by precise positioning of the fiber with respect to the scanning stage. The sample preparation process is developed for precise and robust adhesion of nanodiamond to fiber. A PMMA layer between nanodiamond and coverslip may be removed by dissolution after curing optically- transparent UV-curing adhesive. Repeat measurements confirm the reproducibility of this method.

A probe magnetometer is characterised. DC magnetic field sensitivity is calculated to be 7.16mTHz^{-1/2} when using photoluminescence quenching as a sensing technique. Resolution is achieved on the micrometer scale. Images of magnetic tracks in a commercial hard disk platter with 4 μ m spacing were taken. Resolutions beyond this limit are restricted by excess epoxy present on the probe tip.

Whilst higher sensitivities and resolutions are yet to be achieved, a probe magnetometer has been successfully constructed, opening up a wider range of potential magnetic sensing applications in the biomedical and materials sciences.

CONTENTS

1. INTRODUCTION	5
1.1 PROJECT OVERVIEW	5
1.2 BACKGROUND THEORY: THE NITROGEN VACANCY DEFECT IN DIAMOND	6
NV ⁰	7
NV ⁻	8
SPIN MANIPULATION	10
APPLICATION OF A MAGNETIC FIELD	10
SINGLE PHOTON EMISSION	12
1.3 ENGINEERING CONTEXT	13
2. LITERATURE REVIEW	14
2.1 HISTORY OF OPTICAL MAGNETOMETRY	14
2.2 NV-BASED ATOMIC FORCE MICROSCOPE	15
2.3 FIBER METHODS	17
2.4 NV ENSEMBLES	20
2.5 ALL-OPTICAL IMAGING OF MAGNETIC FIELDS	21
2.6 CONCLUSION	23
3. OPTICAL SETUP	24
3.1 BENCH SETUP	24
3.2 SPECTROSCOPY	27
3.3 FIBER CHARACTERISATION	29
3.4 ALTERNATIVE FIBERS	31
3.5 POLARISATION EFFECTS	34
4. PHOTOLUMINESCENCE IMAGING OF NANODIAMOND	36
4.1 SCANNED IMAGING	36
4.2 IMAGING PHOTOLUMINESCENCE	38
4.3 VARYING NANODIAMOND CONCENTRATION	39
4.4 STUDYING AN INDIVIDUAL NANODIAMOND	41
5. THE MAKING OF A PROBE MAGNETOMETER	44
5.1 FIBER CLEAVING	44
5.2 UV CURING ADHESIVE	46
5.3 PROBE CHARACTERISATION	49
6. MAGNETIC FIELD SENSING	51
6.1 QUENCHING PHOTOLUMINESCENCE	51
6.2 MAGNETIC FIELD DEPENDENCE	52
6.3 HARD DISK IMAGING	57
7. CONCLUSIONS AND FUTURE WORK	63
PROJECT MANAGEMENT	71
APPENDICES A- ACRONYMS, B- LABVIEW PROGRAMMING, C- ERROR ANALYSIS, D- LASER CALIBRATION, E- ELECTROMAGNET CALIBRATION	75

1. INTRODUCTION

1.1 PROJECT OVERVIEW

Diamond is a material that has been admired for centuries for its crystal perfection. Its superlative properties, including high hardness, high thermal conductivity, high melting point, good chemical stability and optical transparency make it an attractive material of choice. However, it is diamond's crystallographic imperfections that have generated a recent surge in scientific research, for potential use in fields including quantum computing, bioscience and magnetometry.

To-date, the nitrogen vacancy (NV) defect has been extensively studied. Its remarkable optical and spin properties are now looking to be exploited for uses in future technologies.

The end target of this project was to create a nanoscale probe magnetometer for imaging magnetic fields. Creating a probe method of magnetic field sensing opens up many new potential applications due to its flexibility and portability in comparison to current instruments.

As an ultimate goal of the project, a single NV centre in nanodiamond would be attached to an optical fiber to act as a highly sensitive nanoscale magnetometer. This could then image weak magnetic fields with nanometer spatial resolution at ambient conditions.

The principal milestones of the project were to setup the optics required and detect the photoluminescence signal through the fiber from a single nanodiamond. The nanodiamond would then be attached to the fiber, and finally be used to detect and image spatial magnetic field variation. This thesis is broken up into 7 chapters, with the first providing an introduction to NV defects, and the second a review of current literature. Chapters 3 to 6 give details of my optical setup and characterisation, nanodiamond adhesion process and probe magnetic field sensing. Finally chapter 7 concludes and discusses potential future research opportunities in this field.

1.2 BACKGROUND THEORY: THE NITROGEN VACANCY DEFECT IN DIAMOND

The superlative properties of diamond such as high thermal conductivity, chemical inertness and hardness are attributed to a covalent lattice of tetrahedrally bonded carbon atoms. Some of these properties are listed in the table below.

Physical Property	Value
Hardness	10,000 kgmm ⁻²
Thermal Conductivity	20Wcm ⁻¹ K ⁻¹
Thermal Expansion Coefficient	0.0000011K ⁻¹
Optical Index of Refraction	2.41
Optical Transmissivity	225
Tensile Strength	>1.2GPa

Table 1.2.1 Physical Properties of diamond¹

However next generation technologies using diamond such as quantum computing, spintronics and nanoscale magnetometry rely on the presence of crystal defects in the lattice. Diamond's large electronic band gap (5.5eV) accommodates for a wide variety of optically active defects.² Of over 500 discovered, one of the most common and well-researched colour centres is the nitrogen vacancy (NV) defect.

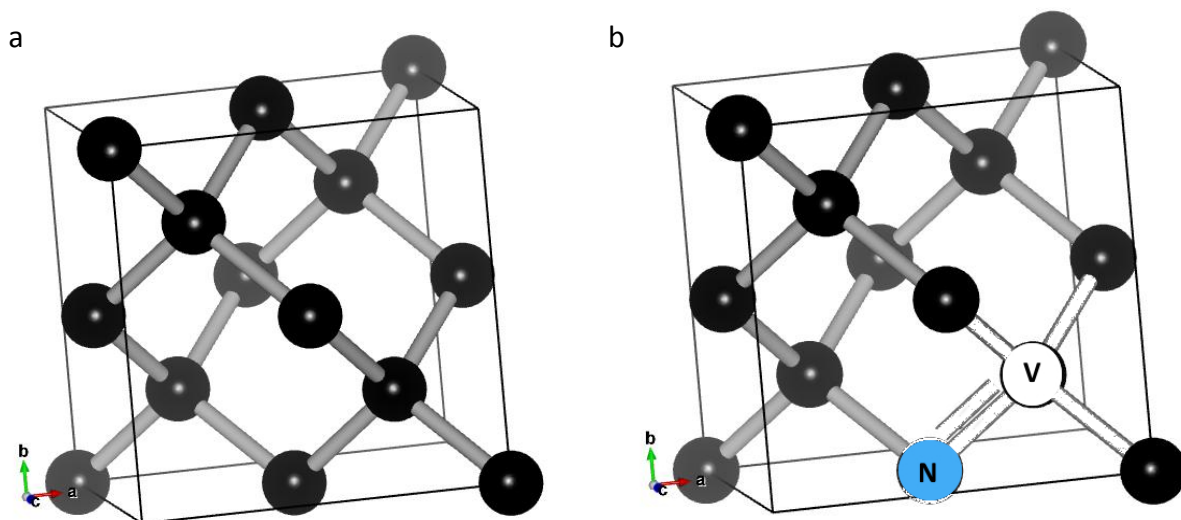


Figure 1.2.1 a) Diamond crystal structure based on an fcc lattice with atoms at 000 and $\frac{a}{4} \frac{a}{4} \frac{a}{4}$ where a is lattice constant³ 0.357nm b) the nitrogen vacancy defect lies along the (111) plane, with axial directions $z:[111]$, $x:[-1-12]$, $y:[1-10]$

Discovered in 1976 by Davies⁴, the nitrogen vacancy centre in diamond consists of a single substitutional nitrogen atom bonded to three neighbouring carbon atoms. An adjacent vacancy is joined to the nitrogen along the (111) atomic plane, as shown in figure 1.2.1, giving the defect C_{3v} symmetry.⁵

Nitrogen vacancy defects occur naturally, or may be artificially engineered in diamond. They may be included in the diamond bulk by chemical vapour deposition (CVD)^{6,7}, high temperature high pressure (HPHT) synthesis⁸, irradiation⁹, or ion implantation¹⁰. Each of these techniques has its advantages and disadvantages; the diamond synthesis process must be selected depending on the desired application. For instance, ion implantation positions the NV centre with sub micron accuracy, yet HPHT is the least costly method¹¹. Nitrogen vacancy centres are multiplied in artificial diamond by annealing for several hours at raised temperature in a vacuum. Carbon vacancies are created which diffuse through the sample combining with nitrogen impurities.¹²

Detonation of carbon based explosives trinitrotoluene (TNT) and hexogen (RDX) inside a metal chamber creates diamond crystals due to the high pressure (20-30GPa) and high temperature (3000-4000K).¹³ These conditions exist for a limited time, so the crystals are sub-micron in size; nanodiamond.¹⁴ Nanodiamonds can be made as small as 5nm in diameter. The residue from the explosion must be filtered to give agglomerates of nanodiamond. Sonication breaks up the nanodiamond clusters, hence a variety of sizes of particles may be obtained depending on extent of disaggregation. There is no refraction of light at the nanodiamond-air interface, so light collection efficiency is greatly improved¹⁵. When considering diamond's high refractive index, $n=2.42$, this is a factor which must be taken into account.

NV⁰

The nitrogen vacancy centre is commonly encountered in one of two possible charge states.⁹ The neutral defect NV⁰ has five unsatisfied active bonding electrons associated with it: three sp^3 electrons from the neighbouring carbon atoms, and two from the adjacent nitrogen atom. The electron wavefunctions are highly localised around the defect and hence one may consider the NV as an artificial atom within the diamond host lattice. NV⁰ ground state

electrons may be excited by light with sufficient energy, which subsequently relax producing photoluminescence (PL). Due to the large 5.5eV band gap in diamond, the PL emission is in the optical wavelength range. The spectrum for NV^0 is shown in figure 1.2.3, with a zero phonon line (ZPL) at 575nm.

NV⁻

The other common charge state is the negatively charged centre, NV^- . An additional electron is associated with the defect, originating from elsewhere in the diamond lattice.¹⁶ This additional electron provides the defect with $S=1$ state, allowing for a spin triplet state where the defect's neutral form possesses a spin doublet equivalent. It is the splitting of the spin triplet state that provides potential application in magnetometry. Application of a microwave field of 2.88GHz splits the triplet ground state into singlet $m_s=0$ and doublet $m_s=\pm 1$ states.¹⁷ m_s here denotes the spin projection along the intrinsic quantisation axis of the NV defect corresponding to the [111] crystal axis. The excited state 3E may be split with a microwave field of 1.42GHz.¹⁸

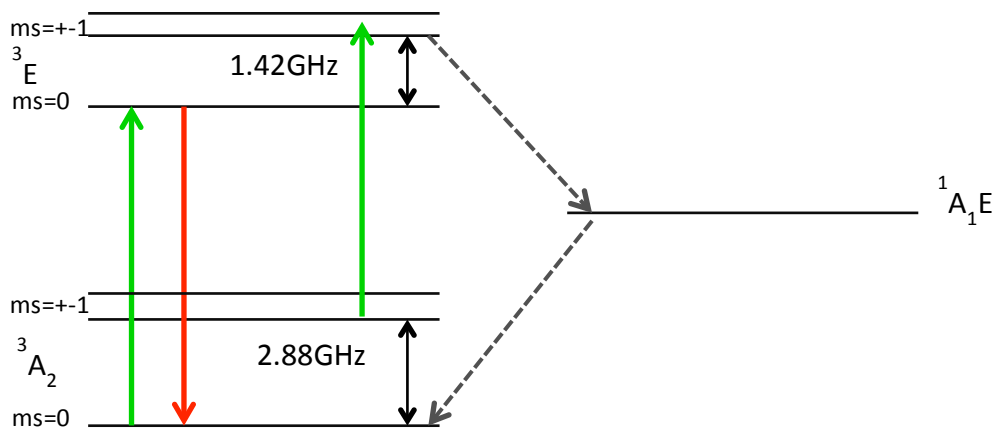


Figure 1.2.2 Simplified 7-level electronic system of the NV defect. Green arrows denote excitation light, red photoluminescence and dotted grey the non-radiative ISC. 3A_2 is the electron ground state, 3E the excited state and 1A_1E the intermediate singlet state

Excitation of an electron from 3A_2 into 3E by laser light causes radiative relaxation with broad red photoluminescence (figure 1.2.3).

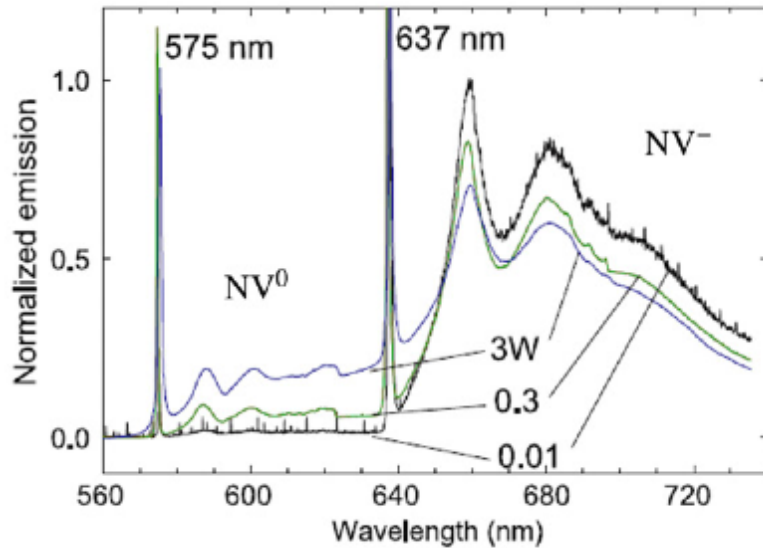


Figure 1.2.3, Spectrum of the NV^0 and NV^- defects; ZPL are 575nm and 637nm respectively. The three lines correspond to different 532nm excitation powers. Data was taken at 10K for sharpened spectral features¹⁹

The PL spectrum exhibits a zero phonon line at 1.945eV ($\lambda=637\text{nm}$). This line is broadened across higher wavelengths at higher temperatures due to the relaxation of electrons through vibrational states before reaching the final ground state (figure 1.2.4). These vibrational states are known as phonon side bands (PSBs). This bright PL signal has seen NV centres in nanodiamond used as fluorescent biomarkers in cells.^{20,21,22}

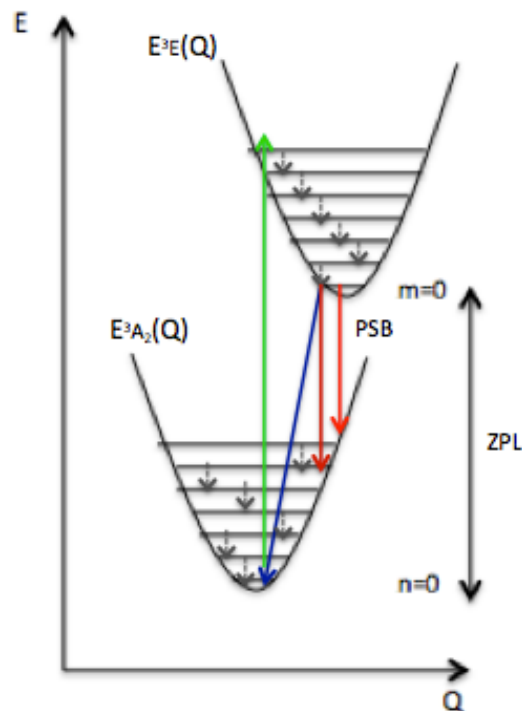


Figure 1.2.4 depicts the phonon energies with phonon ground states at $n=0$ and $m=0$ in the ground and excited states respectively. The most probable optical transitions are vertical, resulting in relaxation via PSBs, producing a broad range of emission wavelengths²³

Spin Manipulation

Alternatively the electron may relax via an intersystem crossing (ISC). Intermediate spin singlet energy levels provide a non-radiative relaxation path. This path is highly spin selective. Electrons in the $m_s=\pm 1$ and $m_s=0$ state have a 30% and a 0.01% probability of entering an intermediate state respectively. Eventually the electron relaxes into the $m_s=0$ ground state. Over sufficient time total electron population is in the $m_s=0$ ground state, such that a high level of photon emission is seen; a laser optically pumps the system. This enables room temperature spin read out of the NV in quantum computing applications.²⁴ In magnetometry a resonant microwave field is applied to prevent all the population remaining in $m_s=0$. This field promotes electrons from the $m_s=0$ into the $m_s=\pm 1$ spin state. Optical transitions conserve spin. Hence a 30% dip in photoluminescence is seen upon excitation of the NV defect.²⁵

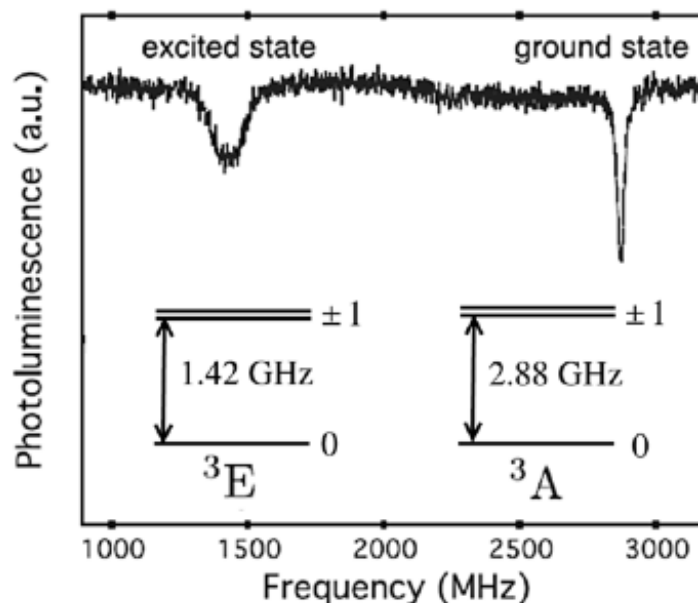


Figure 1.2.5 A dip in photoluminescence is noted at both 2.88GHz and 1.88GHz, representing the splitting of the 3A and 3E $m_s=\pm 1$ and $m_s=0$ spin states respectively²⁵

Application of a magnetic field

The presence of a magnetic field lifts the degeneracy of the $m_s=\pm 1$ spin sublevels. This phenomenon is known as the Zeeman effect.²⁸ The extent of the sublevel splitting is linearly proportional to the magnetic field strength (fig 1.2.6) provided the field acts along the NV

axis. Therefore the field magnitude may be measured by scanning microwave radiation across a range of frequencies ω (fig 1.2.7).

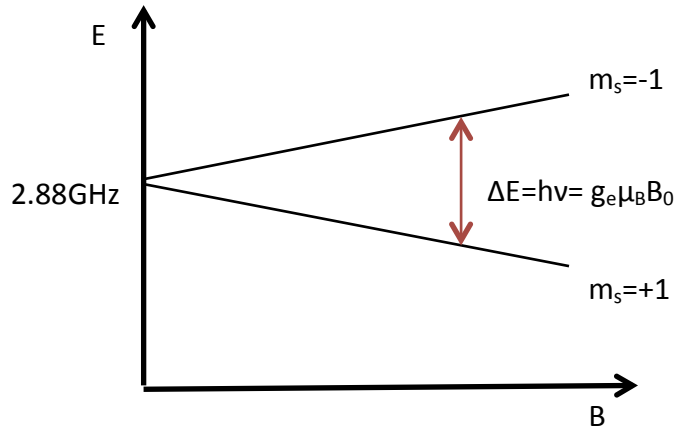


Figure 1.2.6 Zeeman splitting observed on application of an external magnetic field B_0 . Provided the field is applied perpendicular to the z-axis of the NV centre, there is a linear relationship between field strength and the change in energy ΔE ^{26,43}

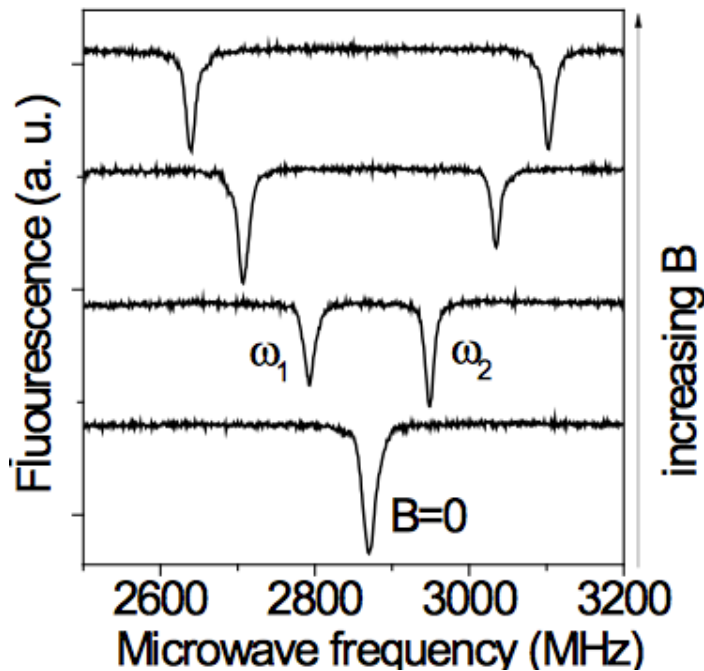


Figure 1.2.7 PL dips corresponding to $m_s = -1$ and $m_s = +1$ energies. The dip energy separation increases linearly with field strength B ²⁷

The sensitivity of the field measurement is controlled by the linewidth, which may be improved by using low optical excitation power and ensuring the NV z-axis is fully aligned perpendicular to the magnetic field.

Neglecting electron-spin interactions with nearby nuclear spins from the diamond lattice and assuming a perpendicular applied magnetic field, B_0 , a ground state Hamiltonian H_{NV} describes the system²⁸:

$$H_{NV} = D_{gs} S_z^2 + g_e \mu_B B_0 \cdot S$$

The ground state splitting energy at zero field $D_{gs} = 2.88 \text{ GHz}$, the electronic g factor $g_e = 2.00232$ ²⁹, μ_B is the Bohr magneton and S the NV spin matrix. Diagonalisation of the spin Hamiltonian identifies the eigenenergies of the possible spin states $m_s = 0, +1, -1$.³⁰

At higher magnetic fields, the electron spin states are randomised. This occurs in both ground and excited state levels, and in doing so increases the probability of non-radiative ISCs. This is also known to cause a 30% decrease in the rate of photoluminescence, and is used as an alternative form of magnetic field sensing without application of a microwave field (see section 2.5).⁶²

Single Photon Emission

The NV centre has to-date been the only paramagnetic system to be detected optically as a single emitter: emitting one photon per excitation pulse. Other paramagnetic defect centres are known, but have lower oscillation strength and/or multiple metastable states, thereby lowering the fluorescence emission.³¹ Through spin manipulation and detection as a single emitter, a plethora of uses for the NV defect are possible. These include sensing time-dependent magnetic fields, quantum devices and solid-state spintronics. For the purpose of this thesis I shall be focusing on the field of magnetometry.

1.3 ENGINEERING CONTEXT

The study of magnetic fields, or magnetometry, is a very expansive topic. Magnetic fields may be oscillating or constant, and may range in magnitude from a few femtotesla to hundreds of tesla. Current methods of sensing include using the Hall effect in semiconductors³², atomic vapour magnetometry³³, magnetic force resonance microscopy (MFRM)³⁶ and superconducting quantum interference in SQUIDs.³⁴

Nanoscale magnetic fields exist in the human brain and heart, and in high temperature superconductors. High-temperature superconductors eject weak external magnetic fields when operating. This is known as the Meissner effect. To better our understanding of this physical phenomenon, a high-resolution method of sensing weak magnetic fields on the nanoscale is required.

Conventional nanoscale magnetometry techniques are limited by their inability to function in ambient conditions when imaging on the nanoscale. SQUIDs and MRFMs offer nanoscale resolution but must be operated at cryogenic temperatures. This makes them bulky and complex to use. Hall probes and gaussmeters offer flexibility and operation at room temperature, yet their resolution goes down to only the millimetre scale. Much higher resolution and magnetic field sensitivity may be obtained by taking advantage of quantum phenomena occurring in the NV centre in diamond. Because the NV defect is a single photon emitter and an atomic scale defect, nanoscale resolution is possible. Under laser excitation and photon detection, NV photoluminescence allows direct field strength measurement. With the advancement of laser diode manufacture and the artificial manufacture of diamond, this approach could also prove more economical than conventional methods employed.

Diamond's non-toxicity and chemical- and photo- stability make it suitable for extended instrument use. By adhering an NV containing nanodiamond to an optical fiber we obtain a non-invasive technique for potential study of individual molecules in the biological sciences, and a robust research instrument available to materials scientists involved in the study of nanoscale magnetic fields.

2. LITERATURE REVIEW

2.1 HISTORY OF OPTICAL MAGNETOMETRY

Conventional light microscopy as founded by Abbe and Rayleigh in the late 1800s is resolution-limited by the diffraction of light at the objective lens and at the specimen surface when under far-field study.³⁵ In practical terms this means that only objects down to several hundred nanometers in size may be resolved.

As a means to overcome the theoretical resolution limit set by conventional techniques, magnetic resonance imaging (MRI) was proposed. The magnetic spin vectors in atoms are deflected by the introduction of a resonant microwave field when a high enough magnetic field is held. Since the resolution is now controlled by the strength of the magnetic field, it should go well below the optical wavelength. However, the resolution of this technique is often restricted down to only the micrometer range due to high signal-to-noise affects.

Then in 1991, magnetic resonance force microscopy (MRFM) was described by Sidles.³⁶ It combined principles of both MRI and atomic force microscopy (AFM) by using a ferromagnetic-tipped cantilever to detect changes in force between sample and tip. The first experiment was performed in 1992, and magnetic imaging in 1996.³⁷ High spatial resolution of the order of 25nm has been achieved. Whilst this is remarkable, a significant limitation to this method is the cryogenic temperatures required for high resolution, and when used at room temperature the sample itself experiences perturbations in magnetic field.^{38,39} This renders it inappropriate for wide scale medical and materials applications.

The discovery of optically detected magnetic resonance (ODMR) was in 1952 by Brossel and Bitter⁴⁰, however it was only in 2005 that Chernobrod and Berman proposed a fluorescent nanoprobe be implanted on the tip of either an AFM cantilever or an optical fiber (see figure 2.1.1).⁴¹ Stable at room temperature, the NV centre in diamond is a suitable candidate for high resolution magnetometry. The magnetic field from a single electron spin has been imaged by a NV-containing diamond nanopillar attached to an AFM tip: the ultimate benchmark for nanoscale sensing.⁴²

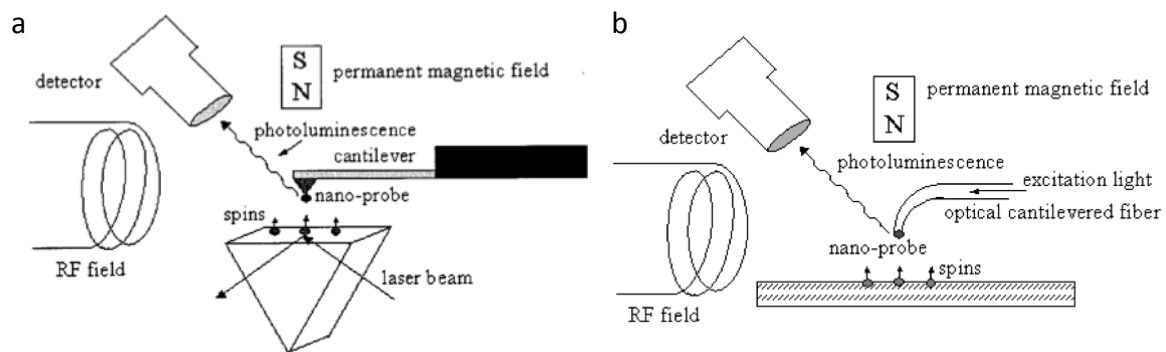


Figure 2.1.1 Principle of an NV ODMR-based magnetometer a) AFM- and b) fiber- based methods⁴¹

2.2 NV-BASED ATOMIC FORCE MICROSCOPE

In 2008 Taylor *et al.* proposed the use of NV centres in magnetometry. Both a high sensitivity magnetometer incorporating multiple NVs in bulk diamond and a nanometer resolution magnetometer containing a single NV centre were proposed.⁴³ As an adaptation of MRFM, an NV-containing nanodiamond is grafted onto the apex of an AFM tip and brought in close proximity to the sample. In that same year Balasubramanian imaged a magnetic sample using a single NV centre. Initially varying the proximity of a magnetic probe relative to the nanocrystal imaged the magnetic resonance of an NV centre. A confocal microscope setup collected the fluorescence and a 2D image was generated with each pixel corresponding to a well-defined magnetic field value. This method located the exact position and orientation of the NV centre in the crystal, such that it could then be attached to a probe tip using UV-curing adhesive (fig 2.2.1).²⁷ This same methodology and setup may be applied to a fiber magnetometer, with the distinct advantage of the fiber offering flexibility that the AFM does not possess.

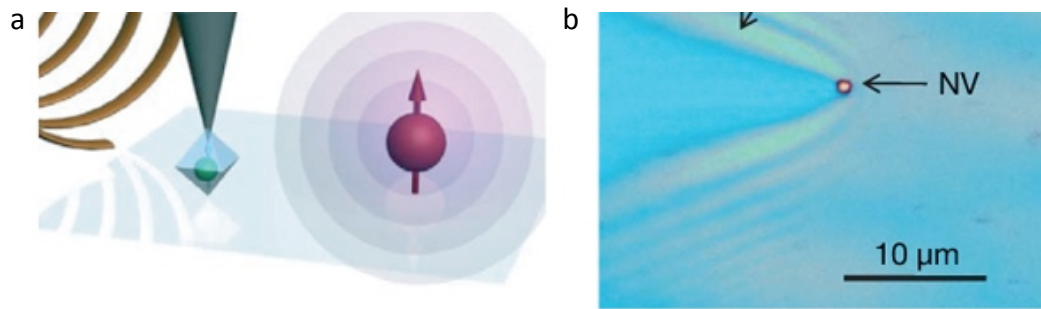


Figure 2.2.1 a) NV orientation, and b) an optical image taken of the AFM tip²⁷

For ODMR to be recorded, the NV axis must be orientated perpendicular to the external alternating magnetic field. An antenna applied a microwave field and a nickel magnetic nanostructure was imaged using the NV-adhered cantilever (fig 2.2.2). The magnetic field resonance resolution was measured to be 0.5mT.

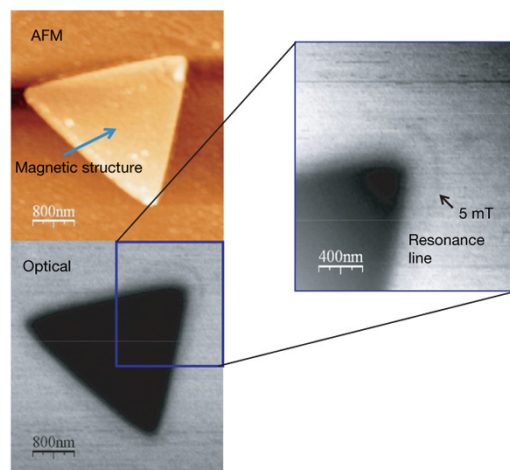


Figure 2.2.2 top left: AFM image of the nickel magnetic nanostructure, and bottom left: corresponding magneto-optical image using a single NV- AFM tip. The inset, right, shows the 5mT line present due to the drop in fluorescence when resonant microwaves are applied to the NV centre²⁷

Following Balasubramanian's work on the NV-integrated AFM cantilever, further work was carried out in the synthesis of diamond used to act as an effective cantilever tip, in order to improve magnetometer sensitivity. NV-containing diamond was grown into a nanopillar by electron lithography on a diamond membrane (see figure 2.2.3). Nanopillars possess the stability of bulk diamond whilst acting as an efficient waveguide for fluorescence emission.⁴⁴

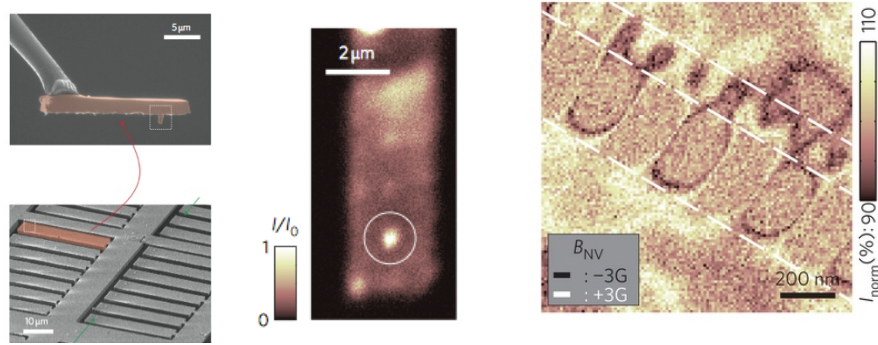


Figure 2.2.3 a diamond nanopillar containing a single NV at the tip is adhered to an AFM cantilever. Strips of magnetic bits were imaged on a commercial hard disk with 170nm and 65nm spacing with excitation power 130 μ W and 50ms acquisition time per pixel.⁴⁵

A magnetic hard disk with alternating out of plane magnetization was imaged (above), and sensitivities of 56nT $\text{Hz}^{-1/2}$ achieved. The resolution of the image is dependent on the proximity of the NV centre to the magnetic sample, which is difficult to consistently achieve in a nanopillar. In contrast, nanodiamond contains NVs very close to the surface such that nanometer scale sample-NV distances may be achieved.

An NV-AFM probe has the distinct advantage over a fiber-probe in that AFM is already a well-established instrument with known sample-tip distance and nano-positioning control, enabling accurate nanoscale magnetic field measurement. However, bulky external excitation and collection optics are required, which must remain in close proximity to the probe tip. A fiber integrates the optics such that it is flexible and manoeuvrable. In doing so, the fiber probe has potential to be used in many different environments; room and extreme temperatures, and on rough surfaces.

2.3 FIBER METHODS

In 2008 a fiber NV based magnetometer was proposed, with integrated collection and excitation⁴⁶. Several years previous Kuhn *et al.* adhered a nanodiamond to an optical fiber for use in scanning near field optical microscopy (SNOM)⁴⁷. SNOM overcomes the limit of diffraction by using a small aperture to illuminate the sample. A fluorescing particle was detected by a tapered optical fiber. A positively charged polymer (polyethylenimine) attached the NV containing nanodiamond to the fiber tip. PL is collected through an objective lens beneath the nanodiamond (figure 2.3.1). Cuche *et al.* developed this idea,

using a single NV- in nanodiamond.⁴⁸ He repeated experiments demonstrating the viability of using multiple nanodiamonds.⁴⁹ Any contact force on the tip resulted in the captured nanodiamond being released; hence, tuning fork is used to determine sample-proximity.⁵⁰ By using UV-curing adhesive a more robust instrument for magnetometry may be made.

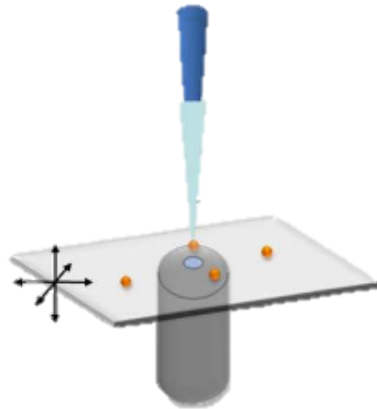


Figure 2.3.1 the fiber-sample configuration used. The excitation beam is passed along the fiber, and photoluminescence collected by an objective lens⁴⁹

A CVD method of implanting diamond on single mode optical fiber bundles was performed. Excitation was incident on the nanodiamond from an objective lens, and photoluminescence collected through the fiber, indicating strong mode coupling. Excitation light was also transmitted through the fiber and PL collected by a lens from the nanodiamond end. A fluorescence spectrum from a bare fused-silica fiber was included for comparison (figure 2.3.2).⁶

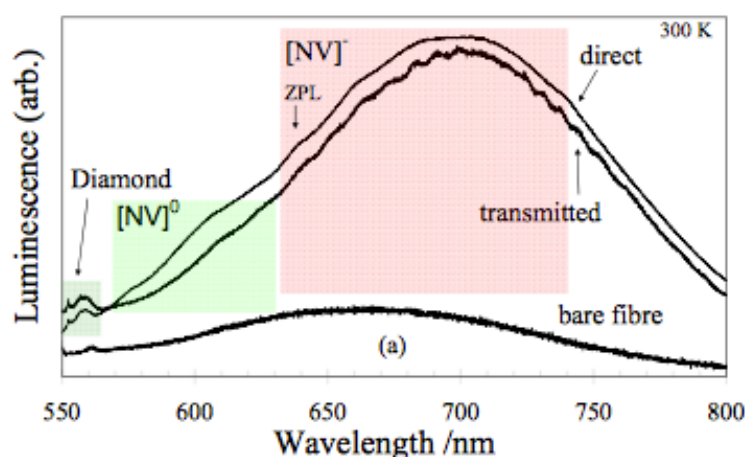


Figure 2.3.2 Spectra of transmitted and direct NV PL, compared to the bare fiber spectra⁶

Schroeder *et al.* attached a single NV centre in nanodiamond to a photonic crystal fiber by a ‘pick and place’ technique using an AFM.⁵¹ Nanodiamonds in a solution of water and 0.02%

PVA were spin coated at 2500RPM onto a coverslip. Repeated pressing of the AFM tip with a force of $0.1\mu\text{N}$ picked up the nanodiamond. He also reported a background signal from impurities and inelastic scattering from the fiber itself (see figure 2.3.3 and 2.3.4).

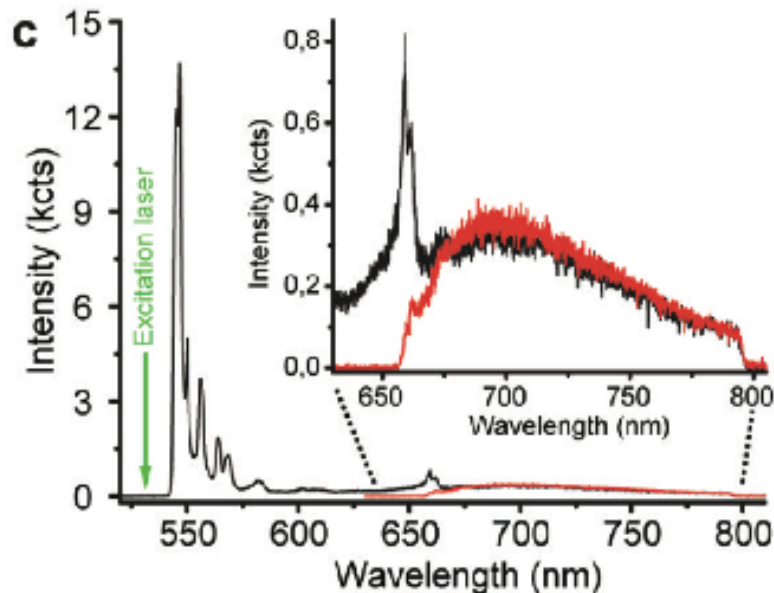


Figure 2.3.3 Background signal reported from impurities and inelastic Raman scattering from the fiber itself (black line). This was suppressed by spectral filtering using a 670nm long pass filter (red line).⁵¹

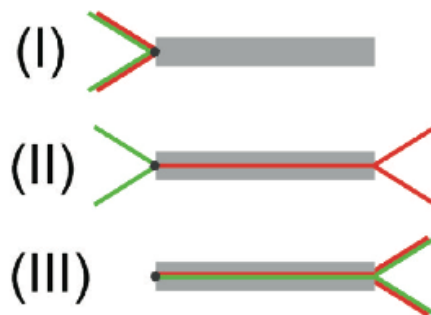


Figure 2.3.4 Fiber excitation and fluorescence collection configurations. Schroder reported fluorescence images for configurations II and I. Configuration III is only achieved with pulsed excitation and temporal filtering. The data was post-processed to imitate gating with an offset of 3.5ns to suppress background fluorescence in order to determine the nanodiamond as a single photon source.⁵¹

Tapering of a thorlabs 630HP optical fiber and dilute nanodiamond solution deposited on the tapered region is the final fiber configuration to discuss⁵². Excitation light is incident on the fiber from an objective lens perpendicular to the tapered region. The photoluminescence is collected along the fiber from the nanodiamond efficiently because of tapering the width to below half the wavelength of emitted light. This fiber configuration

would be inappropriate for magnetometry due to difficulty obtaining a short sample-to-NV distance, because of the random positioning of nanodiamond by solution deposition method. The orientation of the setup with objective lens and fiber is also unfavourable. A probe method with nanodiamond attached to the distal end is most suitable for magnetometry, however the reported background signal from excitation light in the fiber raises the question of whether the signal from a single NV will be strong enough for detection through the fiber.

2.4 NV ENSEMBLES

A high signal-to-noise magnetometer involving a slab of bulk diamond with multiple NVs connected to a Charge Coupled Device (CCD) was created. Vector reconstruction from each pixel in the CCD produces an image, recording pixel sensitivities of $\sim 100 \text{ nT Hz}^{-1/2}$. AC magnetic fields were recorded also, and the possibility of studying neural activity proposed.⁵³ By having n NV centres present, the sensitivity of the probe increases by a factor of $\frac{1}{\sqrt{n}}$, because of higher projection noise per unit volume, provided the magnetic field is homogenous over the magnetometer area. As a result, shorter integration times may be used, and faster magnetic field read-out is achievable. Layers of NVs are incorporated into 'slabs' of bulk diamond by ion implantation of nitrogen and subsequent annealing to combine nitrogen with vacancies⁵⁴. Annealing detonation nanodiamond produces an ensemble of NVs to give brighter emission, thus improving the probability of detection via optical fiber regardless of autofluorescence intensity.

The ultimate sensitivity is compromised by spin-spin interactions from C_{13} and paramagnetic impurities, which are relatively simple to remove from bulk diamond.⁴³ The minimum detectable field^{55,56}

$$\delta B_{min} = \frac{1}{g_s \mu_B} \frac{1}{R \sqrt{\eta}} \frac{1}{\sqrt{ntT_2}}$$

where R is the measurement contrast, η is sensitivity, t is integration time and T_2 the spin coherence time. Measurement contrast is largely affected by noise from the setup, and must

be maximised for smallest possible δB_{\min} . Noise may originate from the fiber itself, or from background counts and laser light fluctuations.

Spin coherence times were recently extended in nanodiamond by controlling the nitrogen concentration by milling HPHT diamond, such that spin-spin interactions between neighbouring NVs were reduced.⁵⁷ Higher sensitivities and resolutions are attainable in nanodiamond than initially recorded, making it an appropriate form of diamond for magnetic sensing application.⁵⁸

2.5 ALL-OPTICAL IMAGING OF MAGNETIC FIELDS

Any off axis fields cause spin mixing and dramatically reduce the contrast of the ODMR signal.³⁸ An ensemble of NVs having various axial orientations will reduce contrast to below the detection limit. However PL from an ensemble of NVs may be necessary to overcome potentially high fiber autofluorescence. As mentioned at the end of section 1.2, an increase in the magnetic field strength in an ensemble of NVs causes a randomisation of the spin state, lowering PL by 30% in a single NV centre.⁵⁹ Recently all-optical imaging has been realised as a potential technique that may be used for sensing large DC magnetic fields.²⁸ I chose to use this method for its relative simplicity (no microwave fields are necessary) and for a higher signal contrast in an NV ensemble than would be achieved using ODMR techniques.

Approximately 10% of the PL signal from an ensemble of NVs is quenched by a high magnetic field because the quenching largely affects just one of the four NV axial orientations.⁶⁰ At lower field strengths, less of the signal is quenched: spin mixing is a gradual effect (fig 2.5.1). For a single NV, At 50mT and 105.8mT the excited and ground state triplets are degenerate, hence spin polarisation is no longer effective and a large dip in PL occurs.⁶¹ In the case of multiple NVs in a single nanodiamond, these deviations from saturation should not be detectable because of the misalignment of the field with respect to NV axes. As a result, a gradual slope that reaches and remains at saturation is predicted with magnetic field strength increase.

Magnetic bits and tracks in a commercial hard disk were imaged using a single NV in 20nm nanodiamond attached to an AFM tip and PL collected via objective lens (fig 2.5.2). Two opposing bit magnetisations produce a stray field coming out at the boundary. Note that the maximum contrast in PL counts is 23%. Use of a scanning stage and fiber probe should give similar results, however with larger nanodiamond sizes, poorer resolution is to be expected.

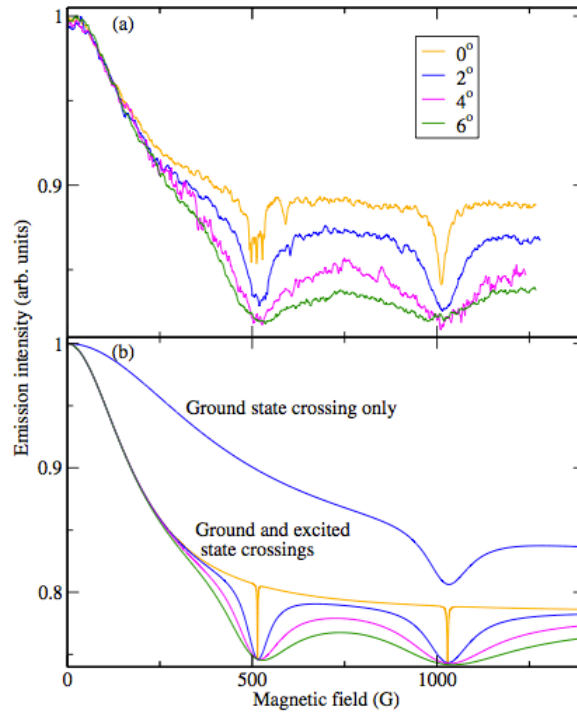


Figure 2.5.1 (a) Experimental variation of emission intensity vs magnetic field strength and (b) calculated dependence, taken for different misalignment angles with the NV axis.⁶⁰

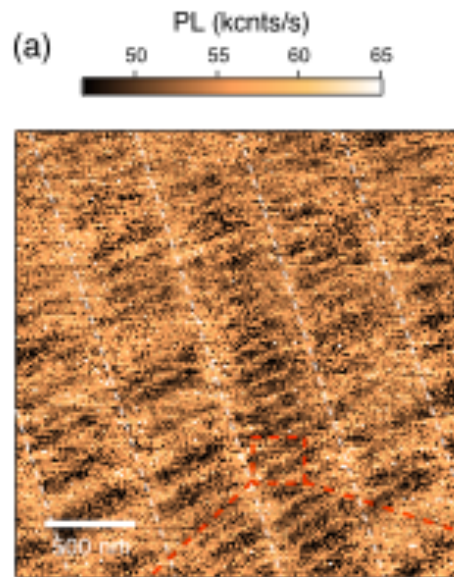


Figure 2.5.2 All-optical magnetic 300x300 pixel image of a hard disk. White lines correspond to 450nm-wide tracks. Continuous wave excitation was used. 8nm pixel size and 20ms acquisition time⁶²

2.6 CONCLUSION

Many different forms of diamond containing NV centres have been used to image magnetic fields, and different sensing techniques adopted. However there is still the challenge of creating a both robust and flexible method for magnetometry. There is no record of a probe magnetometer with simultaneous transmission of excitation and collection light. Different methods have been used to adhere nanodiamond to AFM tips for magnetometry, and to optical fibers for SNOM application.

An autofluorescence signal produced by optical fibers has been reported, however photoluminescence has been successfully coupled into an optical fiber. An ensemble of NVs generates a higher signal, which should overcome this high background signal. Use of an individual nanodiamond provides high spatial resolution. Such resolution may be maintained by light transmission through a single mode optical fiber. Nanodiamond sensitivities may be improved by extending spin coherence times to values comparable to bulk diamond. Fields may be sensed using the nitrogen vacancy centre using ODMR techniques, or alternatively by induced spin mixing and recording the extent of photoluminescence quenching. This method is favourable for a detonation nanodiamond sample containing multiple NVs because it avoids exact alignment of the NV axis to the field.

The current literature, as found through Thomas Reuters web of science and google scholar, indicates that the adhesion of nanodiamond to an optical fiber is a viable method for producing a probe magnetometer, with both high resolution and sensitivity possible.

3. OPTICAL SETUP

3.1 BENCH SETUP

The confocal-based setup used for experimentation is shown below:

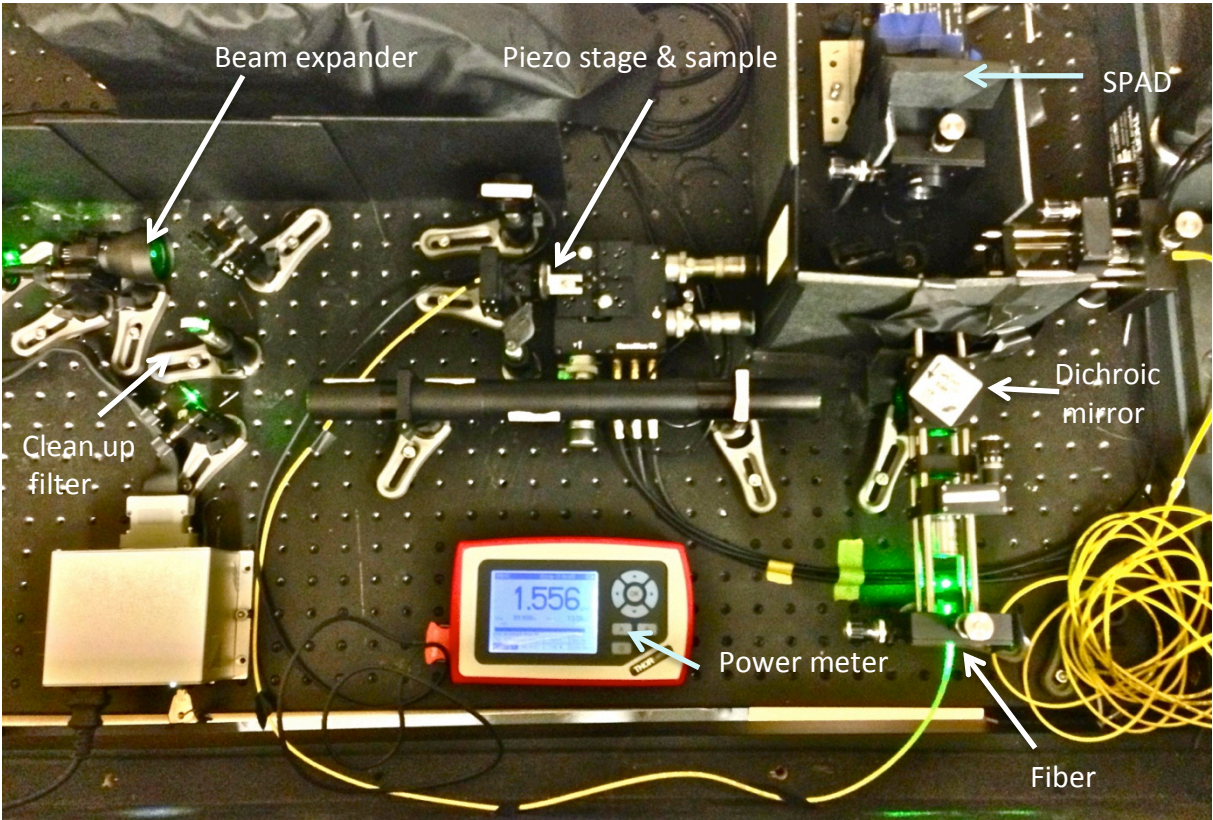
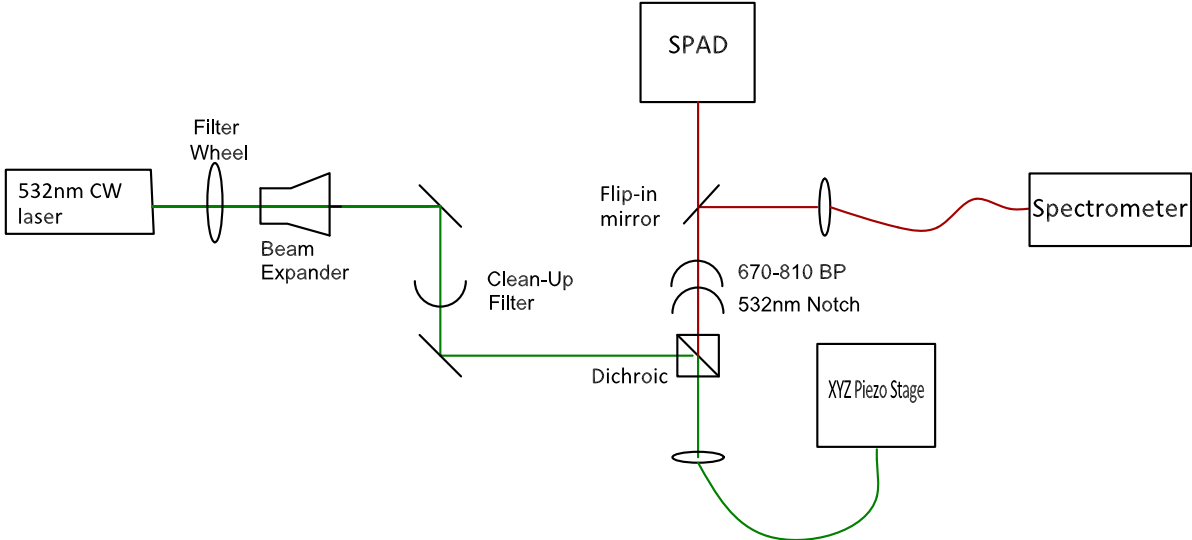


Figure3.1.1 Above drawing of setup and optical components and below an overhead image of the optical bench

An Oxiius 532nm continuous wave He-Ne laser diode (model 532L-200-COL-PP) was used to generate a circular Gaussian beam, with spot size taken at the beam waist $w_0 = \frac{1}{e^2} = 0.7\text{mm}$.⁶³ A Thorlabs variable filter wheel controlled laser power. A 5x beam expander after the filter wheel expands the beam to 3.5mm such that the objective lens was filled appropriately to minimise power losses. It also collimated the beam to ensure the light was neither diverging nor converging. A shear interferometer was used to assess qualitatively whether the beam was collimated. A collimated beam produces a fringe pattern that is parallel to the ruled reference line (figure 3.1.2).

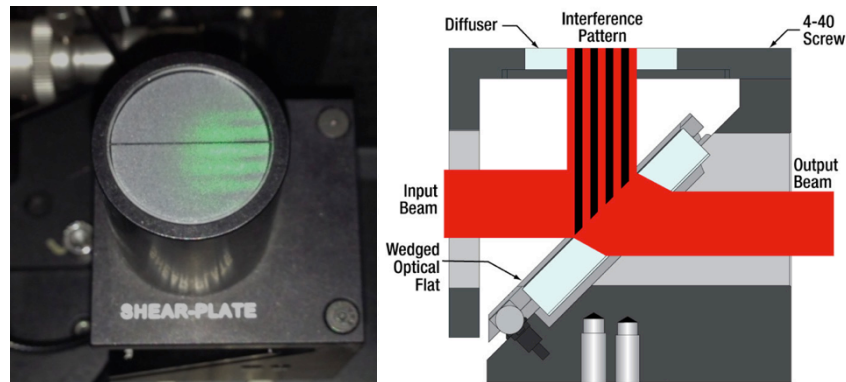


Figure 3.1.2. Left: parallel lines on the shear plate. Right: schematic of phase plate operation⁶⁵ 90% of the laser beam is transmitted, and 10% interferes with a wedged silica plate. Interference fringes are created by Fresnel reflections from the front and back surfaces of the optical flat.

A dichroic mirror reflects excitation light into an objective lens for coupling into a Thorlabs single mode optical fiber with mode field diameter (MFD) $\omega \approx 4\mu\text{m}$ at 532nm operation wavelength λ , and numerical aperture $\text{NA} = 0.1 - 0.14$. Efficient laser-to-fiber coupling requires optimal mode matching, which crucially depends upon the relative alignment of the fiber proximal end with respect to the laser. A 4x objective lens was selected for maximum coupling of laser light into the fiber. This was calculated using the following equation⁶⁴

$$f = \frac{\pi D \omega}{4\lambda}$$

whereby f is the lens focal length, $D = 3.5\text{mm}$ is the beam diameter incident on the lens, and ω the diffraction limited spot size, which for efficient coupling should match the MFD of the

fiber. Using $\lambda=532\text{nm}$, the theoretical optimum focal length for $4\mu\text{m}$ spot size should be 20.7mm . Below is a table of possible lenses and their working distances.

Olympus Achromat objective lens	Working Distance (mm)
X4	18.5
X10	10.6
X20	1.2

Table 3.1.1 Objective lens and their working distances

The optimum lens to focus the laser beam to a diffraction-limited spot is therefore x4. The x-y positioner-mounted fiber then transmitted the coupled light to excite the nanodiamond sample. The sample itself is mounted on a Thorlabs 3-axis flexure stage. Movement of the stage in all three axes allows for precise positioning of the fiber distal end with respect to the sample.

Photoluminescence light is then collected by the fiber, to be transmitted through the dichroic mirror to either the Excelitas free-space single photon avalanche detector (SPAD), or coupled into a fiber to the spectrometer. Before the SPAD is a 532nm Notch filter to remove any excess laser light which may be transmitted ($\sim 1\%$). An aspheric lens with $f=13\text{mm}$ before the SPAD focuses the beam without introducing spherical aberration.⁶⁵

Considerable effort was made to align the laser excitation arm and the fiber-to-SPAD collection arm to maximise photon count detection for a high sensitivity setup. Beam heights were dictated by the SPAD height, and propagation directions were orthogonal to maximise power throughput. The setup was regularly aligned to optimise light collection.

A data acquisition (DAQ) card converts the analogue waveform from the SPAD into an electrical signal. Labview software was used to record photon count rate. The falling edges of the digital signal from the DAQ card were recorded. A while loop enabled controlled repeat recordings to be made with a timer function to prevent unnecessary overloading of the desktop computer (figure 3.1.3). A waveform chart as seen in the front panel in figure 3.1.4 creates a visual of the photon counts recorded.

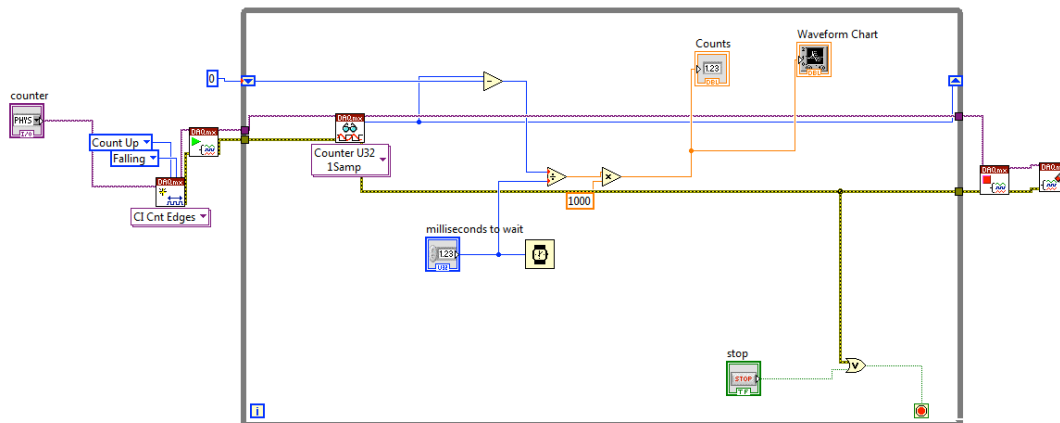


Figure 3.1.3 Print screen of the Labview block diagram, where the script is written.



Figure 3.1.4 Print screen of the SPAD counter front panel in Labview. This is the user interface, with a waveform chart to display photon count rate

3.2 SPECTROSCOPY

Spectroscopic analysis was carried out to study the fiber background signal and to confirm the sample studied and then adhered to the fiber to be NV containing nanodiamond. Figure 3.2.1 shows how the spectrometer works. Light enters the spectrometer through a variable slit. A large slit width $\sim 3\text{mm}$ and imaging mode is used for alignment of the beam with respect to the spectrometer.

Light enters the spectrometer and is collimated by a mirror. To take a spectrum, the entrance slit is narrowed to the spot size of the light for spatial confinement. A metallized grating, designed to maximise the first order diffraction beam to typically 80% efficiency, is

used to reflect and separate the light into its constituent wavelengths. A mirror then focuses the light onto a CCD.

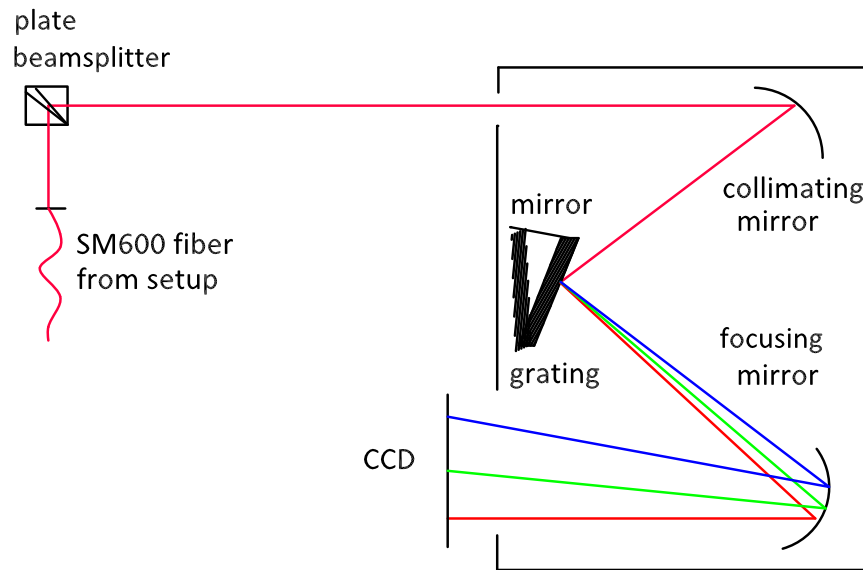


Figure 3.2.1 Drawing of the spectrometer. The mirror, 1200lines/mm and 300 lines/mm may be selected by rotation.

A grating with either 300 lines/mm or 1200 lines/mm may be selected. 300 linesmm⁻¹ allows for a wider range of wavelengths to be recorded per scan (150nm range), as limited by the size of the CCD. Should 1200 lines/mm be used, a higher spectral resolution is attained, but only wavelengths in a 40nm range may be recorded. For the purpose of my experiments I used 300 lines/mm and a ‘step-and-glue’ mechanism on the spectrometer, which moved the grating manually to obtain wavelengths between 500nm and 900nm. Occasionally this mechanism gave unexpected shifts in data, so had to be used with caution. However it gave an appropriate spectral overview of the light collected and produced by the fiber. Different forms of background noise and the means of improving signal-to-noise ratio are recorded in table 3.2.1.

Type of Noise	Source of Noise	Mitigation
Thermal	From Si in CCD	CCD cooled to at least -40 degrees Celsius
Electronic Read-out	Shot noise ~90 counts independent of experiment time	Integrate spectra over longer time period, 30s minimum
Spectral background	Room light	Spectra taken with room light switched off

Table 3.2.1 Types of spectral noise, their source and techniques to improve signal-to-noise

3.3 FIBER CHARACTERISATION

Prior to photoluminescence study, a spectrum was taken of the bare fiber for comparison (figure 3.3.1). A small percentage of 532nm laser light is transmitted through the dichroic mirror and notch filter. In addition numerous peaks are detected ranging from 537nm to 586nm, similar to those seen in figure 2.5.3 [Schoeder *et al.*]⁵¹ These are due to Raman scattering in the fiber. Raman scattering is the scattering of laser light to longer wavelengths in the silica core and cladding.^{66,67} These peaks are removed by positioning a 670-810nm-band pass filter before the SPAD and spectrometer. Additional unexpected peaks were initially detected in recorded spectra, but were removed by methanol sonication of the fiber tip, and therefore were attributed to dirt and contaminants. As a result, each fiber was cleaned prior to use in the setup.

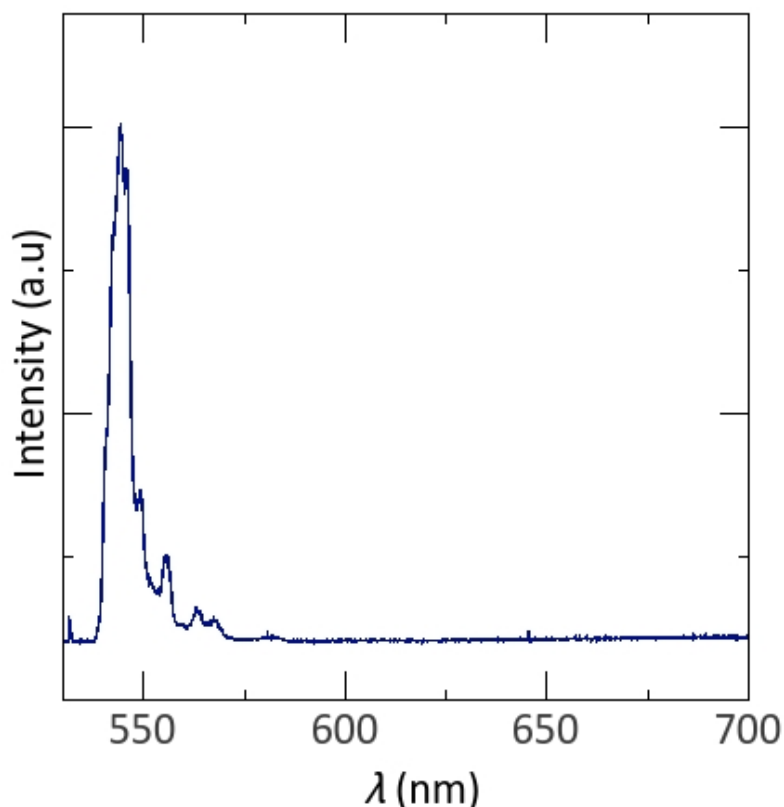


Figure 3.3.1 Background bare fiber signal with peaks from the laser and Raman scattering

In spite of spectral filtering of Raman scattered laser light, an exceptionally high signal of several million counts was detected by the SPAD. This increased linearly with laser power (see figure 3.3.2).

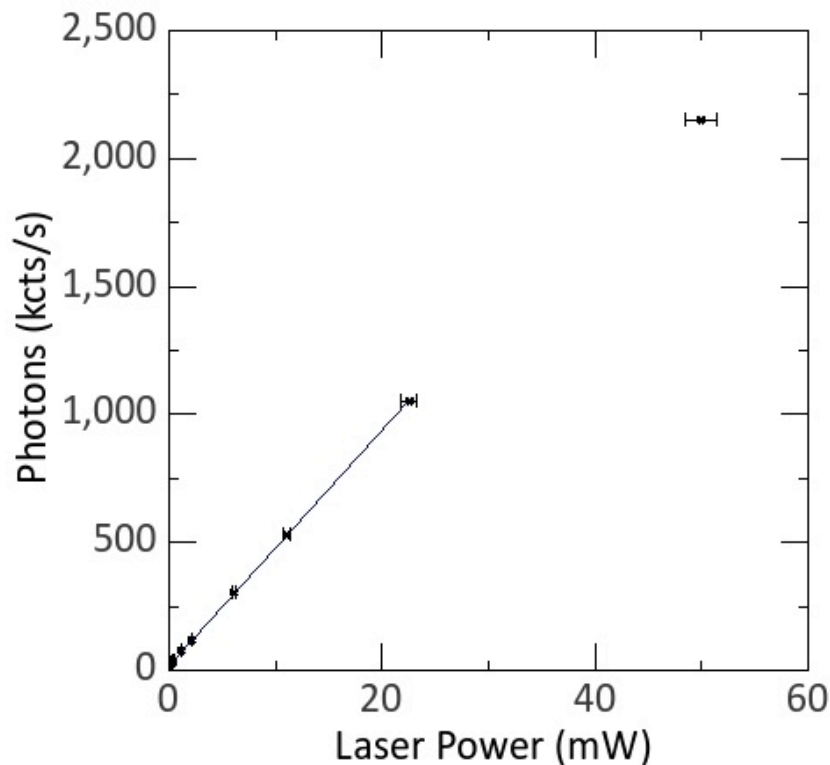


Figure 3.3.2 Comparison of laser power against photon kcts/s. At high powers, the signal falls over time, implying a photobleaching effect. Laser power uncertainty $\pm 3\%$

A neutral density filter was placed before the SPAD to prevent it from being overloaded (when counts exceed 1×10^7 for an extended time period). Quantitative spectral comparison could not be made due to transmission losses to the spectrometer: when coupling the light into the spectrometer-fiber and at the plate beamsplitter, which reflects 70% of the light incident and has a back wedge at a 0.5° angle to eliminate internal fringes: reflected light diverges slightly. The CCD is also less sensitive than the free-space SPAD. By using a fiber-coupled SPAD, counts reaching the spectrometer were maximised and a spectrum taken at high laser power suggests that the high SPAD count rate is due to autofluorescence originating from impurities within the fiber itself as mentioned by Schoeder *et al.* and Rabeau *et al.*^{6,51}

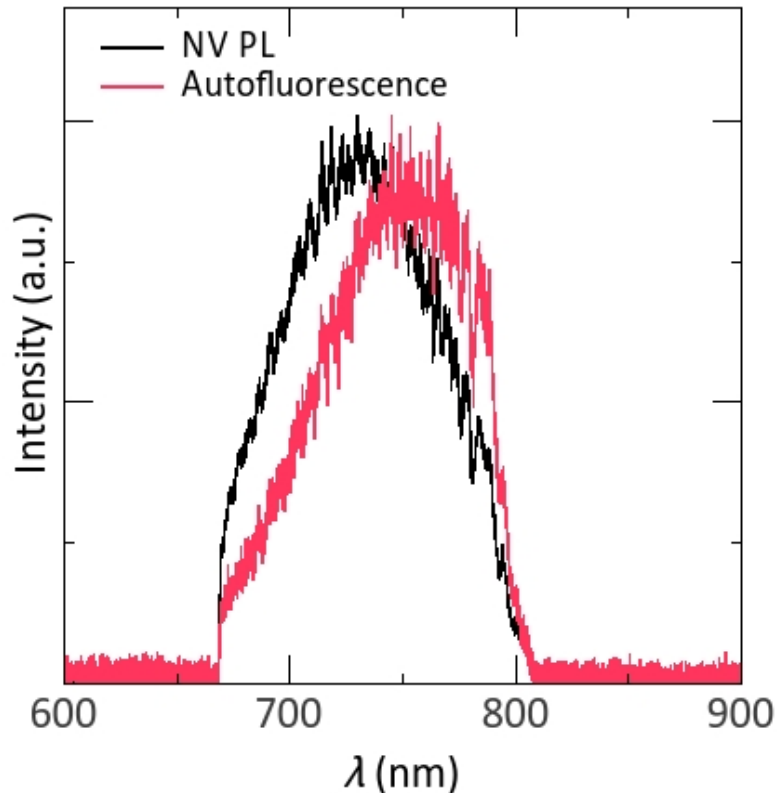


Figure 3.3.3 Spectral comparison of fiber autofluorescence and NV PL. The data sets were independently normalised to demonstrate the significant spectral overlap

Unfortunately autofluorescence may not be removed by spectral filtering because it is in the same wavelength range as NV photoluminescence (see fig 3.3.3). Other fibers with different operation wavelengths and a graded index multimode fiber were tested, all with a background signal of similar magnitude.

3.4 ALTERNATIVE FIBERS

A single mode fiber is preferable for illumination delivery, for high-resolution imaging and a small diffraction limited spot size to detect and precisely locate an individual nanodiamond. It also acts as a pinhole detector, rejecting any out-of-plane photoluminescence emission⁶⁸. However, to compare autofluorescence intensity, a connectorised graded index multimode fiber with core diameter 62.5 μm was tested. The fiber distal end was inserted into a photodiode, which converted incident photons into a current recorded on a Keithley source meter with precision $\pm 0.012\%$.⁶⁹ The proportion of laser light exiting the fiber corresponds to the coupling efficiency of the 130 μW laser light entering the fiber. By making small adjustments to the fiber position using the x-y mount, coupling is altered. Photon counts

produced from the fiber are compared to the coupling efficiency, to determine the origin of the autofluorescence and whether it may be minimised.

Poor coupling into the fiber core results in photon counts exceeding 2×10^7 due to reflection of laser light at the fiber surface and mount. As the coupling improves and laser light hits the fiber cladding, photon count falls as light is transmitted. As more light is coupled effectively into the fiber core, autofluorescence increases the detected photon count. As a larger fraction of laser light is coupled into the fiber and is transmitted to the photodiode photon count decreases once more.

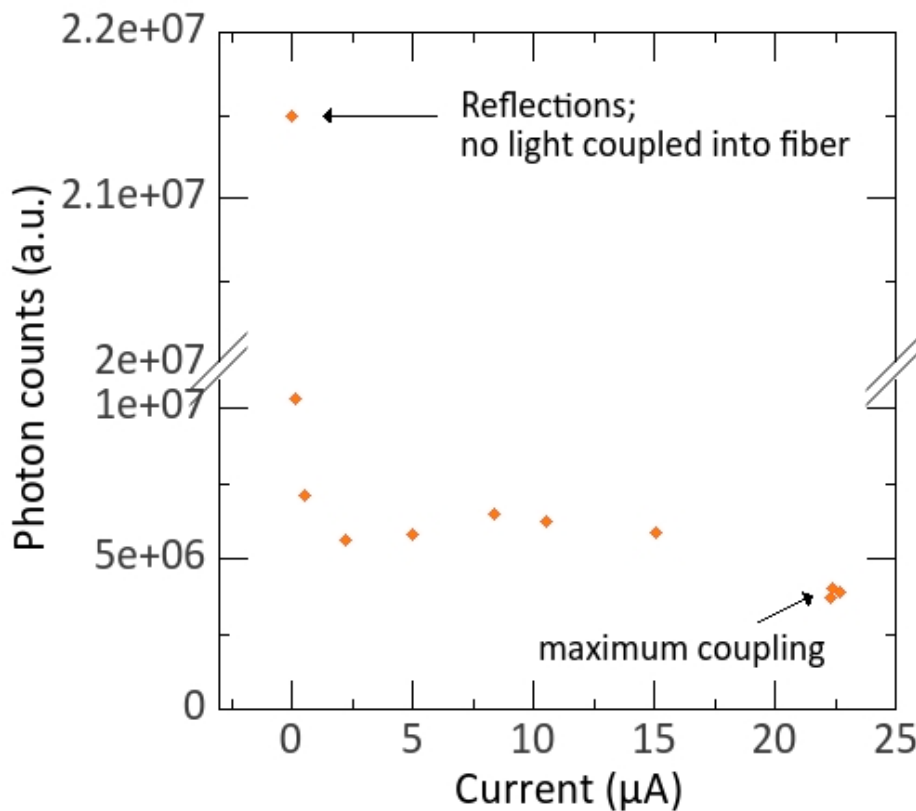


Figure 3.4.1 SPAD photon counts/s against photodiode current corresponding to laser light transmitted by the fiber

The same trend is seen in the SM600 fiber (figure 3.4.2). In contrast, the SM8005 fiber shows no decrease in photon counts once maximum coupling has been achieved. This may be explained by the cut off wavelength of the fiber. The single mode cut off for the SM8005 fiber is ~ 750 nm and therefore the guided mode is not achieved with 532nm laser light. Hence a lower fraction of power propagates through the core and photon counts are seen only to increase with power transmission.

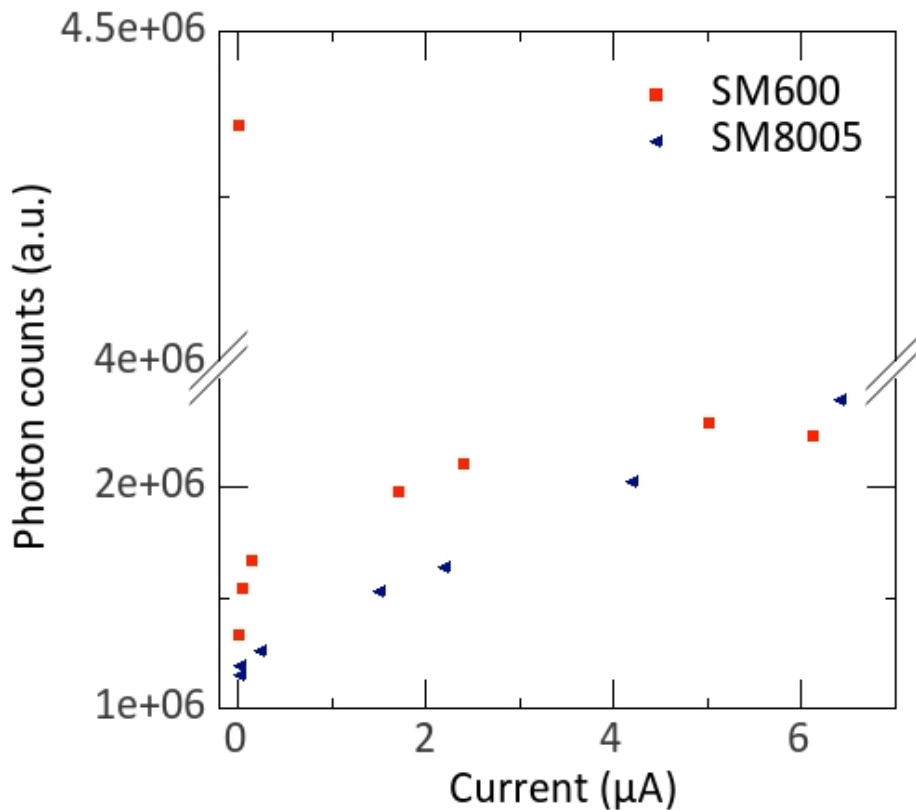


Figure 3.4.2 Graph of Keithley current reading produced by the photodiode at the end of fibers SM600 and SM8005, and corresponding SPAD photon count rate

Standard single mode fibers used are Ge-doped cores with silica cladding. The dopants in the core may be the cause of high background fluorescence.⁷⁰ Roland Albrecht's thesis reported lower autofluorescence intensity in a pure silica core fiber compared to that of a doped core⁷¹. A thorlabs SM630HP fiber with pure silica core was tested and count rate compared to SM600, both with 20% laser light coupling and 0.8m length (figure 3.4.5). Although the photon count rate is lower at a given laser power, SM630HP still generates high autofluorescence. A possible explanation could be the silica itself generates a signal of its own, with additional dopants in the core of standard fibers contributing to autofluorescence further. Fujii *et al.* report similar findings and avoid silica fibers by using photonic crystal fiber (PCF).⁷² Should the autofluorescence noise overpower the photoluminescence signal, using a PCF may be necessary. This approach would be more costly and may introduce complexities in nanodiamond adhesion method due to the air holes present in PCFs.⁷²

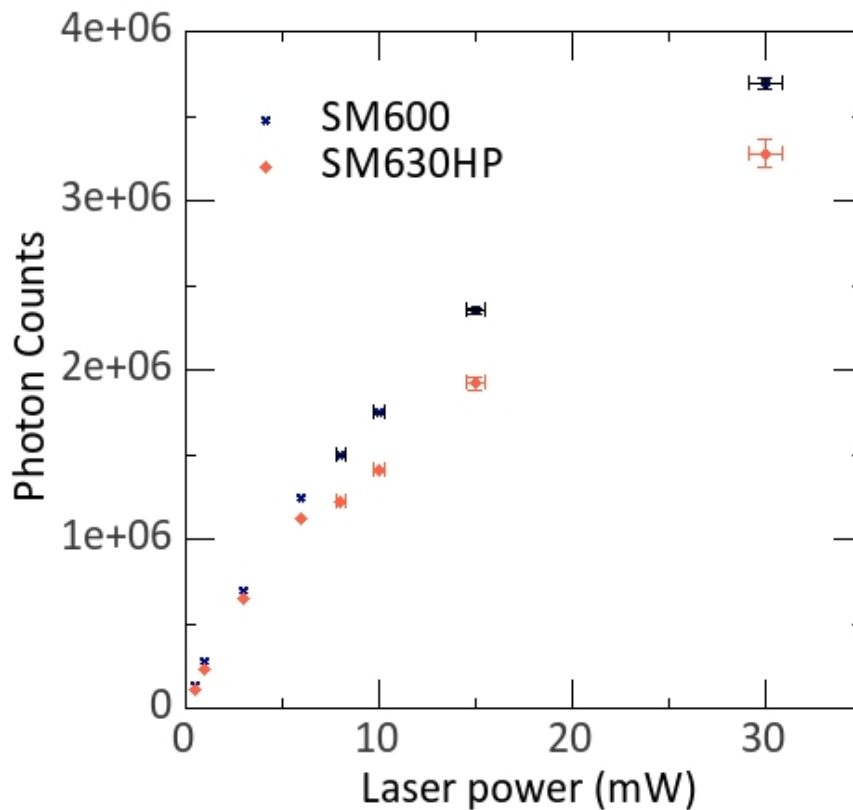


Figure 3.4.5 Comparison of Ge-doped core SM600 and high purity silica core SM630HP fiber photon counts with varying laser power. Data was collected over 50s, with error in photon counts found by standard deviation of data

3.5 POLARISATION EFFECTS

In addition to high autofluorescence, large photon count fluctuations were noted. The 532nm notch and 670-810nm bandpass filters were temporarily removed from the setup and a neutral density filter placed before the SPAD. At laser power 1.035mW and 140 μ W fiber transmission (coupling 13.5%), the average photon counts detected per second taken over a time period of 55s was 31,152. However there was a standard deviation of ± 1325 counts or $\pm 4.253\%$ of the signal. This deviation is much higher than the stability of the laser as calibrated prior to my arrival in the group by Alex Powell. The laser power deviates from its true value by only $\pm 1\%$ when taken over 2 minutes (see Appendix D).

This photon count oscillation is dependent on thermal vibrations experienced along the fiber length. By agitating the fiber, the regularity of the oscillation is eradicated (figure 3.5.1).

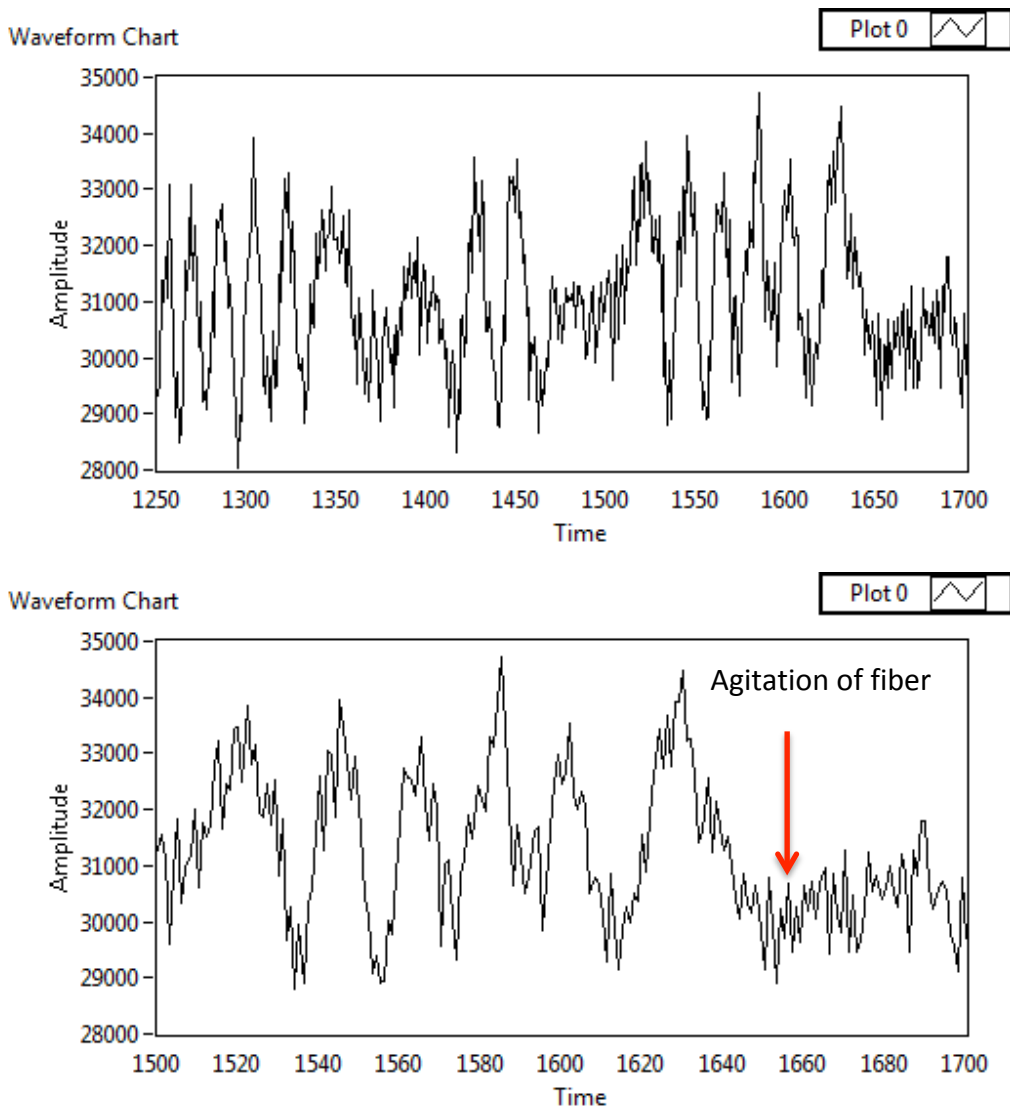


Figure 3.5.1 Waveform graphs of SPAD photon counts/100ms. Above is the measured fluctuation over 55s, and below demonstrates the effect of fiber agitation

The polarisation sensitivity of the dichroic mirror is the suspected cause of this oscillation⁷³. A change in polarisation is caused by irregularities in fiber geometry and change in refractive index. As coherent laser light travels along the optical fiber, birefringence in the optical cladding and impurities in the core cause a change in the light's polarisation state. The light passes through the dichroic with a time dependence depending on its polarisation state⁷³. Fortunately the photoluminescence signal is not seen to fluctuate as drastically: the broad range of emission frequencies makes it highly incoherent hence such strong polarisation effects are not detected. Oscillations were stabilised by temporary adhesion of the fiber to the optical bench to minimise effects of motion and bend losses. A temporary cover placed over the setup minimised changes in environment experienced by the fiber.

4. PHOTOLUMINESCENCE IMAGING OF NANODIAMOND

4.1 SCANNED IMAGING

The software programming for photoluminescence imaging using the thorlabs 3-axis piezo stage, detailed in Appendix B, was written with thanks to Matthew Wincott. Once the Labview program had been written, the setup was calibrated using a Ronchi grating. Figure 4.1.1a is an optical image of the grating. $5\mu\text{m}$ wide lines with $10\mu\text{m}$ spacing are apparent.

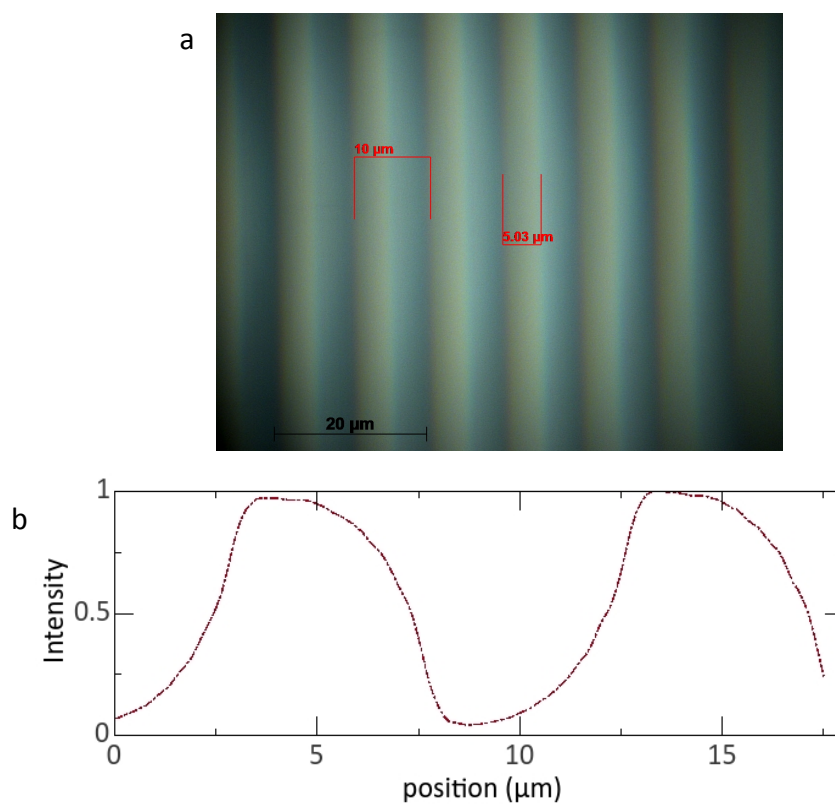


Figure 4.1.1a) Optical image of the Ronchi grating. Lines are $5\mu\text{m}$ apart with a $10\mu\text{m}$ spacing b) depending on image resolution and the microscope lamp brightness, the line profile across the grating is smooth. A binary image gives a box-like profile.

Whilst the lines in the grating are not fluorescent, they reflect excitation light that is collected back into the fiber. Silica between the lines transmits the incident laser light; the regions of lower intensity in figure 4.1.2b. The grating's 100 lines/mm corresponds to 2 lines in a $20\times 20\mu\text{m}$ image (figure 4.1.2a). Irregularities in the Ronchi lines are due to polarisation effects in the fiber (see section 3.6). A box profile was taken, averaging grey scale values over 40 line profiles to minimise noise effects in the data. The profile corresponds to that of

the optical image in 4.1.1b, but with smoother peak intensities due to the collection of light by the fiber (see section 4.4). Note that in both the optical image profile and the fiber scanned image profile, there is a gradual intensity change as each line is approached from left to right. This is likely to be due to the fabrication process of the Ronchi grating.

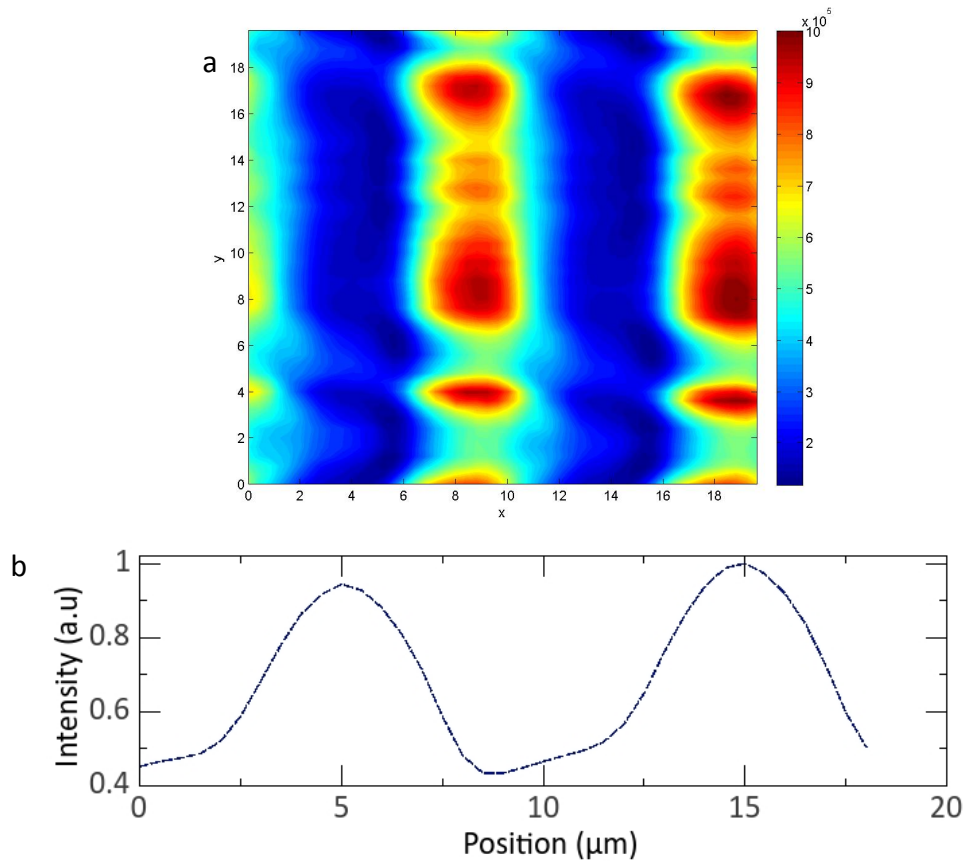


Figure 4.1.2 a) 20x20 μ m scanned image of a 100 lines/mm Ronchi grating b) box profile of image, demonstrating 10 μ m separation

Success of imaging a grating confirmed that photons collected at the fiber distal end could be sensed and recorded, sensitive at the micrometer scale. This was confirmation that the optical setup was well aligned for PL imaging.

4.2 IMAGING PHOTOLUMINESCENCE

Due to fiber autofluorescence, photon count fluctuations and fiber-to-substrate proximity uncertainty, a very bright emitter was required to determine the potential of fiber fluorescence collection. Quantum dots emit brightly and are used as chemical and temperature sensors.⁷⁵ Using cadmium selenide drop cast on a silicate substrate, provided thanks to Laiyi Weng, PL was detected from >mm fiber-distance. No distinct PL images could be taken because of the dense particle packing in the thin film. A spectrum was taken to confirm the light intensity increase to be from CdSe photoluminescence.^{74,75} The collection of CdSe PL indicated the potential of the fiber to transmit both excitation and photoluminescence light simultaneously.

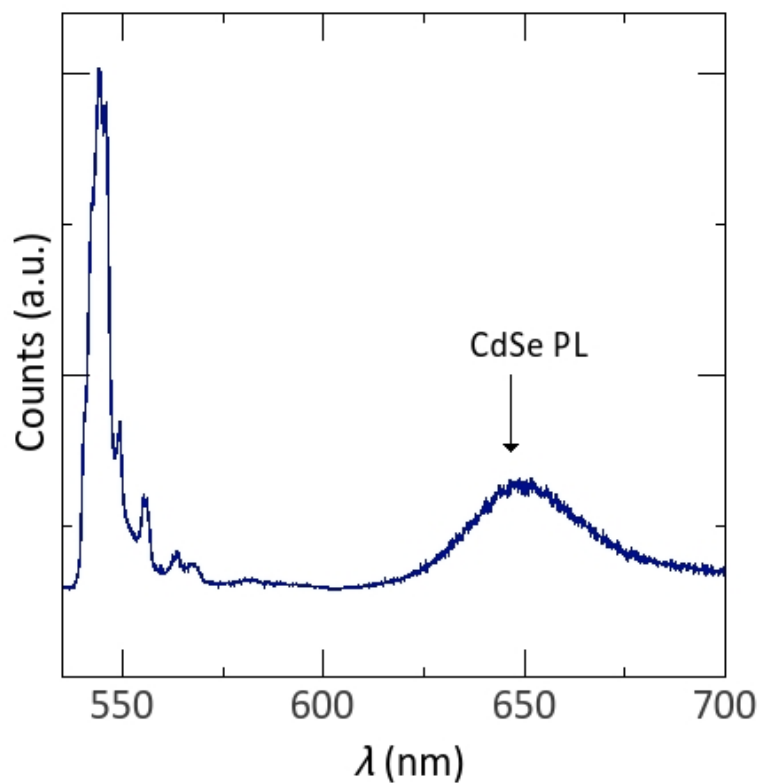


Figure 4.2.1 Spectrum of CdSe PL over 20s, with no 670-810 band pass filter in place. Due to the high PL intensity and Raman signal, a neutral density filter was placed before the spectrometer and laser power of 0.17mW used. The fiber-probe coupling was ~30%

4.3 VARYING NANODIAMOND CONCENTRATION

Following the success of fiber PL collection, 2-3 drops of commercial detonation nanodiamond solution was cast on a silica coverslip and left to dry in atmosphere. The nanodiamonds are dispersed in water with 1mgml^{-1} . They are on average 200nm in size, and contain a high density of fluorescent NVs. This increased their ease of detection. Prior to application the sample was sonicated for a minimum of 5 minutes to disaggregate the particles.⁷⁶ Due to the high density of nanodiamonds in the sample provided, further dilution in methanol was necessary to isolate individual particles on the coverslip.

The degree of disaggregation with varying dilution is seen in figures 4.3.1 a-f overleaf with results concluded in the table below.

Sample	Distinguishable features in 20x20 μm scan
CdSe quantum dots	None – spatial variation
Concentration ND solution	Spatial variation, agglomerated regions
1:2 ND in methanol	~6 agglomerates per scan, occasional individual particle
1:5 ND in methanol	Individual nanodiamonds, often agglomerated in pairs
1:10 ND in methanol	Time consuming and difficulty detecting nanodiamonds by change in photon count signal
1:5 ND spin coated 3500RPM for 180s	Individual nanodiamonds detected and well dispersed across substrate

Table 4.3.1. compares different sample concentrations and preparation methods to nanodiamond dispersion on a coverslip

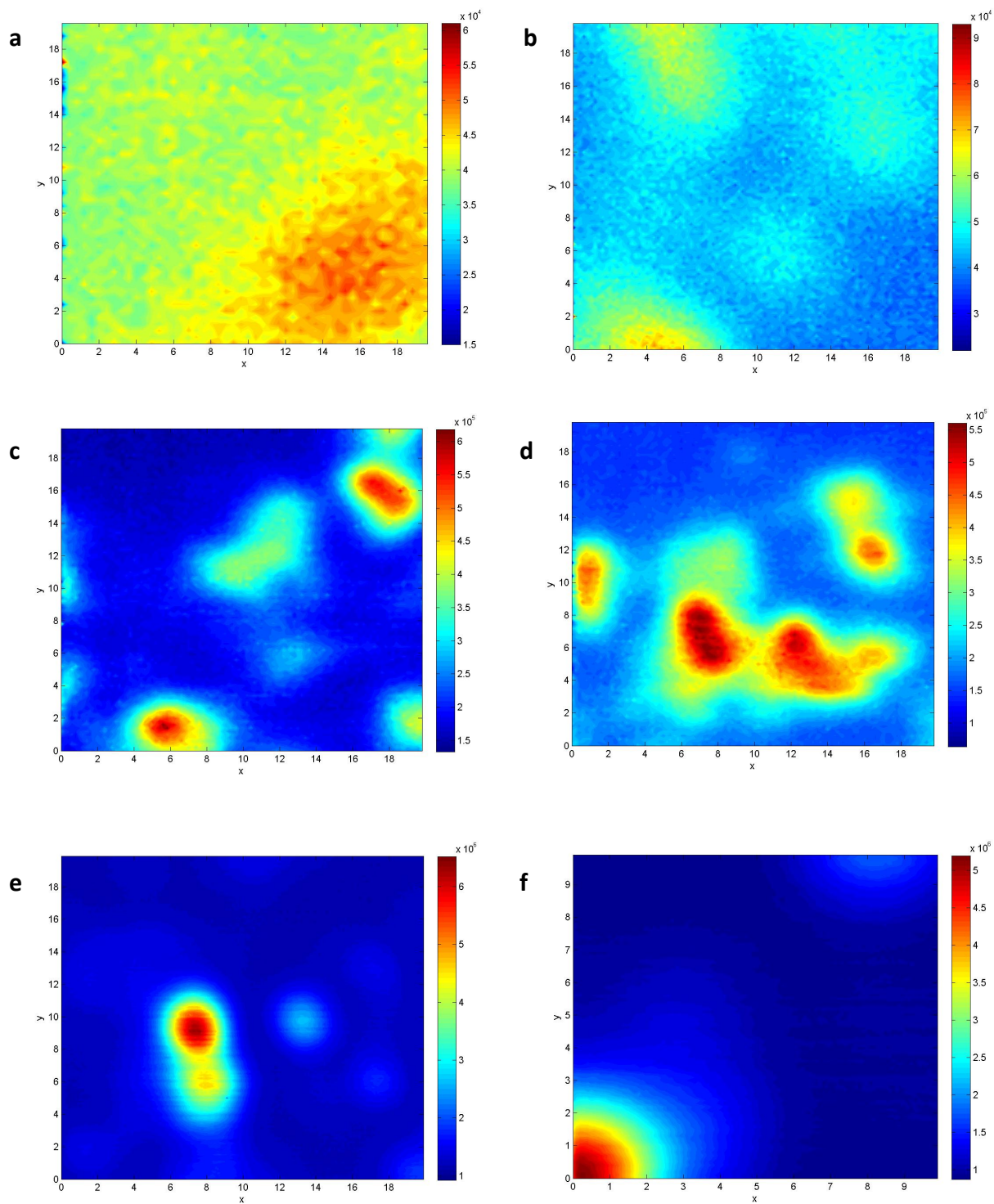


Figure 4.3.1 (a) concentrated solution 1mgml^{-1} with spatial variation. When the fiber proximity is increased by $100\mu\text{m}$ (b) more distinct ND agglomerates are detected. (c) and (d) show PL images of the ND sample diluted 1:2 in methanol, with heavy particle agglomeration. (e) 1:5 dilution shows less agglomeration, but the particles are not well dispersed. (f) fiber positioned above a nanodiamond in 1:5 dilution, spin coated. Pixel size is 200nm^2 and 30ms step integration time

4.4 STUDYING AN INDIVIDUAL NANODIAMOND

To improve particle dispersion, 1:5 nanodiamond solution was spin coated at 3500RPM for 180s. This allowed for the PL collection from an individual nanodiamond in a single 20x20 μm scan (see figure 4.4.1). FWHMs were calculated, which correspond to a beam waist (half width at $1/e^2$) $w_0 \approx 4.15 \mu\text{m}$ at 532nm. This is as one would predict, matching the mode field diameter of the fiber used quoted as 4.3 μm at 633 nm and 4.6 μm at 680 nm.⁶⁵

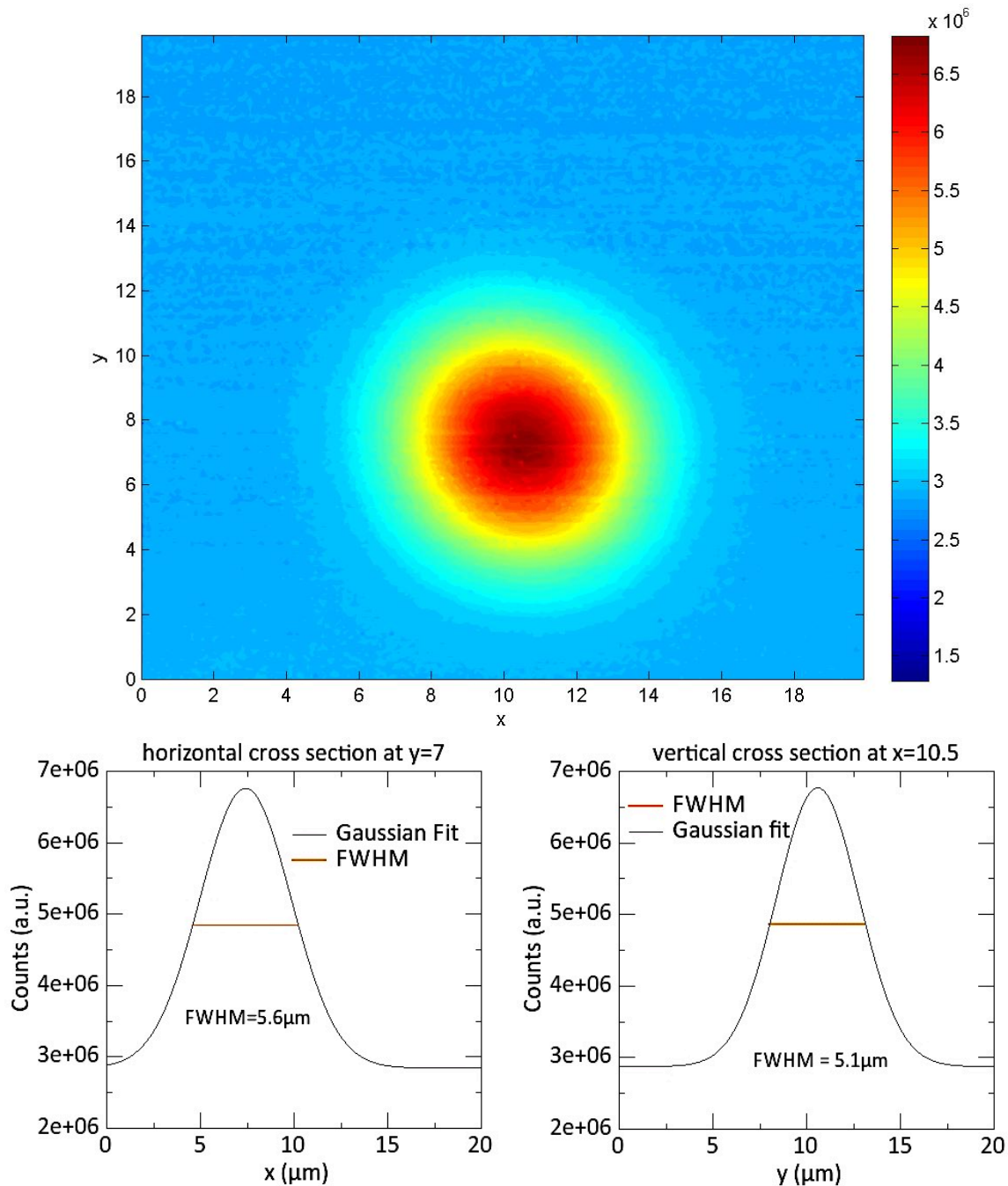


Figure 4.4.1 20x20 μm PL image of a single nanodiamond taken with 100nm² pixel size, and FWHM data used to calculate fiber core diameter

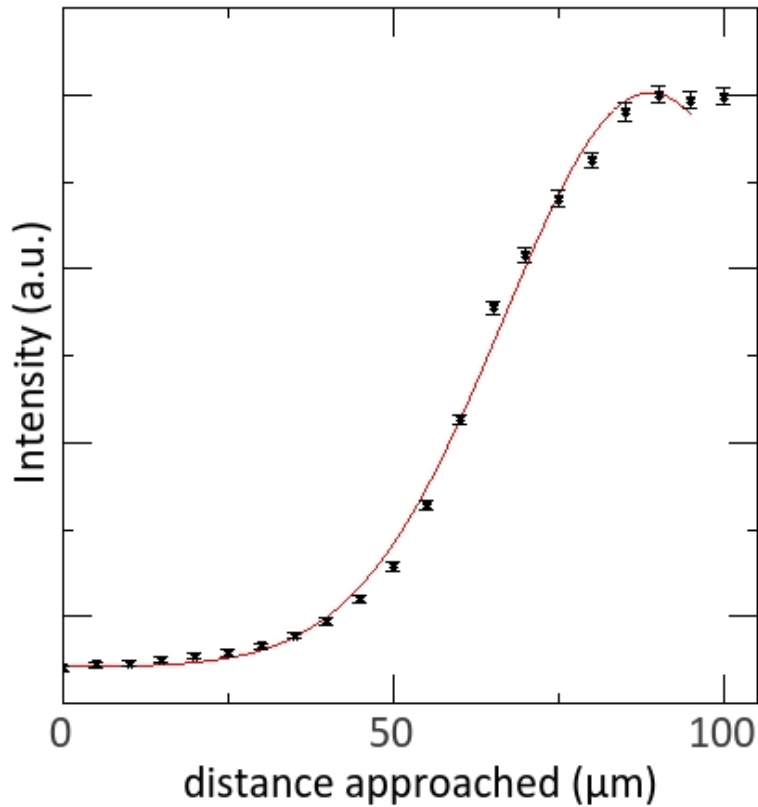


Figure 4.4.2 Variation in photoluminescence intensity with fiber proximity

Because the nanodiamond is multi-faceted, emitted light radiates at all angles, so photoluminescence collection increases as fiber-sample separation decreases (above). Counts plateau as radial photon emission fills the fiber core. With nanodiamond size \ll fiber core diameter, it may be regarded as a point light source. By measuring the change in photoluminescence with respect to fiber proximity, the experimental value of focal length is found at the distance at which the detected fluorescence falls to one half of its maximum: the axial resolution of the fiber.

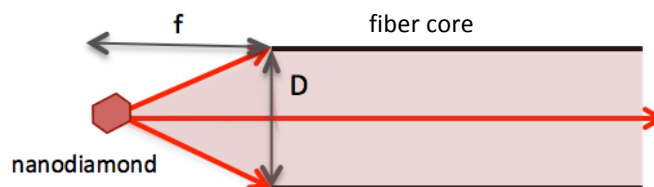


Figure 4.4.3 displaying the collection of light by the optical fiber. f is the focal length which is confirmed to be $40\mu\text{m}$ and D the fiber core diameter

From the numerical aperture $NA=0.1$ and core diameter of the fiber tip, one may calculate the focal length of the fiber:⁷⁷

$$f = \frac{nD}{2NA}$$

the aperture, or in this case the fiber core diameter, $D=8.3 \mu\text{m}$, the refractive index in air $n=1$, and therefore the calculated focal length is $42 \mu\text{m}$. From the figure 4.4.2, the axial resolution is $40 \mu\text{m}$, which is in concordance with the focal length calculated.⁷⁸

As confirmation the source of photoluminescence originated from NV centres in an individual nanodiamond particle, spectrum of the fiber both directly 'on' and 'off' the nanodiamond were taken (figure 4.4.4). In regions where the fiber is 'off', no PL signal is detected and only photon counts from fiber and coverslip autofluorescence are detected. 'On' position demonstrates a PL signal typical of NV colour centres, as seen in the literature.

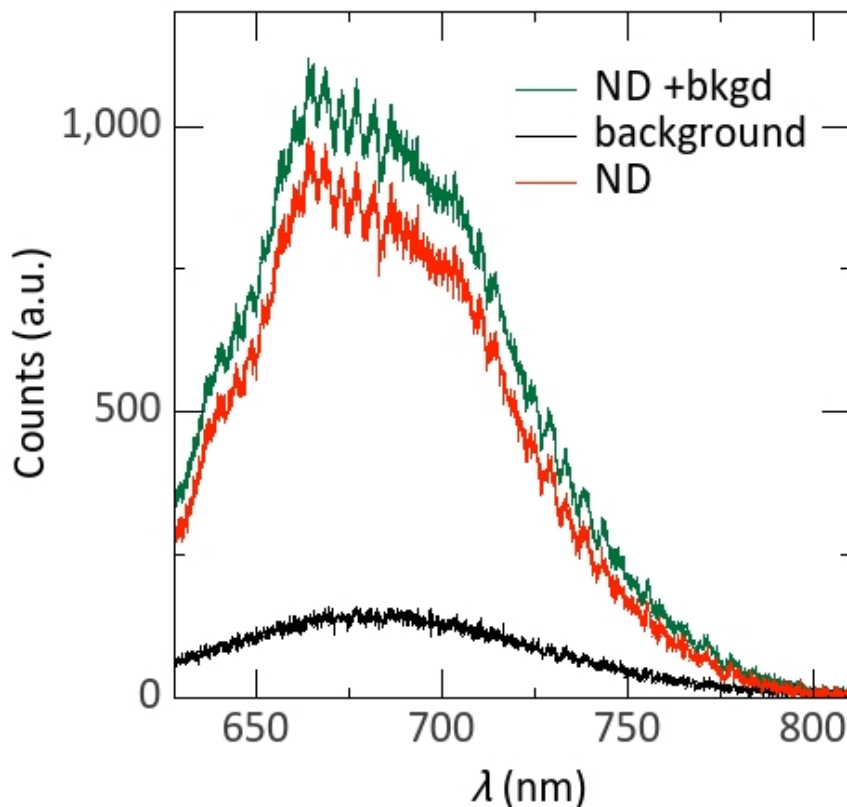


Figure 4.4.4 Shows spectra taken 'on' and 'off' the individual nanodiamond seen in the previous image. A slight peak is seen at 637nm for the ZPL, and a broad PL characteristic of NV

5. THE MAKING OF A PROBE MAGNETOMETER

5.1 FIBER CLEAVING

A silica based core and cladding with a protective buffer layer, acrylate coating and connectorised ends constitute the purchased SM600 fiber. A 2.5mm diameter ceramic ferrule surrounds the accurately positioned fiber core for protection. It is imperative that the fiber axis is 90° to the substrate to ensure optimal coupling⁷⁹. Although the ferrule is flat, it is difficult to approach normal to the substrate. Often the fiber ferrule would become contaminated or scratched, as in figure 5.3.1a. To obtain as uncontaminated a distal end as possible and for ease of approach to the nanodiamond, the fiber was cleaved. The connector end was removed with acetone (figure 5.1.1b). A mechanical stripper then removed the buffer coating, revealing the core and cladding of the fiber (figures 5.1.2b & 5.1.3b). A diamond scribe was used to scratch a cleavage point, and the fiber was subsequently pulled away. Should the end be poorly cleaved, light collection and emission is inefficient from the fiber (fig. 5.1.3c).

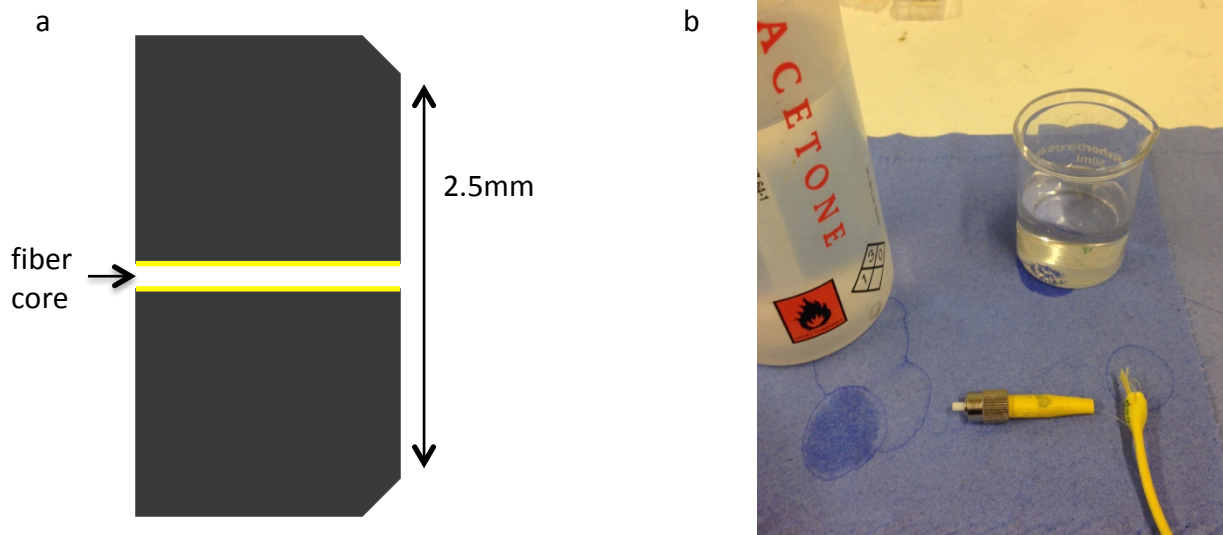


Figure 5.1.1 a) schematic of the ferrule connector and b) its removal

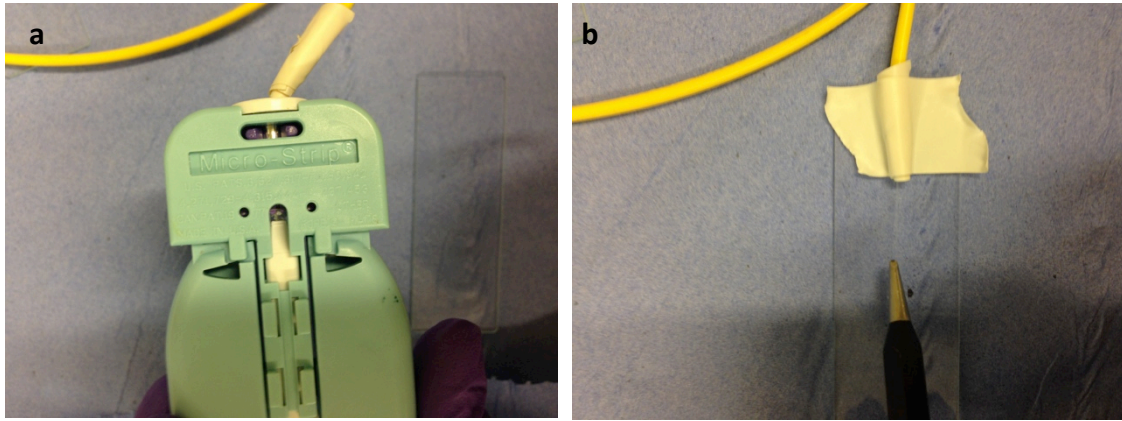


Figure 5.1.2 a) stripping the buffer layer and b) using the diamond scribe

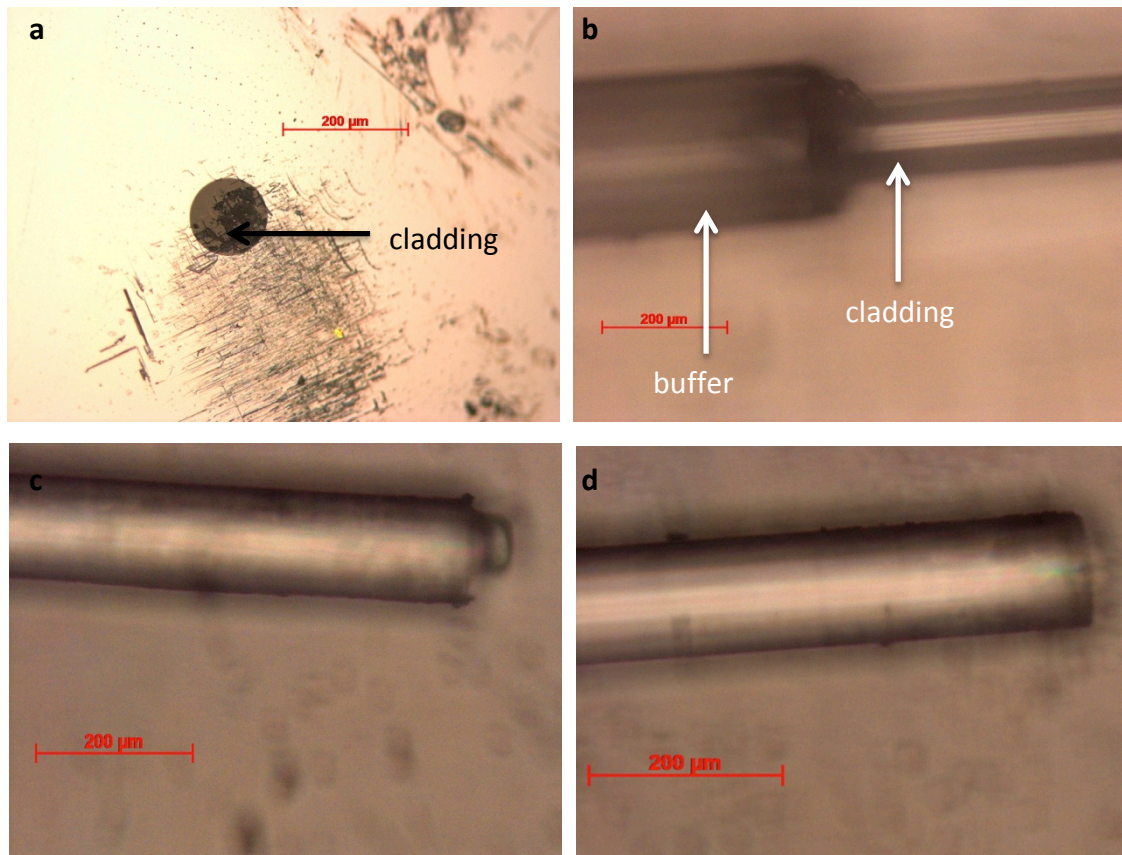


Figure 5.1.3 Optical images of the fiber a) shows the ferrule end with scratches over the fiber cladding. The fiber core is no longer visible due to displacement within the ferrule upon impact b) Stripping of the fiber down to just cladding (125 μ m) and core. c) shows a poor and d) good fiber cleave

Following fiber cleaving, the nanodiamond had to be adhered to the fiber tip.

5.2 UV CURING ADHESIVE

Different approaches were taken to adhere the nanodiamond to the fiber. It was desirable to have the nanodiamond accurately positioned on the fiber core, so a pick-and-place method was adopted. Norland optical adhesive was selected for its transparency at operation wavelength and ease of curing using UV light⁸⁰. Once the nanodiamond had been located and the adhesive applied, no movement in x-y could be made, or the adhesive would smear and the fiber no longer be perpendicular to the substrate (see figure 5.2.2a).

The adhesive is optimum for bonding glass to glass, and bonds poorly to polymer. Hence an experiment was designed with the nanodiamond coated on a thin polymer layer (figure 5.2.1).

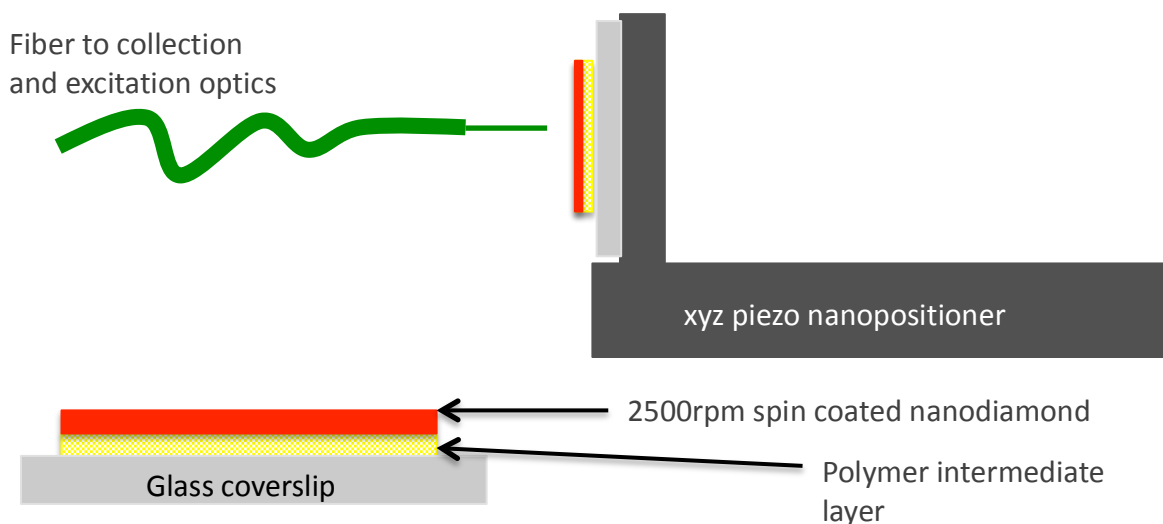


Figure 5.2.1 Schematic of the fiber-stage configuration, and the sample preparation method adopted

Initially a Perspex substrate was used, however this generated a large level of autofluorescence and substrate curvature caused fringes on images taken (fig 5.2.2b).

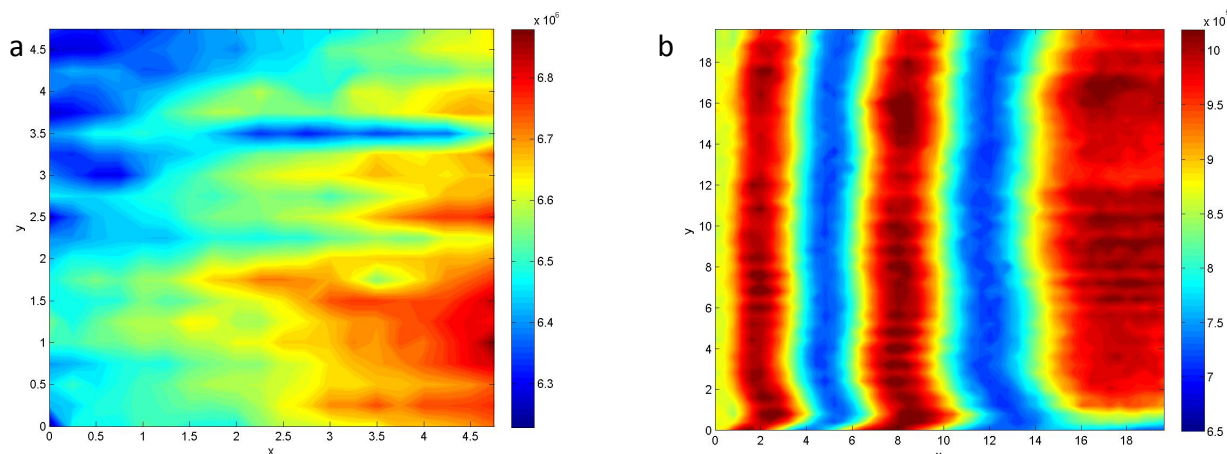


Figure 5.2.2 a) A scanned image of the ‘smearing’ effect of UV adhesive on the nanodiamond PL collected by the fiber b) scanned image of autofluorescence variations due to curvature of the Perspex substrate

Other polymers such as mylin were considered, but again, handling difficulties were encountered when trying to obtain a level surface. Polymethylmethacrylate (PMMA) has very low autofluorescence.^{81,82} A 75mgml⁻¹ solution of PMMA in toluene, provided by Dr David Coles, was initially tested by spin coating a thin layer (~300nm) onto a coverslip followed by a layer of spin coated nanodiamond. The nanodiamond could then be detected and UV adhesive applied directly to the nanodiamond, PMMA and coverslip. The coverslip was then removed from the mounted stage along with the fiber using a scalpel. The fiber and coverslip were separated, but with some difficulties experienced with fracture of both components. The thick layer of adhesive necessary in this method created somewhat of a bulky end to the fiber (see figure 5.2.3). This caused frequent fiber fracture.

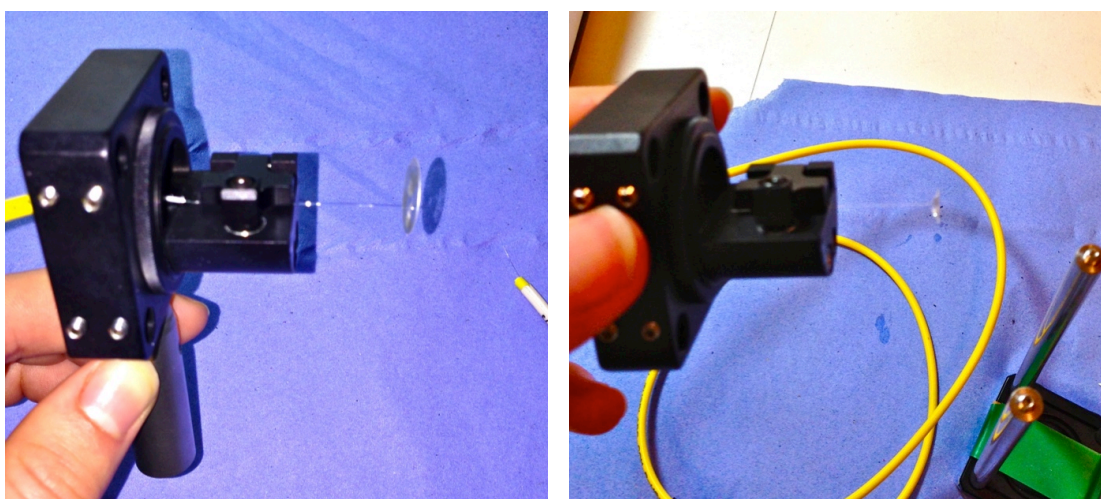


Figure 5.2.3 Images of the adhesive-to-coverslip application method. Left is fiber and coverslip removed from the stage mount, and right the fiber with excess adhesive post-curing

To obtain a more robust tip, the PMMA was solvent cast, such that it was several microns thick. Upon toluene evaporation, slight shrinkage curls the film up at the edges⁸³. This is advantageous for the removal of the polymer from the coverslip with the nanodiamond and fiber still attached. Excess polymer may then be dissolved using methanol (fig 5.2.4).

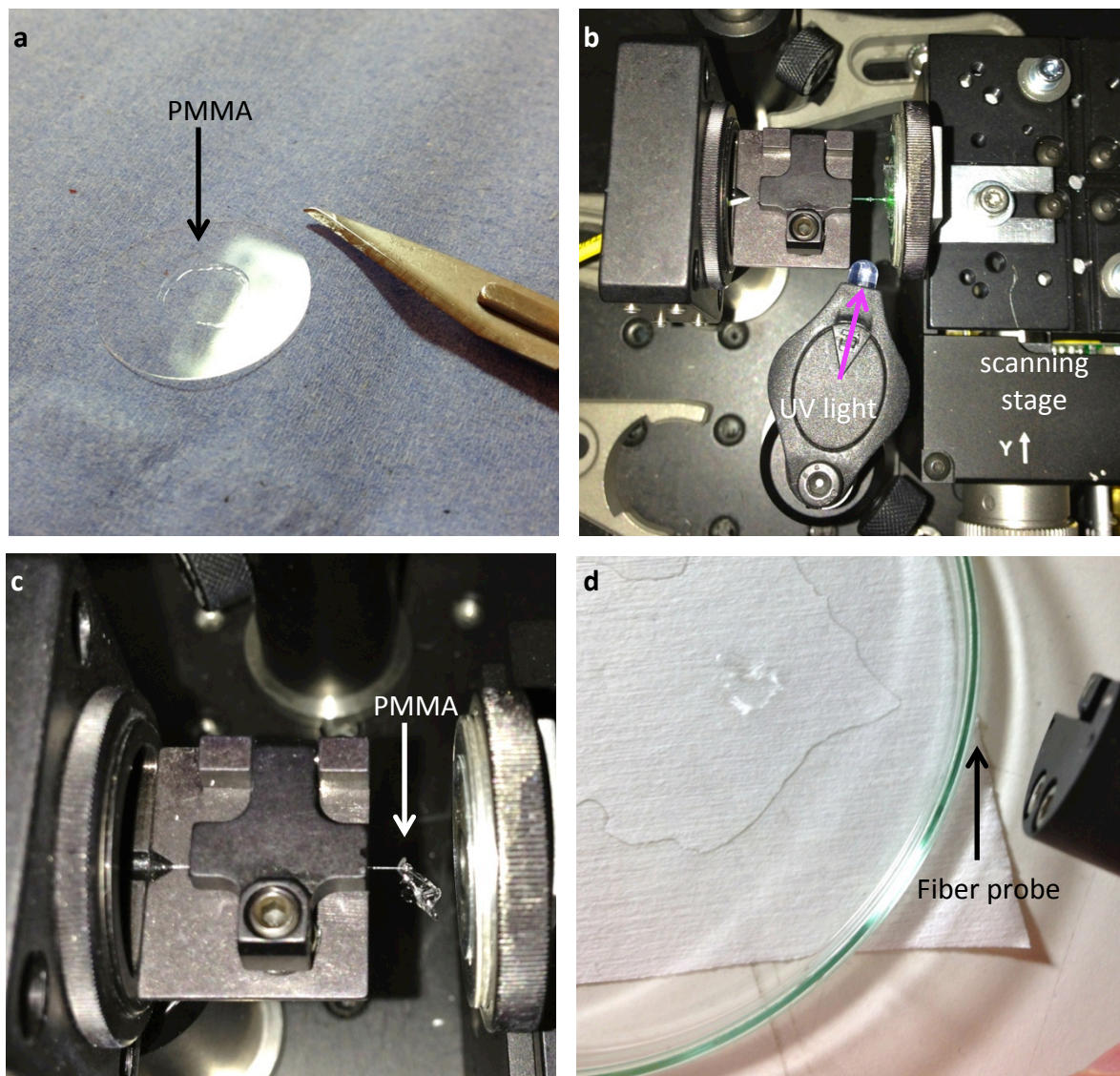


Figure 5.2.4 a) PMMA layer 'curls up' at the edges of the film, b) partial cure of the UV adhesive with accurate positioning of a single nanodiamond c) removal of the PMMA layer from the coverslip with the fiber d) dissolution of excess PMMA from the fiber

5.3 PROBE CHARACTERISATION

Optical microscope images were taken of the probe after adhesion of nanodiamond. x5 and x10 objective lenses were used. The images demonstrate the flexibility of the probe. Of the three probes made, all have residual adhesive approximately 600 μ m in diameter on the fiber (figures 5.3.1a & 5.3.2a). This was considered not to hinder the overall flexibility of the probe, or interfere with photoluminescence signal. However, it may be worth attempting to remove excess glue by soaking for an extended period in solvent. This was not attempted to prevent washing away of the adhered nanodiamond.

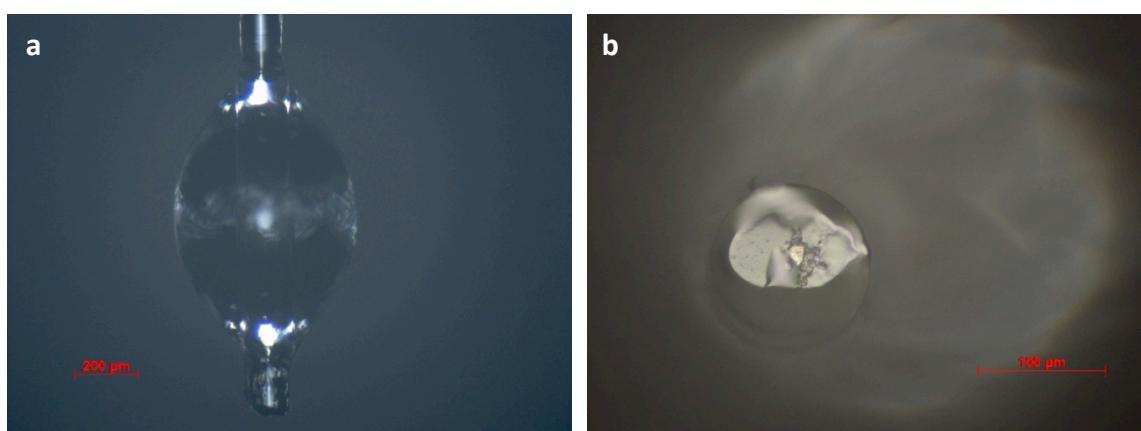


Figure 5.3.1 Optical micrographs of the probe with nanodiamond adhered. (a) is taken perpendicular to the fiber axis, and (b) excess PMMA looking along the z-axis of the fiber

Looking down the z-axis (figure 5.3.1b) a small amount of excess PMMA remains. This is smaller than the diameter of the fiber, and was removed by careful additions of solvent. However, this may have caused damage and contamination to the fiber tip itself.

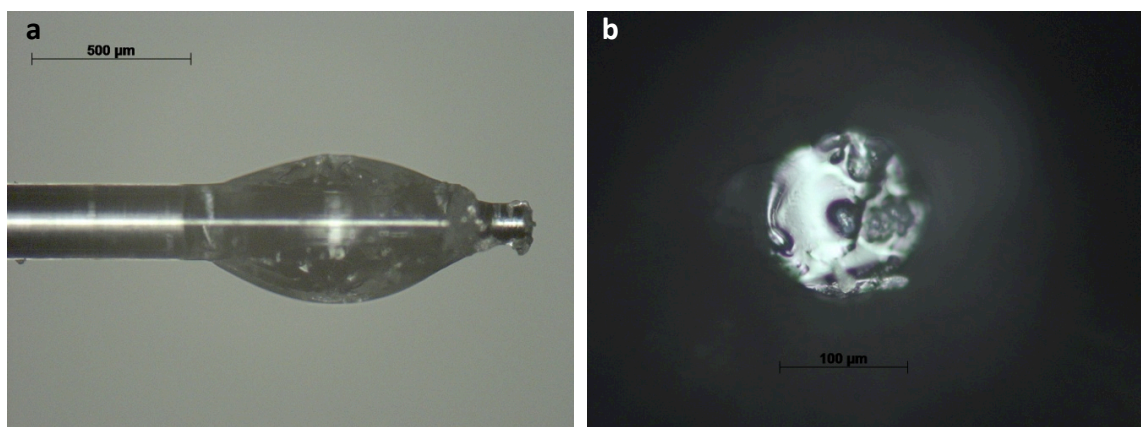


Figure 5.3.2 a) a second fiber probe with methanol dropped on the fiber tip to remove excess PMMA b) contaminated probe tip from excess PMMA removal

Spectroscopic measurements confirmed the presence of NV centres in nanodiamond on the fiber core. The photoluminescence signal corresponds to that found in the literature and also to the spectrum taken of the nanodiamond prior to adhesion to the fiber (see section 4.4).

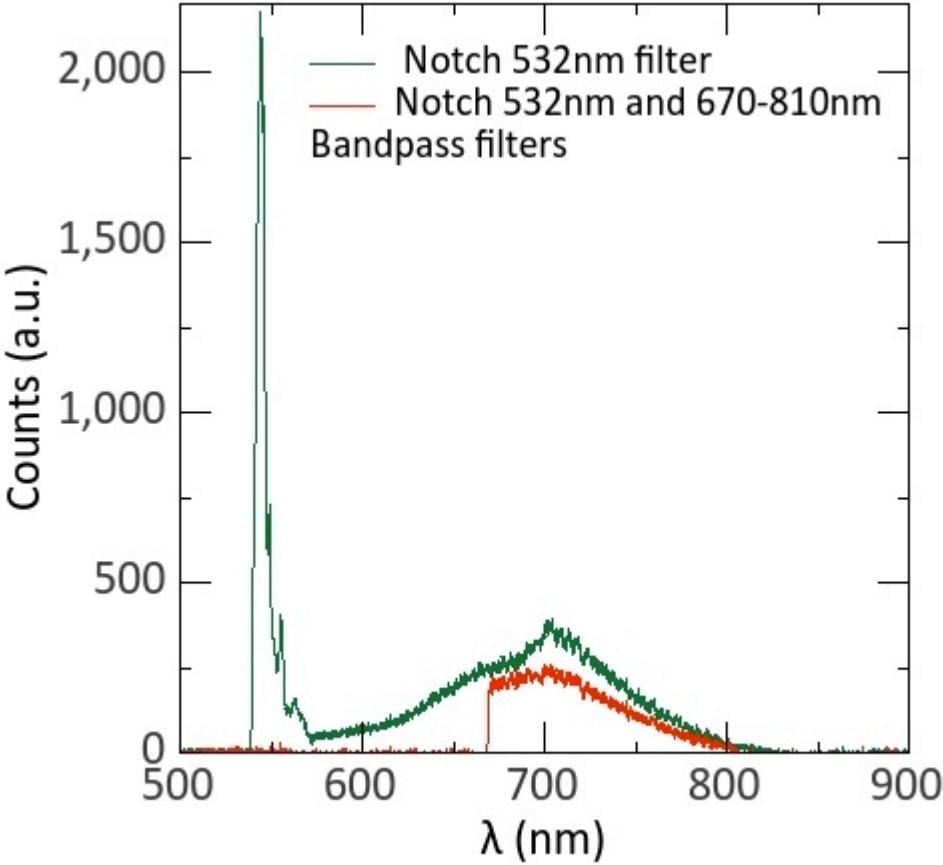


Figure 5.3.3 Spectrum taken of the probe with and without 670-810nm bandpass filter

6. MAGNETIC FIELD SENSING

6.1 QUENCHING PHOTOLUMINESCENCE

Having precisely positioned and successfully attached a nanodiamond to the tip of an optical fiber, the sensitivity of the probe magnetometer was then determined. In preference to setting up an ODMR experiment that requires precise positioning of expensive equipment, a simpler method of testing the probe's efficiency was adopted. An $8\% \pm 1\%$ drop in photoluminescence was recorded when a bar magnet was brought $<1\text{mm}$ from the probe. As the probe-magnet distance was increased, counts returned to their original value. This demonstrates the randomisation of the NV spin states, which occurs in the presence of a large magnetic field. The drop in PL is lower than the predicted 10% decrease found by Rogers *et al.*⁶⁰ The additional constant background autofluorescence signal from the fiber regardless of field strength decreases the recorded quench value. For this reason, the SM630HP fiber was used for probe fabrication in favour over the SM600 fiber for its lower autofluorescence for a given laser power (see section 3.4).

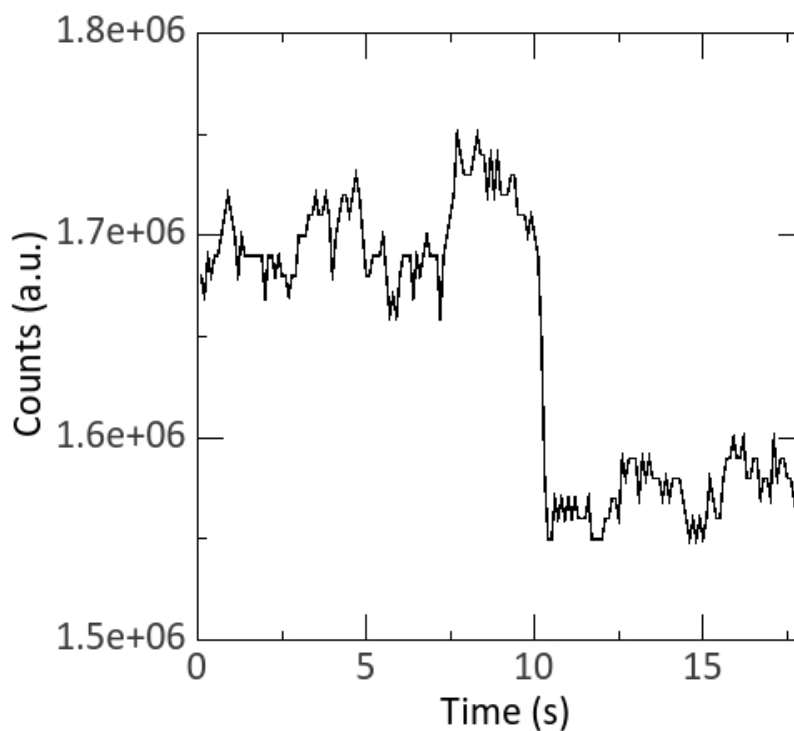


Figure 6.1.1 photoluminescence quenching in the presence of a large magnetic field $>100\text{mT}$ (time 10s). Photon count fluctuations are $\pm 18,000$, or $\pm 1\%$ at constant field

6.2 MAGNETIC FIELD DEPENDENCE

To perform a more quantitative analysis of the photoluminescence dependence with respect to magnetic field strength, a U-shaped electromagnet was used to create a field around the probe tip (figure 6.2.1). The electromagnet was calibrated using a hall probe held perpendicular to the field. The magnetic field strength created depends on the current applied to the coils surrounding the soft iron core, recorded by a Keithley closed loop device (see figure 6.2.2).

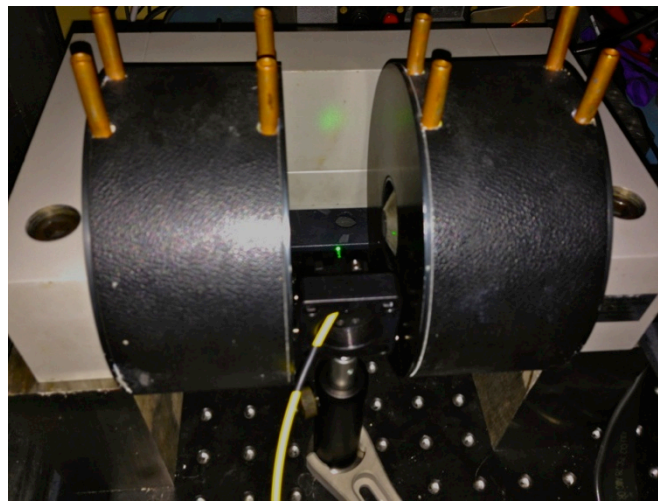


Figure 6.2.1 image of the electromagnet with the fiber probe between the coils

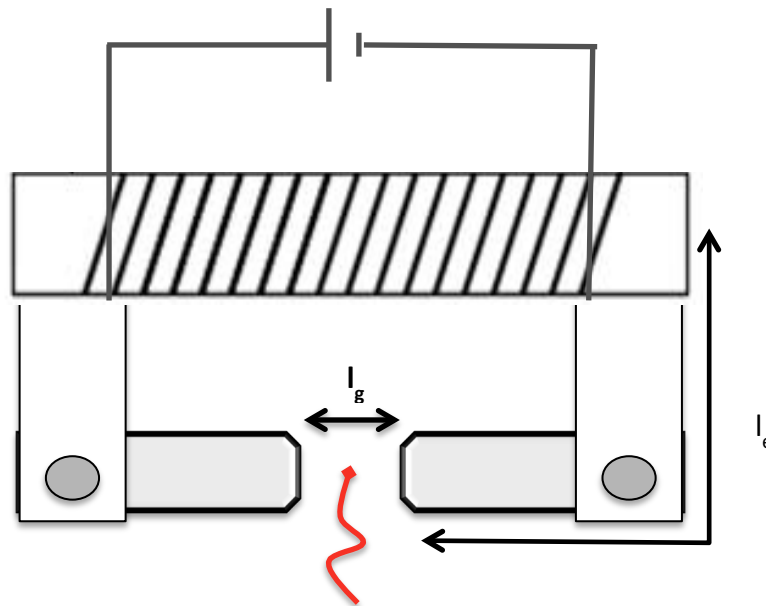


Figure 6.2.2 the electromagnet consists of a U-shaped soft iron core, which has high susceptibility and low retentivity and path length l_e . Decreasing the air gap l_g increases magnetic field strength

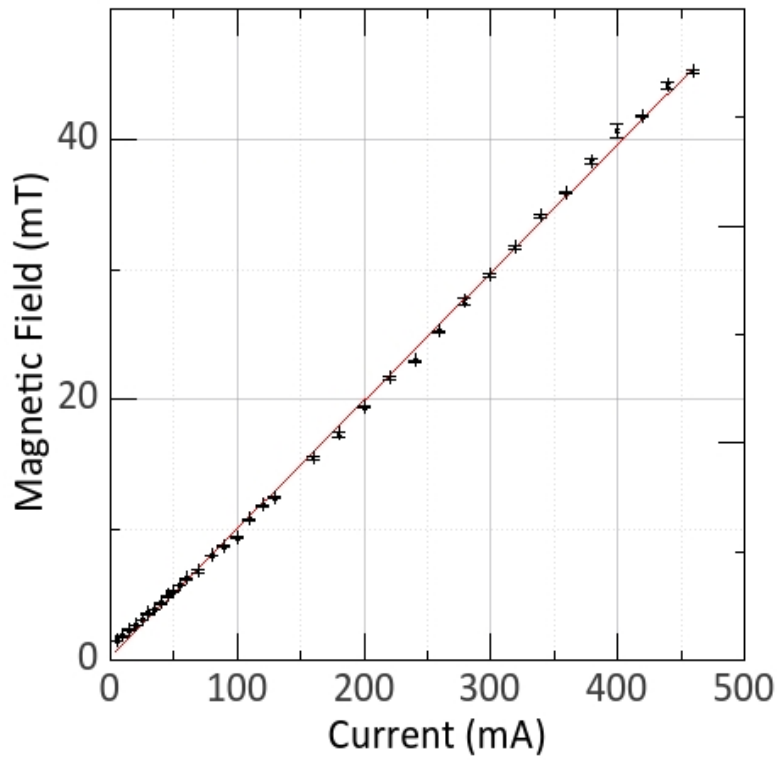


Figure 6.2.3 Plot of magnetic field strength as a function of current applied to the electromagnet coils. Error bars are taken from the standard deviation of magnetic field values

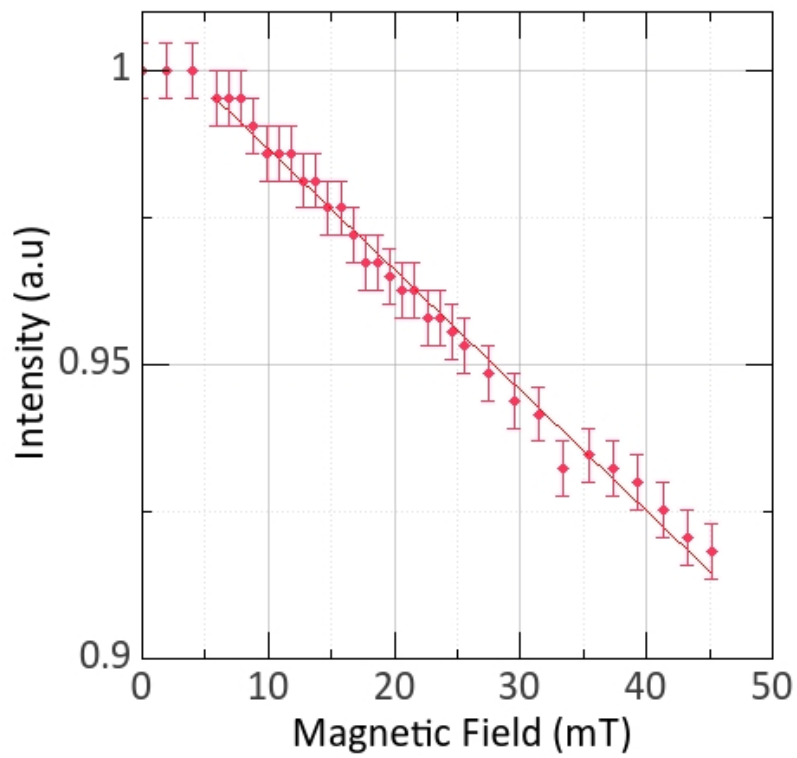


Figure 6.2.4 Graph of Magnetic field strength against intensity at 4cm core separation l_g

Magnetic field strength B increases linearly with applied current I ,

$$B = \frac{NI\mu}{l}$$

Where N is number of turns in the coil, μ is flux path permeability and l is flux path length. The magnetic field may thus be calculated for any current applied from the gradient, with error accounted for as the maximum and minimum gradient difference. The photon counts from the probe were then measured across this magnetic field range (figure 6.2.4).

The Keithley current source limit restricted the field maximum to 46mT for a 4cm electromagnet air gap. By altering the size of the air gap, a wider range of magnetic field strength could be generated. The calibration of the electromagnet is detailed in Appendix D. Core separation of 2cm was selected for appropriate B field range. Minimal flux leakage and less % error in magnetic field values recorded at smaller I_g improved the reliability of data collected.

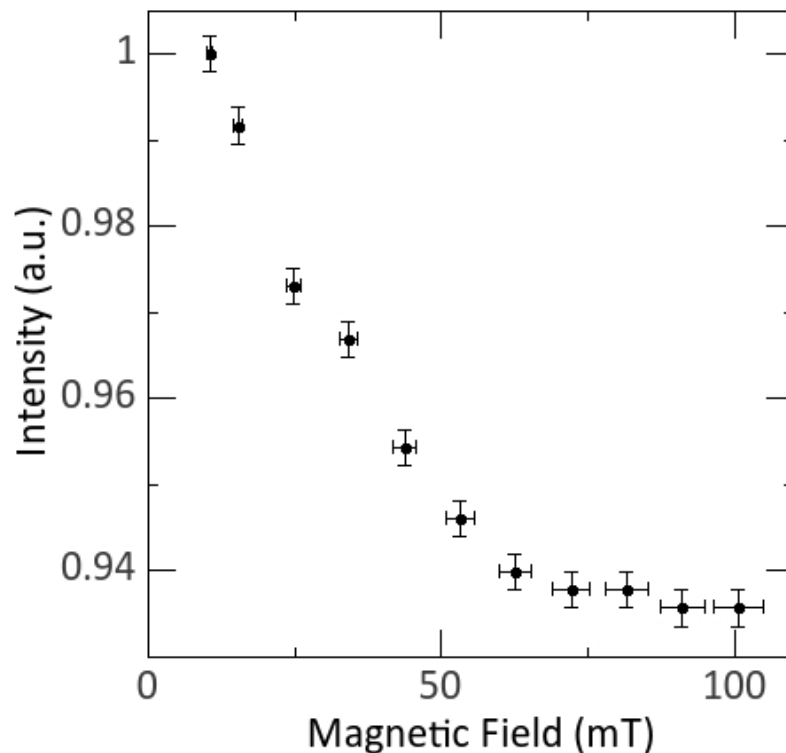


Figure 6.2.5 Graph of Magnetic field strength against probe photon count intensity at 2cm core separation I_g

Saturation occurs at high magnetic field, indicating total spin mixing. Unlike the drop in PL in figure 6.1.1, here the decrease is found to be just over 6%; less than before due to poor laser-to-fiber coupling efficiency and possible probe contamination over time. Results collected on a second probe at various laser powers showed PL % quenching to range 6.5-8.1% (see Table 6.2.1). At higher powers, although the intensity of PL increases, the fiber autofluorescence increases also. The fiber autofluorescence contributes to the total SPAD count signal from the fiber and therefore lowers the recorded value for % PL quench. Therefore to maximise the % PL quenching, optimum coupling and an appropriate laser power (3mW) must be used. To attain % PL quenching closer to the value reported in literature, and thus higher probe sensitivity, the fiber autofluorescence must be either accurately known for a given fiber coupling and laser power, or must be decreased to a negligible value.

Power (mW)	Counts at 0mA	Counts at 0.4mA	% PL quench	% error
0.5	497335	458776	8	1
1	948219	871928	8.1	0.8
3	2.46E+06	2.26E+06	8.1	0.5
4.5	3.23E+06	2.97E+06	8.0	0.4
6	3.96E+06	3.67E+06	7.2	0.4
12	6.40E+06	5.98E+06	6.5	0.5

Table 6.2.1 Laser powers and the PL quench associated with them. Counts averaged over 50s

The fluctuations in photon counts are the principal cause of noise, generating deviation of \pm several thousand counts depending on laser power (see Table 6.2.1). Due to the high intensity of this fluctuation, other noise contributions such as spin coherence time T_2 and background photon count variations may be considered negligible. From data taken in figure 6.2.5, the photon counts fluctuate by $\pm 0.4\%$ intensity when collected over 5s. This time period was selected because it incorporates 1-2 oscillations of the photon count rate, so noise is fully accounted for (referring to figure 3.5.1). For longer integration periods, the fluctuations vary more drastically due to thermal fluctuations and other effects mentioned in section 3, so reducing the magnetometer sensitivity. Therefore the sensitivity, η_B , described as the minimal DC magnetic field detectable δB_{min} for signal-to-noise ratio of unity:⁸⁴

$$\eta_B = \delta B_{min} \sqrt{\Delta t}$$

$$\begin{aligned}
\eta_B &= \frac{0.004\sqrt{\Delta t}}{\max \frac{dI_0}{dB}} \\
&= \frac{(0.004 \times \sqrt{5})}{0.00125} \\
&= 7.2 \text{mTHz}^{-1/2}
\end{aligned}$$

where I_0 is photon count rate, and dI_0/dB is the change in count rate with field strength. For different PL quench values, this value varies significantly due to the change in dI_0/dB . For example, the probe used in figure 6.2.4 has a higher sensitivity, because the gradient is steeper, hence δB_{\min} is smaller. The calculated sensitivity of this probe, with 8.2% PL quench and 0.5% noise, is $5.5 \text{mTHz}^{-1/2}$. This value is also dependent on laser power, and photon count integration time Δt .

Compared to sensitivities achieved by an NV-based magnetometer with a stable nanopillar AFM tip of $56 \text{nTHz}^{-1/2}$,⁴⁵ this sensitivity value is poor. Whilst this result does not exceed sensitivities for current instruments for field sensing, such as Hall probes which can sense down to $\sim 0.1 \text{mT}$ limit, it does show that an NV fiber based probe is sensitive to magnetic fields, and has potential for magnetic imaging. There is plenty of opportunity for this value to be reduced further. Reducing the fiber autofluorescence such that the % quench is greater and minimising photon count noise will improve the minimum detectable field, and thereby sensitivity (see section 7).

6.3 HARD DISK IMAGING

To test the feasibility of magnetic imaging with the probe, a sample of appropriate size and field strength was needed. Modern forms of data storage, including magnetic tape and hard disks, involve the spin orientations of paramagnetic particles. The particles in magnetic tape are $>100\mu\text{m}$ in size and therefore inappropriate for study with the scanning stage in my setup.

A commercial hard disk platter was sectioned using a rotating diamond blade saw. The platter is coated with ferromagnetic film on which data is recorded in magnetic bits. These bits are stored in magnetic concentric rings running around the platter known as tracks.

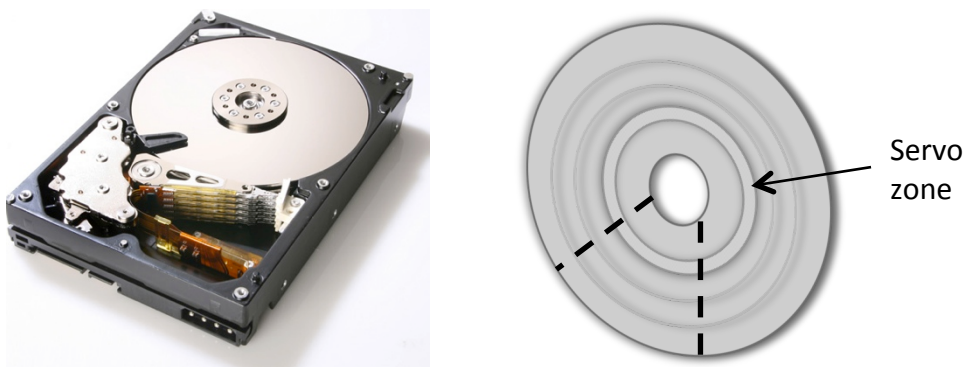


Figure 6.3.1 Left is an image of a hard disk with platter and read/write head,⁸⁵ and right a schematic of the platter with servo pattern ring, data tracks (not to scale) and sectioned region

Within the servo zone sit $\sim 10\mu\text{m}$ concave portions, which provide a read back system to indicate the position of the read/write head relative to the platter, known as a 'servo pattern'. Figure 6.3.2 shows optical images of the servo pattern. PL images of these portions were obtained using my probe magnetometer. Each domain corresponds in size to those in the optical images. Low laser power was necessary ($\sim 1\text{mW}$) to minimise background autofluorescence signal. Due to the physical curvature of the regions, the centre reflects the most light, whilst the edge both experiences lower incident power per unit area and also scatters incident light such that a lower intensity is collected by the fiber.

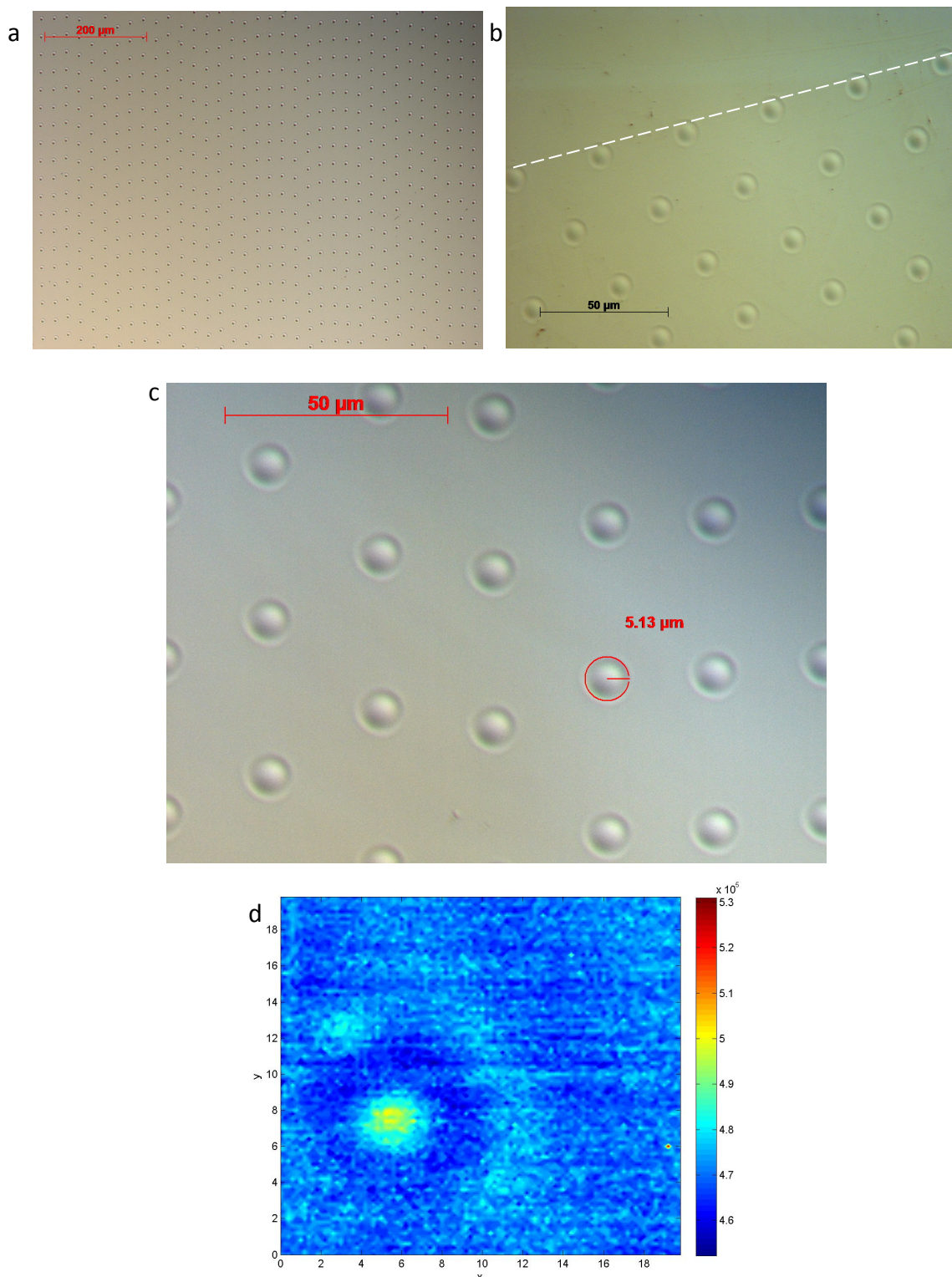


Figure 6.3.2 a) x10 objective lens optical image of servo pattern, b) servo pattern ring edge c) x50 lens optical image d) PL 20x20μm image of a servo pattern portion acquired using fiber probe, 50ms step-integration time 100 steps in x and y

The servo pattern was useful for improving the resolution of scanned images by changing the probe proximity and scan integration time. By optimising the servo pattern image, magnetic data tracks, as seen by Tetienne *et al.* (fig 2.6.2), became well defined (see figures

6.3.4 and 6.3.5. The tracks are in concentric rings around the platter, therefore different track line orientations are imaged as different regions of the disk are studied, for a given scan orientation (see figure 6.3.4).

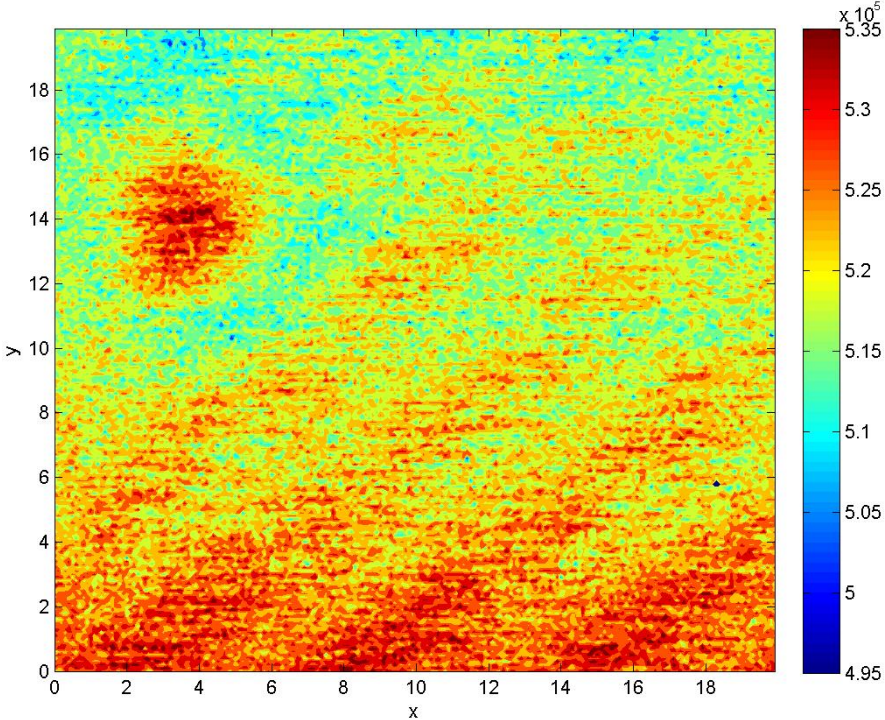


Figure 6.3.3 20x20μm scan of servo pattern (top left) and tracks for data storage

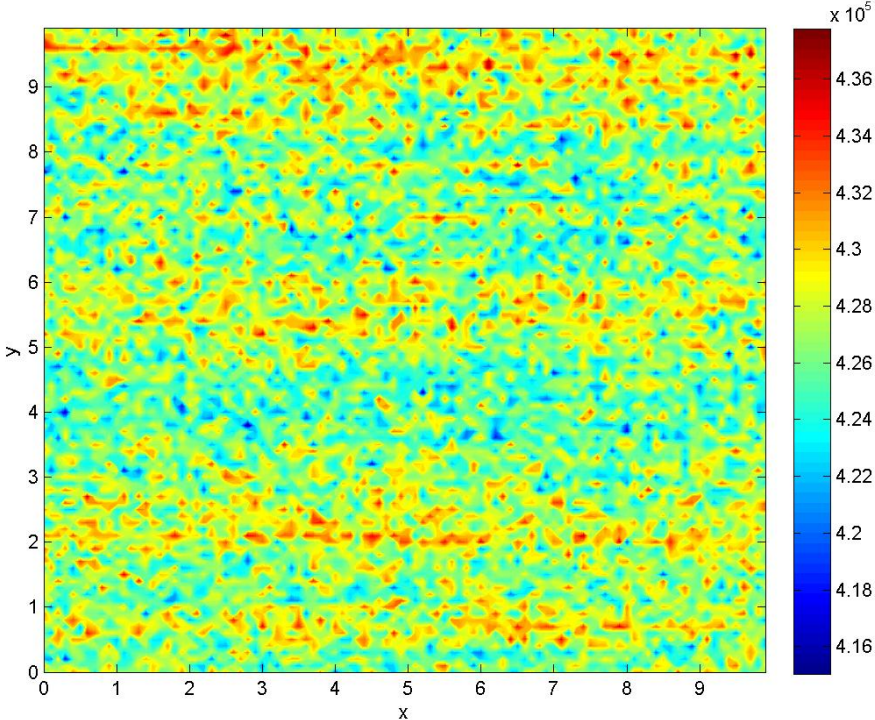


Figure 6.3.4 10x10 μm of track lines away from the servo zone. Change in orientation of the hard disk changes the orientation of the lines on the scanned image

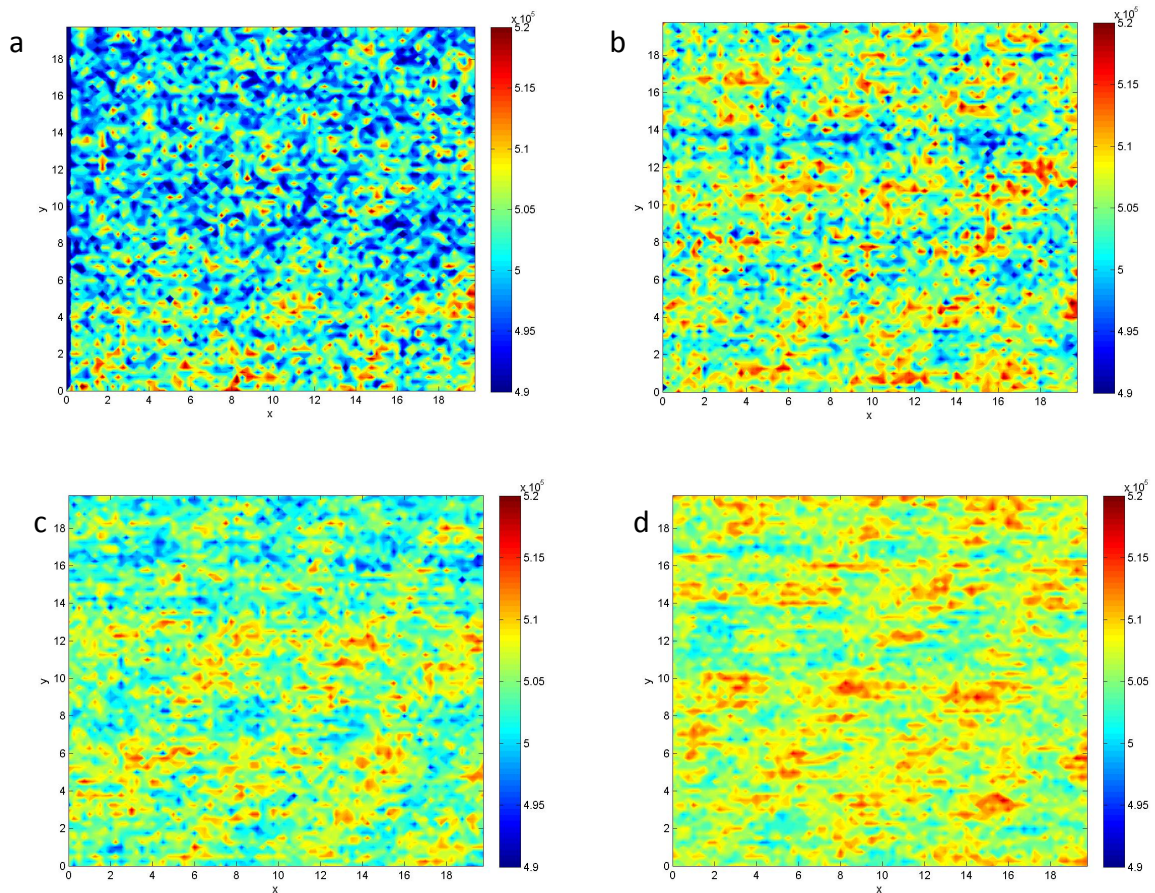


Figure 6.3.5 Track resolution in the images improves with increasing step-integration time, above showing times a) 15ms, b) 30ms, c) 60ms and d) 120ms

A box profile (figure 6.3.6) was taken as an average over 50 line profiles across the tracks using 'Image J' software on a rotated image, to overcome the high noise levels from the scan.

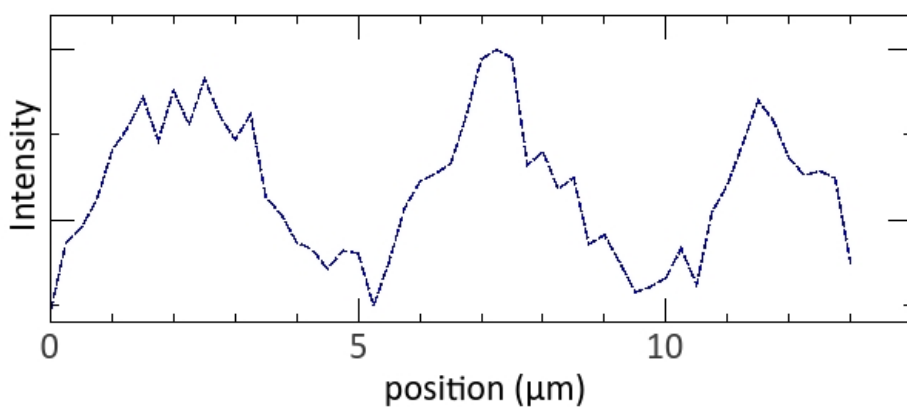


Figure 6.3.6 Box profile taken perpendicular to figure 6.3.5d track lines

By modelling a line profile as a sinusoidal variation in PL intensity using Matlab (figure 6.3.7), the wavelength of the track oscillations is estimated. The software calculates $\lambda=64$ pixels,

which converts to 86.4 pixels due to the 45° angle of the track lines. This corresponds to a magnetic track size of $4.3\mu\text{m}$; that typical of a hard disk made in 1990s.⁸⁶ This calculation is a rough estimate of track size, because the sinusoidal fit has a low R-square value, with fit accounting for only 52.6% of the variance. This is because a change in in-plane magnetisation between tracks means a stray field at the track boundary is detected, assuming the tracks are similar to those imaged by Tetienne *et al.* and Malentinsky *et al.*, and therefore the variation should not be sinusoidal at high enough image resolution. Additionally the noise level is considerably high, due to the small percentage changes in collected light intensity for change in magnetic field strength. Tetienne *et al.* reported the need for two consecutive bit regions to build up a strong enough stray field to induce a detectable change in PL quenching. This may be why individual bits are not detected on my scanned image also. Alternatively residual epoxy and possible probe contamination have prevented distinguishing individual magnetic bits; the resolution of the probe is not high enough.

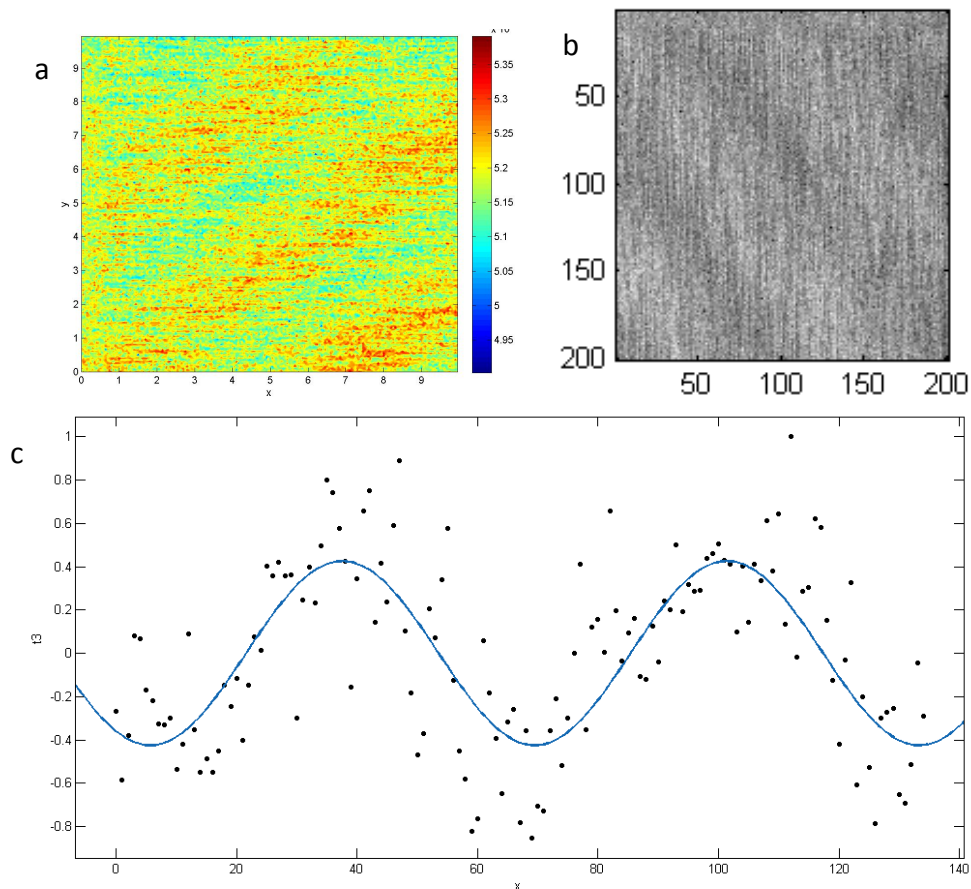


Figure 6.3.7 a) a $10 \times 10 \mu\text{m}$ PL image of tracks with data points used to generate b) a grey scale image with scale in pixels, which then creates c) a sinusoidal fit of intensity by taking 8 line profiles of equal angle and length across b

As explained in section 2.5, the NV centre in nanodiamond has been used for PL optical imaging for SNOM application. To confirm the magnitude and size of the track lines an MRFM tip may be used on the optical setup. The PL variations are due to magnetic field variation as opposed to reflections: no visible differences in physical appearance of the track lines are seen in figure 6.3.2c, or by using a fiber with no adhered nanodiamond. Additionally, the % drop in PL is a value one would predict for field strengths of a magnetic hard disk.³¹

Measuring the normalised PL intensity can in principle give a lower bound for B. However, parameters such as proximity of the probe tip to magnetic sample, NV defect transition rates, distribution and density of NVs and laser power coupling efficiency are not readily accessible. One can assume from the images that the dark regions correspond to a higher magnetic field, >5mT, which would be consistent with a hard disk field expected.³¹

7. CONCLUSIONS AND FUTURE WORK

Conclusions

A nanoscale probe magnetometer has been constructed. The probe was created by adhesion of a precisely positioned nanodiamond to a cleaved single mode optical fiber with 4.2 μm core diameter using a UV-curing optical adhesive. Core diameter determines the objective lens used for optimum laser coupling, and the lateral and axial resolution of the optical fiber for nanodiamond imaging. Nanodiamond concentration 1:5 spin coated on a PMMA solvent cast layer silica coverslip was found to be the most successful method for adhesion of an isolated nanodiamond.

Three probes were created by this method, with varying responses to magnetic field, but all displaying a 6-8.1% decrease in photon count intensity in the presence of a high magnetic field, depending on laser power and laser-light to fiber coupling. Variations in PL intensity may be attributed to a spin mixing effect at higher magnetic fields, resulting in quenched photoluminescence due to increased electron relaxation via intermediate singlet states. The probes manufactured have potential for 200nm spatial resolution and may record magnetic fields ranging between 5 and 65mT. Whilst this does not allow for weak magnetic field sensing, it does offer a probe method of study at room temperature. 4.3 μm wide magnetic bit tracks on a hard disk platter were imaged.

Fiber autofluorescence was found to be high in all optical fibers tested. Those fibers with doped cores have higher autofluorescence intensity, however the autofluorescence is believed to be largely due to impurities within the silica itself. Whilst this fluorescence did not initially inhibit probe magnetometry, in order to improve the probe resolution the autofluorescence signal must be lowered so as to discern the photoluminescence signal from fewer NV centres.

The sensitivity of the probe is currently limited by high background noise in the photon count signal. Large oscillations are present due to polarisation dependence of the laser light travelling along the fiber and interacting with the dichroic mirror. Small improvements in the

sensitivity of the probe have been made already by improving coupling efficiency of laser light to the fiber, and by using a high purity fiber, which gives slightly lower autofluorescence than a standard fiber. But in order to increase the sensitivity these oscillations must be minimised. Probe sensitivities were calculated to be in the $\text{mTHz}^{-\frac{3}{2}}$ range. This does not exceed current sensitivities of nanoscale magnetometers, however is the most sensitive probe to-date possessing both micrometer resolution and physical flexibility.

Future Work

Whilst the probe magnetometer has been realised, it has not yet proven to resolve on the nanoscale. Now that the method of nanodiamond adhesion to the optical fiber has been successful, excess adhesive should be removed from around the tip. It should then be possible for smaller nanodiamonds to be adhered to the fiber. The nanodiamond sample used contained an average particle size of 200nm, however much smaller particle sizes of $\sim 20\text{nm}$ are available.⁸⁷ This should lower the resolution limit of the probe, with the ultimate limit being a single NV centre – atomic scale resolution. As the number of NV centres decreases, the photon emission rate decreases also. The collection efficiency of the fiber may need improving, due to the glass acting as a reflective surface. In order to couple as much emitted light as possible, the fiber may be tapered, either using a heat-and-pull technique or by chemical etching.⁸⁸ By decreasing the diameter of the fiber to less than half the wavelength of the light incident, diffraction at the interface is prevented and light is more effectively collected.^{74,89} In addition, imaging smaller, less emissive nanodiamonds increases the need for fiber-sample proximity measurement. This could be achieved by adopting the tuning fork method adopted by Karrai *et al.* for SNOM use.⁵⁰

The autofluorescence noise from the fiber becomes an increasing challenge, as higher field sensitivities are required. Less fluctuation is necessary, which may be controlled by the introduction of an Acoustic Opto-Modulator (AOM) that alters laser light power depending on the oscillations in order to smooth the signal. Alternatively the polarisation dependence of the setup may be addressed by changing the fiber to one that maintains light polarisation more efficiently. There is a possibility of splicing a tapered fiber to a photonic crystal fiber⁷², or using shorted fiber lengths to reduce the background signal.⁷⁰ Sensitivity of the single NV

magnetometer would then be improved by extending spin- coherence times, by improving the nanodiamond purity, as mentioned in section 2.4.⁵⁸

Once the resolution and sensitivity have been improved further, a wider variety of samples may be studied and magnetically imaged. Should weak magnetic fields wish to be sensed and a single NV adhered to the fiber in the appropriate configuration, an ODMR sensing method could be introduced.

By taking the resolution down to a single NV centre, magnetic field lines in nanocomposites may be imaged. To image magnetic field lines in a high temperature superconductor, the fiber probe would have to be made to withstand sufficiently low temperatures at which the Meissner effect takes place. For application in the study of single protons and molecules, the adhesive used would have to be made compatible with the biological sample in question.

PROJECT MANAGEMENT FORM 1

Part II Project Description Form

After discussion with your supervisor YOU should complete this form and send a copy to the Academic Administrator's Secretary by Friday of 0th week of Michaelmas Term.

Name: Katherine Hazelton College: Mansfield

Address for correspondence: Mansfield College, Mansfield Road, Oxford, OX1 3TF

Contact telephone number: 07849753689

Title of project: Optical and Magnetic Characterisation of Colour Centres in Diamond

Supervisor: Jason Smith

What are the objectives of the project in order of priority? The end goal is to build a probe magnetometer using a nanodiamond on the end of an optical fibre. I need to construct the fibre PL set-up; measure PL through an optical fibre; attach a nanodiamond to the fibre end; measure ODMR; image a simple magnetic structure by scanning the sample and attempt to achieve a single NV probe limit

List the major milestones that must be accomplished in order to meet the objectives of the project

To have an operational scanning piezo stage with Labview interface, to image the PL from a nanodiamond colour centre, to detect magnetic resonance of the nitrogen vacancy centre through optical fibre and to attached an aligned nitrogen vacancy to the fibre end.

Are you working essentially on your own or as part of a team? If you are part of a team what is your role, and to what extent is the success of your project dependent on other members of the team?

It is principally a project I am working on full time, with the help and advice of other members of my research group

What resources (equipment, materials, technician support etc.) will you need?

Thorlabs equipment; laser, piezo stage, optical fibre, optics including mirrors, posts, filters, a dichroic, objective lens

Do you require any training to meet your objectives, e.g. in the use of specific experimental equipment or software, and how are you going to obtain that training?

Training with lasers, scanning confocal microscope, labview software, with the help of other members of the photonic nanomaterials group.

Complete the following plan for your entire project as you see it now. List each major task down the left hand column, and for each one draw a horizontal line to indicate the period you expect to allocate to it. For example, the final task, writing your thesis, is shown as occupying mid-April to mid-June.

Task	Oct	Nov	Dec	Jan	Feb	Mar	Apr	May	Jun
Set up optics and PL spectroscopy of optical fibre	xxxx								
Operational scanning piezo stage	xxxx								
PL of dense nanocrystal film through fibre – proximity monitoring	Xxx	xxxx							
PL imaging of NV centres		xxxx							
Optics theory	xxx	xxx	Xxx						
Magnetic resonance of NV through fibre			xxx	Xxx					
Attach and align NV to fibre end				xxx	xxx	xxx			
Writing up							xxxx	xxxx	xxxx

Has your supervisor completed a *Risk Assessment Form* about your project yet? Yes

Your signature:
Date: 10/13



Your supervisor's signature:
Date: 10/13



PROJECT MANAGEMENT FORM 2

1st Part II Project Analysis Form

Complete this form and send a copy to the Academic Administrator's Secretary by Friday of 6th week of Michaelmas Term

Name: Katherine Hazelton

Title of Project as given in your Project Description:

Optical and Magnetic Characterisation of Colour Centres in Diamond

Refer back to the project plan in your Project Description and list the goals you set for this term. Comment briefly on the extent to which you have achieved them.

I have successfully completed the optical set-up required for both SPAD and PL experiments, and carried out PL spectroscopy of the fibre. The scanning stage has been set up for use. However, due to time delays in the optical set-up, I have yet to measure the photoluminescence from a nanodiamond sample.

Identify clearly any difficulties you have encountered. Are they surmountable in the time available?

The alignment of my optical set-up has taken considerably longer than expected, due to the level of precision required. However I believe it is now well-aligned, thereby preventing problems from occurring at a later stage. Measuring PL from the optical fibre has also created unexpected difficulties due to the detection of a strong background signal.

State any refinements, modifications or replacements of the original objectives for your Part II project:

My objectives remain the same, however prior to attaching nanodiamond to the fibre end, I must ensure that the photoluminescence signal from a single NV centre is detected through the optical fibre. I must first try and remove background signal from the fibre, and then attempt to detect PL from a strongly fluorescing sample, before trying to isolate a single NV defect for fibre attachment.

Are you intending to change the title of your project? If so, state the new title:

*My project title has become, more specifically, 'building a probe magnetometer using nanodiamond on the end of the optical fibre', instead of characterisation of diamond NV centres**

Have the training needs you identified in the Project Description been met, and have you identified any further training requirements?

Yes

Tick the appropriate box. Do you have

	None	Some	Sufficient
Results		x	
Analysis of results	x		

Do you have any other comments you wish to make?

None at present

After looking at the project plan in your Project Description complete the following project plan for the remainder of your Part II.

Task	Dec	Jan	Feb	Mar	Apr	May	Jun
Address problem of background signal from fibre	xx						
Measure PL from a strongly fluorescing sample	xxxx						
PL imaging of NV centres		xxxx					
Magnetic resonance of NV through fibre			xxxx				
Attach and align fibre to end			xxxx	xxxx			
Optics theory	xxxx	xxxx	xxxx	xxxx			
Writing up					xxxxx	xxxxx	xxxxx

General comments by the supervisor:

Your signature: *Katherine Hazelton*

Date: 19/11/13

Your supervisor's signature: *J. Sill*

Date: 19/11/13.

PROJECT MANAGEMENT FORM 3

2nd Part II Project Analysis Form

Complete this form and send a copy to the Academic Administrator's Secretary by Friday of 6th week of Hilary Term

Name: Katherine Hazelton

Title of Project: *Building a probe magnetometer using nanodiamond on the end of an optical fibre*

Refer back to the project plan you made last term and list the goals you set for this term. Comment briefly on the extent to which you have achieved them.

I have largely achieved the goals I set myself at the end of last term: I have addressed the problem of fiber background signal, having to effectively disregard it to continue with the main objective of the project. I have detected and imaged PL from quantum dots and NV centres in a nanodiamond sample using the piezo scanning stage. I am currently attempting to adhere the nanodiamond to the fibre tip. I have not yet detected magnetic resonance of the NV centre through the fiber, because I came to the conclusion that attachment of the nanodiamond was of more priority at this stage.

Identify clearly any difficulties you have encountered. Are they surmountable in the time available?

Lack of awareness of fibre- sample proximity has resulted in frequent damage to the fibre end, caused by collision. Therefore the fiber must be replaced or recleaned. I have begun to use cleaved fiber, but regular re-cleaving and re-aligning has proved to be quite time consuming. Once I have a nanodiamond attached to the tip, this issue will be eradicated. I have therefore decided to prioritise attaching the nanodiamond to the fibre tip. Taking an ODMR measurement should be achievable once the nanodiamond has been well-attached to the fibre tip.

State any refinements, modifications or replacements of the objectives you set for your Part II project:

Whilst I am still aiming to produce a magnetometer, due to time constraints of the project I believe that more progress may be made by attaching the nanodiamond to the fiber, prior to attempting to detect ODMR of the NV centres whilst they are still on the substrate. Hopefully attachment of the nanodiamond can be achieved with relative ease, so that I can take ODMR data.

Are you intending to change the title of your project? If so, state the new title:

No

What is the title of the talk you will give to the Department?

Constructing a probe magnetometer using photoluminescence from nitrogen vacancy centres in nanodiamond

Have all your training needs for this project now been met?

In order to take ODMR measurements, I will need training to use the ODMR equipment. In addition I may use the scanning confocal microscope to study the fibre end, which I may need some supervision with, although I have had some prior training earlier this year.


Tick the appropriate box. Do you have


	None	Some	Sufficient
Results		x	
Analysis of results		x	

Do you have any other comments you wish to make?

No

General comments by the supervisor: Kate is making good progress and, with a following wind will complete the goals of the project.

Your signature: 
Date: 24/02/14

Your supervisor's signature: 
Date: 24/2/14.

PROJECT MANAGEMENT

Day-to-day

To achieve the goals set out at the start of the project, it was necessary to manage and organise my work on a day-to-day basis. An initial timescale was laid out with principle milestones laid out. Project management forms aided in the review of progress, and the need to adapt targets due to unforeseen challenges. In the initial stages of the project, my supervisor guided me through the goals of the project and the lab work that should be carried out. Despite working largely independently, at the start of the project I requested help from other group members due to their expertise in the optical equipment and setup. Optics classes were held on a weekly for basis for group members (run by Dr Aurelien Trichet, Dr David Coles and Dr Jason Smith), and were very beneficial; aiding understanding in fundamental theory, laser alignment, beam quality and diamond's electronic structure.

Group meetings on Monday mornings were a good opportunity to display and discuss results, to gain opinions from other members of the group regarding challenges to overcome, and also a time to set out a week schedule to follow. On occasion I would seek out my supervisor for advice on results I struggled to comprehend, and how to approach subsequent lab work that would be challenging. These meetings would often spur me on to read more in the literature, and develop my own method for carrying out lab work successfully (e.g nanodiamond-adhesion methodology).

Ordering Equipment

Firstly, the equipment for my optical setup, such as posts, holders, stands, fibers, stage controllers etc. had to be ordered, with a delivery time of a few weeks. To make use of this time, I used Thomas Reuter's web of science and Google scholar to understand NV centre theory and to research literature on current methods of magnetometry. I also ensured I had all the appropriate safety training for the equipment I was to be using. This included signing up to a laser safety talk in the physics department prior to the use of lasers in the lab. I was

informed of the location of various laser keys, and the sensitivity of the photon detectors and spectrometer. Such expensive equipment had to be handled with care. I was aware of the different chemicals within the lab, including liquid nitrogen, chloroform and non-halogenated chemicals, and the potential hazards associated with them. For requisitions from Thorlabs at later stages in the project, time was utilised by becoming familiar with software such as 'Qti plot' and 'Image J' for data analysis and graphical representation, 'VESTA' for ball and stick models, and 'Corel CAD' for representing tome-built confocal microscope setup and the spectrometer.

On occasion, a simple test was necessary to run, and rather than making an order for new equipment, I would be try to be resourceful with what was already available to me. For example, when testing the study of nanodiamond on a polymer substrate, I initially used broken up sample boxes, before realising surface curvature was too much of a barrier to progress. The source of UV light used to cure the adhesive was from an LED, which I purchased from an online supplier, originally made for checking bank notes.

Data management

Once I began to collect data, I logged it by hand in a lab book, and electronic figures and data were saved to the group server. To mitigate any data losses caused by potential hardware damage, I frequently backed it up onto my memory stick, and also transferred it to Dropbox several times a week. All my nanodiamond samples were stored in a sample box, and labelled appropriately should I require them for later use.

Challenges and re-evaluation of objectives

During the course of the project, several unexpected difficulties were encountered. The autofluorescence from the fiber was not well reported in many papers, and was found to be much higher than expected. Therefore more time was spent characterising the setup and different fibers available. The optical setup took an extended period of time, as I became accustomed to the method of laser alignment. It was imperative to remain patient and

persevere. At times, it was necessary to realise when a method had to be adapted because sufficient time had been spent trying to succeed. I would become frustrated with lab work and repetitive difficulties with the equipment: in optics this would often result in little progress, with precision and care needed to succeed. At these times I would refer back to reading literature as a break, so time in the lab was not wasted. After collecting data for a particular optical setup, I would analyse the data before making adjustments to the setup, to ensure that no further data would need to be collected for that optical configuration. Because fiber coupling was time-consuming, this was important for effective time management.

The initial aim of my project was to isolate a single NV in nanodiamond, and attach it with specific orientation such that ODMR spectroscopy could be carried out. However, due to fiber background signal and proximity uncertainty, this target became unrealistic in the given time frame and with the available resources. As a result, after testing multiple conventional fibers, a decision was made to use an ensemble of NVs in a single nanodiamond, because the signal-to-noise was high enough for detection. ODMR signals are less sensitive as more NVs are present, so all-optical imaging by PL quenching was more appropriate as a method of magnetic field sensing. It was a less time-consuming method than ODMR for testing the probe magnetometry potential.

As time was missed in the lab for job applications, I came in weekends to complete experiments. This was also necessary to obtain sufficient time periods on equipment, such as the spectrometer, which is used by several group members.

With hindsight I would have characterised my setup more effectively prior to taking any data. Although I characterised my setup and fiber sufficiently in order to continue onto later stages of lab work, such as nanodiamond study, before writing the report I had to re-characterise the setup to interpret all of my results correctly. Whilst some results seemed less impressive, had I been fully aware of all of the setup components, I could have carried out more conclusive experiments. For example, had I been aware of the beamsplitter losses to the spectrometer as I was carrying out autofluorescence studies of the fiber, I had the time to swap it for a mirror, and determine the full spectra of the background fiber counts.

As it was, I determined the autofluorescence was in the NV spectra range, but it may have been a more appropriate test to directly compare photon count rates.

Thesis Writing

When it came to writing my thesis, in Hilary term I began collating all of the data I had collected thus far. This gave me the opportunity to structure my report into relevant sections, which then gave me further clarity in my lab work and literature analysis. I documented my findings from the literature using refworks and an excel spreadsheet, which greatly aided the writing of my literature review in particular. By Easter I had written drafts for the introduction, background theory (taken largely from notes made in optics theory classes back in Michaelmas term), literature review, and optical setup. The part II talk in Trinity term gave me a deadline to have a clear and concise description of the project's engineering context and the relative successes and setbacks my project had posed. I continued with lab work in conjunction with writing up on weekends and in the evenings until three weeks before thesis submission to focus my efforts on producing a well-written thesis with accurate analysis of my findings and methods.

Overall I would say I have managed my time efficiently over the course of the year. On occasion lab work has felt unproductive and slow, but on reflection I successfully achieved the goals of the project, despite unexpected challenges along the way. I worked largely independently in both the lab and in writing my thesis, and feel I have gained a full experience in working in a research group on cutting-edge scientific work.

APPENDIX A

Acronyms

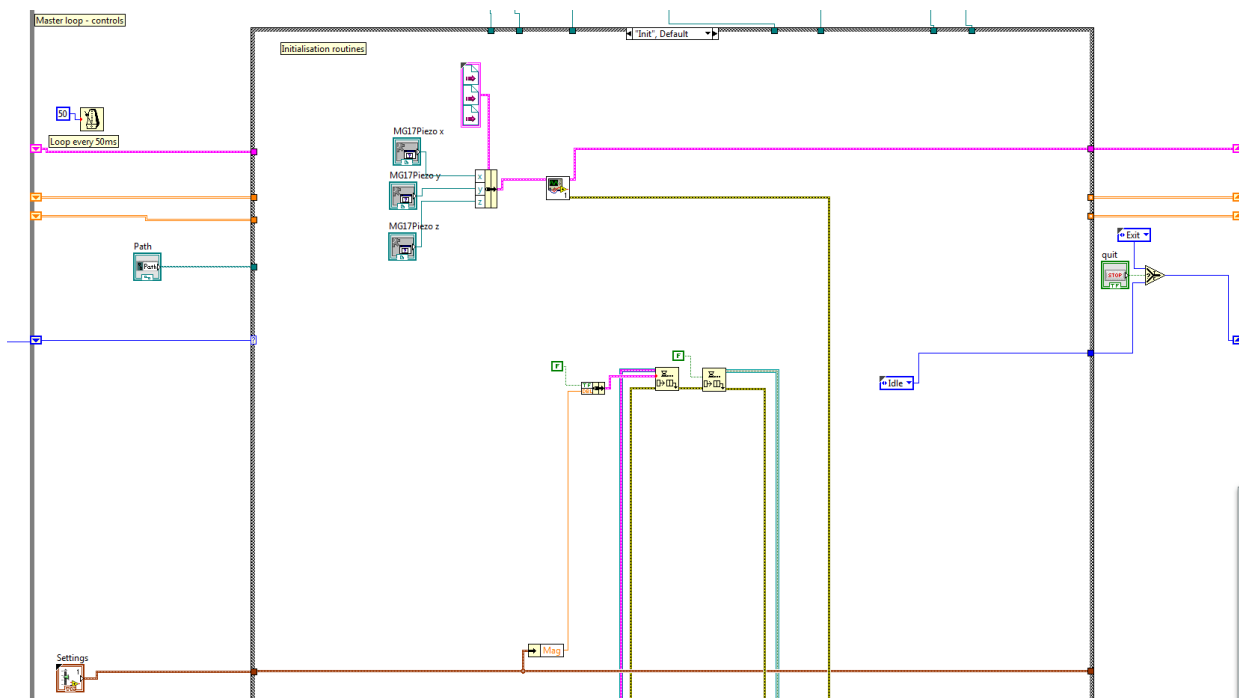
NV	Nitrogen vacancy centre
NV ⁰	neutral NV
NV ⁻	negatively charged NV with additional electron
PL	Photoluminescence
ZPL	Zero Phonon Line
PSB	Phonon Side Band
m _s	spin projection along the intrinsic quantisation axis of the NV defect [111]
ISC	Intersystem crossing
MRFM	Magnetic Force Resonance Microscopy
SQUID	Superconducting Quantum Interference Device
ODMR	Optically detected magnetic resonance
AFM	Atomic Force Microscopy
CCD	Charge Coupled Device
MFD	Mode Field Diameter
DAQ	data acquisition
LED	light emitting diode
UV	ultra violet
SPAD	Single photon avalanche diode
NA	Numerical Aperture
CVD	Chemical Vapour Deposition
HPHT	High Pressure High Temperature
SNOM	Scanning Near-field Optical Microscopy
MFD	Mode Field Diameter
AOM	Accoustic Opto Modulator

APPENDIX B

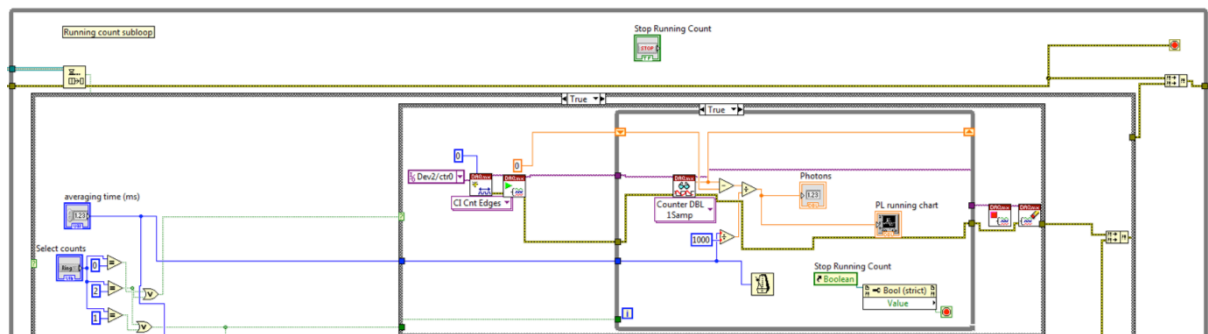
Labview Software for Scanning Piezo Stage

The software was written thanks to Matthew Wincott.

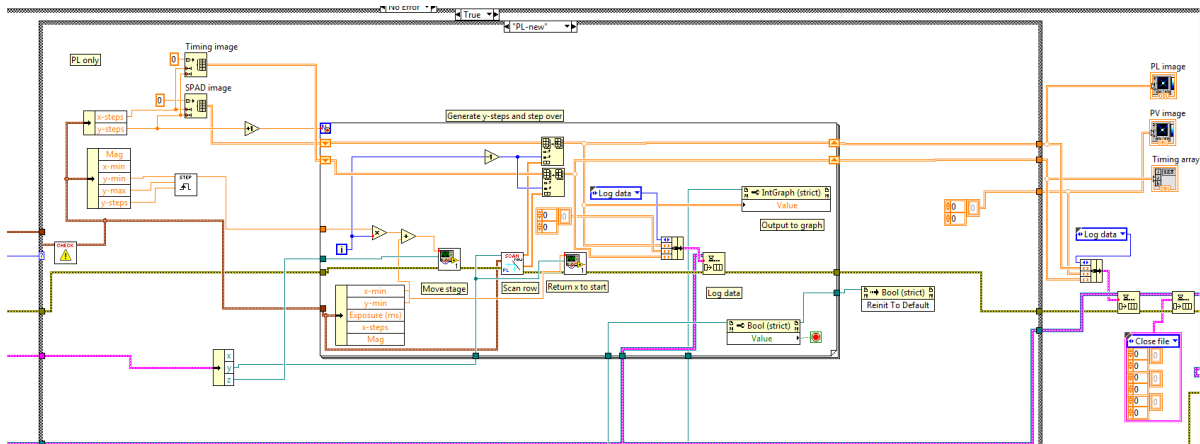
The initialisation process begins with a while loop path on 'scan' setting. Within the while loop is the programming software for the x, y and z piezos.



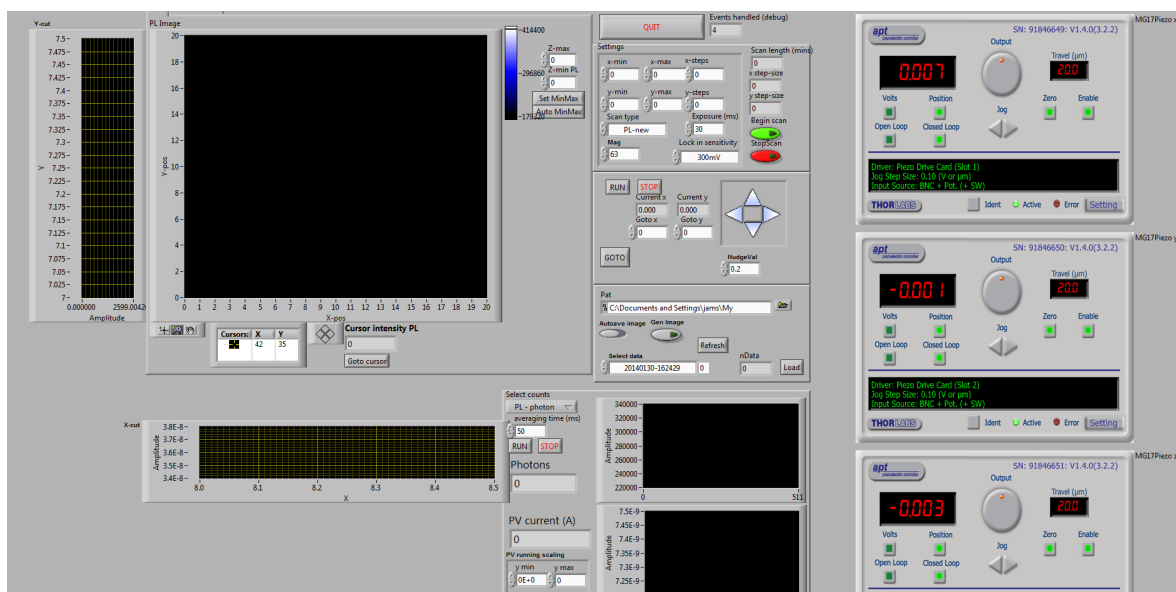
Running counts



A running count sub loop enables the photon count rate to be monitored without a scan running. Count edges are monitored and recorded as digital data by the DAQ card.



Once the software has been set to scan, the stage moves in increments along the x direction, before resetting to the start and moving one increment in y. Data is logged and outputted as a graph.



Above is the front panel interface for the user. Step size, scan size and exposure time (ms) may all be varied. The scan size was restricted by the limit of piezo movement, 20x20microns. Charts may then be saved to the desktop. Running photon counts may be monitored, and on the right is the piezo controller interface.

APPENDIX C

Error Analysis

1. Incident laser power on the fiber was measured prior to the dichoric mirror. The Thorlabs digital power meter has measurement uncertainty $\pm 3\%$.

2. The Keithley has fluctuations $\pm 0.012\%$,

3. To measure fluctuations in photon count rate, data was taken at constant power over an extended time period (~ 100 s). This data was then exported from labview to qtiplot, and the average and standard deviations for each point calculated by the program.

The standard deviation is the square root of the variance, which is the average of the squared differences from the mean value. So for data with values x_1, x_2, x_3, \dots

the mean $\bar{x} = \frac{x_1 + x_2 + x_3 + \dots}{n}$, where n is the number of values taken.

The variance is then $\sigma^2 = \frac{(x_1 - \bar{x})^2 + (x_2 - \bar{x})^2 + (x_3 - \bar{x})^2 + \dots}{n}$

and hence the standard deviation $\sigma = \sqrt{\frac{(x_1 - \bar{x})^2 + (x_2 - \bar{x})^2 + (x_3 - \bar{x})^2 + \dots}{n}}$

4. When calculating the magnetic field strength, the Hall probe had precision to ± 0.01 mT. However, when measuring the value, exact position of the probe in the air gap altered the field recorded. Therefore 3 readings of magnetic field strength were taken, and the standard deviation measured for each current value.

5. To find the magnetic field at a given current, the gradient of the calibration curve was used. The error in the field value was then the gradient error, calculated by plotting the maximum and minimum gradients (using $\pm\sigma$) and taking the difference. Lines of best fit were plotted in qti plot from the linear regression equation, $y = ax + b$ where

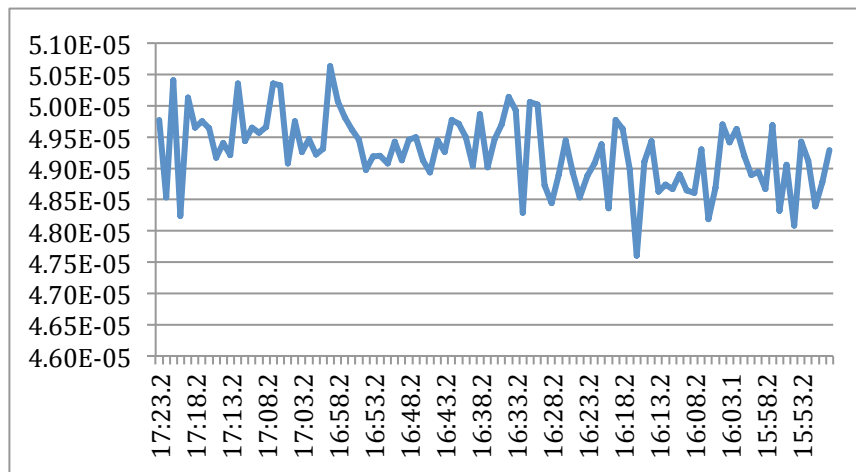
$$a = \frac{(\sum y)(\sum x^2) - (\sum x)(\sum xy)}{n(\sum x^2) - (\sum x)^2} \quad b = \frac{(n \sum xy) - (\sum x)(\sum y)}{n(\sum x^2) - (\sum x)^2}$$

6. Error in fluctuation of laser was found by averaging data across an extended time period for the number of oscillations, often 50-100s

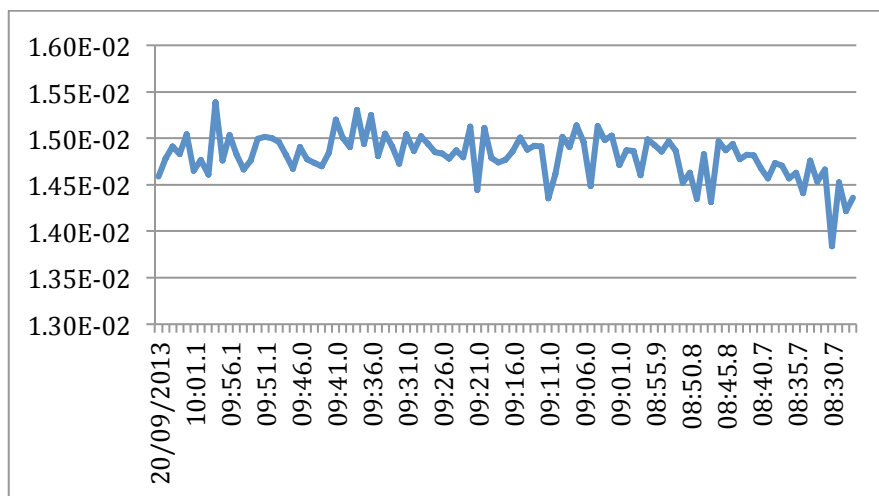
APPENDIX D

The 200mW laser power stability was characterised before I joined the group by Alex Powell. Data was recorded in September 2013. His data confirms that the laser provides stable power, and oscillations from the signal collected in my experiments are due to polarisation effects of the light and thermal effects in the optical fiber as explained in section 3.

At low laser power, average $49.1\mu\text{W}$ the power recorded over 2 minutes has a standard deviation of just 1%.



Similarly at high laser power, average 14.8mW , the standard deviation is 1.6%. This is higher than at low power, but not as high as found with an optical fiber in the setup.



APPENDIX E

The current I , and the relative permeability of the iron core and air gap μ , govern the field strength generated by the electromagnet. The majority of circuit reluctance originates from the air gap, and therefore by narrowing the air gap the magnetic field increases at constant current. The magnetic field strengths achievable were recorded for four air gap lengths (figure 6.2.5).

The reluctance R is a sum of the total reluctance of the iron core and air gap,

$$\begin{aligned} R_{total} &= \left(\frac{l_{total}}{\mu A_e} \right) \\ &= \left(\frac{l_e}{\mu_0 \mu_r A_e} + \frac{l_g}{\mu_0 A_e} \right) \end{aligned}$$

where A_e is the effective area of flux lines and the permittivity of free space $\mu_0 = 4\pi \times 10^{-7}$.

We can now adapt our field equation, such that

$$B = NI \left(\frac{\mu_0}{\mu_r l_e} + \frac{\mu_0}{l_g} \right)$$

The iron core reluctance term may be neglected in the case of a large air gap due to the high permeability of the soft iron core μ_r . One would predict a linear relationship between calibration B vs I gradients (figure 6.2.5) against $1/l_g$ since $N\mu_0$ is constant. However at high separation this does not apply due to flux leakage: flux field lines leak at the core edges with larger air gaps, and therefore the magnetic field strength is lower than predicted. The value for the gradient is therefore lower and hence the relationship becomes non-linear at lower $1/l_g$ (fig 6.2.6).

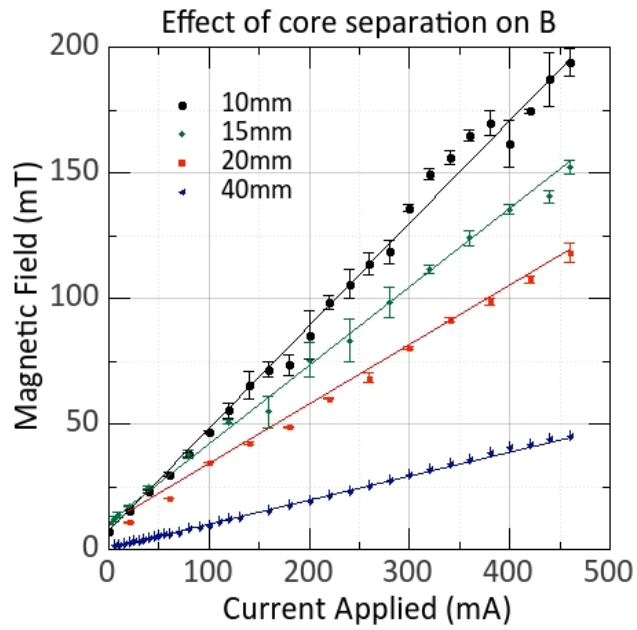


Figure E.1 Changing core separation and its affect on the magnetic field generated with applied current

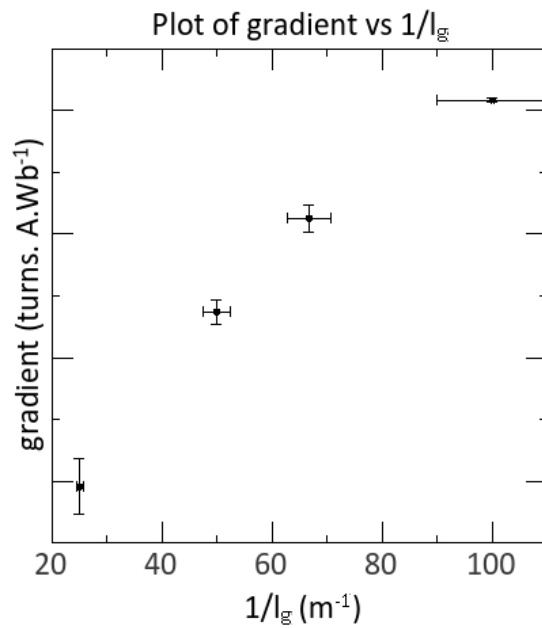


Figure E.2 Determining the relationship between core separation and field generated

BIBLIOGRAPHY

- 1 'Synthetic Diamond - Emerging CVD Science and Technology', Spear and Dismukes, Wiley, NY (1994)
- 2 Aharonovich, I., Greentree, A.D. and Praver, S. (2011) Diamond photonics. *Nature Photonics*, 5 (7), pp. 397-405.
- 3 Ashcroft & Mermin (1976) *Solid State Physics*
- 4 Davies, G. and Hamer, M. (1976) Optical studies of the 1.945 eV vibronic band in diamond. *Proceedings of the Royal Society of London. A. Mathematical and Physical Sciences*, 348 (1653), pp. 285-298.
- 5 Doherty, M.W., Manson, N.B., Delaney, P., Jelezko, F., Wrachtrup, J. and Hollenberg, L.C. (2013) The nitrogen-vacancy colour centre in diamond. *Physics Reports*, 528 (1), pp. 1-45.
- 6 Rabeau, J., Huntington, S., Greentree, A. and Praver, S. (2005) Diamond chemical-vapor deposition on optical fibers for fluorescence waveguiding. *Applied Physics Letters*, 86 (13), pp. 134104.
- 7 Rabeau, J., Stacey, A., Rabeau, A., Praver, S., Jelezko, F., Mirza, I. and Wrachtrup, J. (2007) Single nitrogen vacancy centers in chemical vapor deposited diamond nanocrystals. *Nano letters*, 7 (11), pp. 3433-3437.
- 8 Hazen, R.M. (1999) 'The Diamond Makers' Cambridge, UK: Cambridge University Press
- 9 Mita, Y. (1996) Change of absorption spectra in type-Ib diamond with heavy neutron irradiation. *Physical Review B*, 53 (17), pp. 11360.
- 10 Meijer, J., Burchard, B., Domhan, M., Wittmann, C., Gaebel, T., Popa, I., ... & Wrachtrup, J. (2005). Generation of single color centers by focused nitrogen implantation. *Applied Physics Letters*, 87(26), 261909.

-
- 11 Mainwood, A. (1994) Nitrogen and nitrogen-vacancy complexes and their formation in diamond. *Physical Review B*, 49 (12), pp. 7934.
 - 12 Martin, J., Wannemacher, R., Teichert, J., Bischoff, L., & Köhler, B. (1999). Generation and detection of fluorescent color centers in diamond with submicron resolution. *Applied physics letters*, 75(20), 3096-3098.
 - 13 Bradac, C., (2012) The Properties of Nitrogen Vacancy Centres in Nanodiamond, Thesis submitted to Macquarie University, NSW, Australia, internal
 - 14 Vlasov, I.I., Shenderova, O., Turner, S., Lebedev, O.I., Basov, A.A., Sildos, I., Rähn, M., Shiryayev, A.A. and Van Tendeloo, G. (2010) Nitrogen and Luminescent Nitrogen-Vacancy Defects in Detonation Nanodiamond. *Small*, 6 (5), pp. 687-694.
 - 15 Greentree, A., Aharonovich, I., Castelletto, S., Doherty, M., McGuinness, L. and Simpson, D. (2010) 21st-Century Applications of Nanodiamonds. *Optics and Photonics News*, 21 (9), pp. 20-25.
 - 16 Doherty, M., Dolde, F., Fedder, H., Jelezko, F., Wrachtrup, J., Manson, N. and Hollenberg, L. (2012) Theory of the ground-state spin of the NV⁻ center in diamond. *Physical Review B*, 85 (20), pp. 205203.
 - 17 Manson, N., Harrison, J. and Sellars, M. (2006) Nitrogen-vacancy center in diamond: Model of the electronic structure and associated dynamics. *Physical Review B*, 74 (10), pp. 104303.
 - 18 Fuchs, G., Dobrovitski, V., Hanson, R., Batra, A., Weis, C., Schenkel, T. and Awschalom, D. (2008) Excited-state spectroscopy using single spin manipulation in diamond. *Physical Review Letters*, 101 (11), pp. 117601.
 - 19 N.B. Manson, J.P. Harrison, *Diam. Relat. Mater.* 14 (2005) Photo-ionization of the nitrogen-vacancy center in diamond. *Diamond and Related Materials*, 14
 - 20 Fu, C.C., Lee, H.Y., Chen, K., Lim, T.S., Wu, H.Y., Lin, P.K., Wei, P.K., Tsao, P.H., Chang, H.C. and Fann, W. (2007) Characterization and application of single fluorescent

-
- nanodiamonds as cellular biomarkers. *Proceedings of the National Academy of Sciences of the United States of America*, 104 (3), pp. 727-732.
- 21 Wu, T., Tzeng, Y., Chang, W., Cheng, C., Kuo, Y., Chien, C., Chang, H. and Yu, J. (2013) Tracking the engraftment and regenerative capabilities of transplanted lung stem cells using fluorescent nanodiamonds. *Nature Nanotechnology*, 8 (9), pp. 682-689.
 - 22 Schirhagl, R., Chang, K., Loretz, M. and Degen, C.L. (2014) Nitrogen-vacancy centers in diamond: nanoscale sensors for physics and biology. *Annual Review of Physical Chemistry*, 65, pp. 83-105.
 - 23 Gali, A., Janzén, E., Deák, P., Kresse, G. and Kaxiras, E. (2009) Theory of Spin-Conserving Excitation of the N-V-Center in Diamond. *Physical Review Letters*, 103 (18), pp. 186404.
 - 24 Childress, L. and Hanson, R. (2013) Diamond NV centers for quantum computing and quantum networks. *MRS Bulletin*, 38 (02), pp. 134-138.
 - 25 Neumann, P., Kolesov, R., Jacques, V., Beck, J., Tisler, J., Batalov, A., Rogers, L., Manson, N., Balasubramanian, G. and Jelezko, F. (2009) Excited-state spectroscopy of single NV defects in diamond using optically detected magnetic resonance. *New Journal of Physics*, 11 (1), pp. 013017.
 - 26 J.A. Weil, J.R. Bolton and J.E. Wertz, *Electron Paramagnetic Resonance: Elementary Theory and Application*. Chapman & Hall, 3rd edition, 1994.
 - 27 Balasubramanian, G., Chan, I.Y., Kolesov, R., Al-Hmoud, M., Tisler, J., Shin, C., Kim, C., Wojcik, A., Hemmer, P.R., Krueger, A., Hanke, T., Leitenstorfer, A., Bratschitsch, R., Jelezko, F. and Wrachtrup, J. (2008) Nanoscale imaging magnetometry with diamond spins under ambient conditions. *Nature*, 455 (7213), pp. 648-651.
 - 28 Jelezko, F. and Wrachtrup, J. (2006) Single defect centres in diamond: A review. *Solid State Physics (a)*, 203 (13), pp. 3207-3225.
 - 29 Rieger, P.H. (2007) *Electron spin resonance: analysis and interpretation*. Royal Society of Chemistry.

-
- 30 Gaebel, T., Domhan, M., Popa, I., Wittmann, C., Neumann, P., Jelezko, F., Rabeau, J.R., Stavrias, N., Greentree, A.D. and Prawer, S. (2006) Room-temperature coherent coupling of single spins in diamond. *Nature Physics*, 2 (6), pp. 408-413.
 - 31 Jelezko, F. and Wrachtrup, J. (2005) Read- Out of Single Spins by Optical Spectroscopy. *ChemInform*, 36 (2), pp. no-no.
 - 32 Woollam, J. A., Beale, H. A., & Spain, I. L. (2003). Bi₂Se₃ Hall effect magnetometer for reliable low temperature use. *Review of Scientific Instruments*, 44(4), 434-437.
 - 33 Romalis, M. V., & Dang, H. B. (2011). Atomic magnetometers for materials characterization. *Materials today*, 14(6), 258-262
 - 34 Kleiner, R., Koelle, D., Ludwig, F. and Clarke, J. (2004) Superconducting quantum interference devices: state of the art and applications. *Proceedings of the IEEE*, 92 (10), pp. 1534-1548.
 - 35 Rayleigh, L. (1896). XV. on the theory of optical images, with special reference to the microscope. *The London, Edinburgh, and Dublin Philosophical Magazine and Journal of Science*, 42(255), 167-195.
 - 36 Sidles, J. A., Garbini, J. L., Bruland, K., Rugar, D., Züger, O., Hoen, S., et al. (1995). Magnetic resonance force microscopy. *Reviews of Modern Physics*, 67(1), 249.
 - 37 Züger, O., & Rugar, D. (1993). First images from a magnetic resonance force microscope. *Applied Physics Letters*, 63(18), 2496-2498.
 - 38 Rondin, L., Tetienne, J., Spinicelli, P., Dal Savio, C., Karrai, K., Dantelle, G., Thiaville, A., Rohart, S., Roch, J. and Jacques, V. (2012) Nanoscale magnetic field mapping with a single spin scanning probe magnetometer. *Applied Physics Letters*, 100 (15), pp. 153118.
 - 39 Chao, S., Dougherty, W. M., Garbini, J. L., & Sidles, J. A. (2004). Nanometer-scale magnetic resonance imaging. *Review of Scientific Instruments*, 75(5), 1175-1181.

-
- 40 Davies, J. (1976) Optically-detected magnetic resonance and its applications. *Contemporary Physics*, 17 (3), pp. 275-294.
- 41 Chernobrod, B. M., & Berman, G. P. (2004). Spin microscope based on optically detected magnetic resonance. *Journal of Applied Physics*, 97(1), 014903.
- 42 Grinolds, M. S., Hong, S., Maletinsky, P., Luan, L., Lukin, M. D., Walsworth, R. L., & Yacoby, A. (2013). Nanoscale magnetic imaging of a single electron spin under ambient conditions. *Nature Physics*, 9(4), 215-219.
- 43 Taylor, J.M. (2011) High-sensitivity diamond magnetometer with nanoscale resolution. *Nature physics*, 7 (3), pp. 270.
- 44 Babinec, T.M., Hausmann, B.J., Khan, M., Zhang, Y., Maze, J.R., Hemmer, P.R. and Lončar, M. (2010) A diamond nanowire single-photon source. *Nature nanotechnology*, 5 (3), pp. 195-199
- 45 Maletinsky, P., Hong, S., Grinolds, M.S., Hausmann, B., Lukin, M.D., Walsworth, R.L., Loncar, M. and Yacoby, A. (2012) A robust scanning diamond sensor for nanoscale imaging with single nitrogen-vacancy centres. *Nature nanotechnology*, 7 (5), pp. 320-324.
- 46 Degen, C. (2008) Scanning magnetic field microscope with a diamond single-spin sensor. *Applied Physics Letters*, 92 (24), pp. 243111.
- 47 Kuhn, S., Hettich, C., Schmitt, C., Poizat, J. & Sandoghdar, V. Diamond colour centres as a nanoscopic light source for scanning near-field optical microscopy. *J. Microsc.* 202, 2–6 (2001).
- 48 Cuche, A., Drezet, A., Sonnefraud, Y., Faklaris, O., Treussart, F., Roch, J. and Huant, S. (2009) Near-field optical microscopy with a nanodiamond-based single-photon tip. *Optics express*, 17 (22), pp. 19969-19980.
- 49 Cuche, A., Roch, J., Huant, S., Treussart, F. and Drezet, A. (2010) Grafting fluorescent nanodiamonds onto optical tips. *Journal of Nanophotonics*, 4 (1), pp. 043506-043506-6.

-
- 50 Karrai, K. and Grober, R.D. (1995) Piezoelectric tip-sample distance control for near field optical microscopes. *Applied Physics Letters*, 66 (14), pp. 1842-1844.
- 51 Schröder, T., Schell, A.W., Kewes, G., Aichele, T. and Benson, O. (2010) Fiber-integrated diamond-based single photon source. *Nano letters*, 11 (1), pp. 198-202.
- 52 Schröder, T., Fujiwara, M., Noda, T., Zhao, H., Benson, O. and Takeuchi, S. (2012) A nanodiamond-tapered fiber system with high single-mode coupling efficiency. *Optics Express*, 20 (10), pp. 10490-10497.
- 53 Pham, L.M., Le Sage, D., Stanwix, P.L., Yeung, T.K., Glenn, D., Trifonov, A., Cappellaro, P., Hemmer, P., Lukin, M.D. and Park, H. (2011) Magnetic field imaging with nitrogen-vacancy ensembles. *New Journal of Physics*, 13 (4), pp. 045021.
- 54 Rabeau, J., Reichart, P., Tamanyan, G., Jamieson, D., Prawer, S., Jelezko, F., Gaebel, T., Popa, I., Domhan, M. and Wrachtrup, J. (2006) Implantation of labelled single nitrogen vacancy centers in diamond using ^{15}N . *Applied Physics Letters*, 88 (2), pp. 023113-023113-3.
- 55 Budker, D., & Romalis, M. (2007). Optical magnetometry. *Nature Physics*, 3(4), 227-234.
- 56 Acosta, V. M., Bauch, E., Ledbetter, M. P., Santori, C., Fu, K. M., Barclay, P. E., ... & Budker, D. (2009). Diamonds with a high density of nitrogen-vacancy centers for magnetometry applications. *Physical Review B*, 80(11), 115202.
- 57 Balasubramanian, G., Neumann, P., Twitchen, D., Markham, M., Kolesov, R., Mizuochi, N., Isoya, J., Achard, J., Beck, J. and Tissler, J. (2009) Ultralong spin coherence time in isotopically engineered diamond. *Nature materials*, 8 (5), pp. 383-387.
- 58 Yamamoto, T., Umeda, T., Watanabe, K., Onoda, S., Markham, M., Twitchen, D., Naydenov, B., McGuinness, L., Teraji, T. and Koizumi, S. (2013) Extending spin coherence times of diamond qubits by high-temperature annealing. *Physical Review B*, 88 (7), pp. 075206.

-
- 59 Lai N D, Zheng D, Jelezko F, Treussart F and Roch J-F 2009 Influence of a static magnetic field on the photoluminescence of an ensemble of nitrogen–vacancy color centers in a diamond single-crystal *Appl. Phys. Lett.* 95 133101
- 60 Rogers, L., McMurtrie, R., Sellars, M. and Manson, N. (2009) Time-averaging within the excited state of the nitrogen-vacancy centre in diamond. *New Journal of Physics*, 11 (6), pp. 063007.
- 61 Martin, J., Manson, N., Doetschman, D., Sellars, M., Neuhaus, R. and Wilson, E. (2000) Spectral hole burning and Raman heterodyne signals associated with an avoided crossing in the NV centre in diamond. *Journal of Luminescence*, 86 (3), pp. 355-362.
- 62 Tetienne, J., Rondin, L., Spinicelli, P., Chipaux, M., Debuisschert, T., Roch, J. and Jacques, V. (2012) Magnetic-field-dependent photodynamics of single NV defects in diamond: an application to qualitative all-optical magnetic imaging. *New Journal of Physics*, 14 (10), pp. 103033.
- 63 www.oxxius.com
- 64 1. O’Shea Donald C. 1985 *Elements of Modern Optical Design* (John Wiley & Sons, Inc) Chapter 7 General
- 65 thorlabs.de
- 66 Lan, G., Banerjee, P. and Mitra, S. (1981) Raman scattering in optical fibers. *Journal of Raman Spectroscopy*, 11 (5), pp. 416-423.
- 67 Wardle, D. (1999) *Raman scattering in optical fibres*
- 68 Flusberg, B.A., Cocker, E.D., Piyawattanametha, W., Jung, J.C., Cheung, E.L. and Schnitzer, M.J. (2005) Fiber-optic fluorescence imaging. *Nature methods*, 2 (12), pp. 941-950.
- 69 www.keithley.com

-
- 70 Wang, L., Choi, H.Y., Jung, Y., Lee, B.H. and Kim, K. (2007) Optical probe based on double-clad optical fiber for fluorescence spectroscopy. *Optics express*, 15 (26), pp. 17681-17689.
- 71 Roland Albrecht's thesis, internal
- 72 Fujii, T., Taguchi, Y., Saiki, T. and Nagasaka, Y. (2011) A fusion-spliced near-field optical fiber probe using photonic crystal fiber for nanoscale thermometry based on fluorescence-lifetime measurement of quantum dots. *Sensors*, 11 (9), pp. 8358-8369.
- 73 Ma, X., Liu, D., Zhang, F. and Yan, Y. (2007) Non-polarizing broadband dichroic mirror. *Journal of Optics A: Pure and Applied Optics*, 9 (7), pp. 573.
- 74 Saiki, T. and Matsuda, K. (1999) Near-field optical fiber probe optimized for illumination–collection hybrid mode operation. *Applied Physics Letters*, 74 (19), pp. 2773-2775.
- 75 Jorge, P., Martins, M.A., Trindade, T., Santos, J.L. and Farahi, F. (2007) Optical fiber sensing using quantum dots. *Sensors*, 7 (12), pp. 3489-3534.
- 76 Ōsawa, E. (2008) Monodisperse single nanodiamond particulates. *Pure and Applied Chemistry*, 80 (7), pp. 1365-1379.
- 77 www.newport.com , 'Lens collection and systems throughput'
- 78 Balaji, J., Garai, K., Chakrabarti, S. and Maiti, S. (2003) Axial resolution limit of a fiber-optic fluorescence probe. *Applied Optics*, 42 (19), pp. 3780-3784.
- 79 Utzinger, U., & Richards-Kortum, R. R. (2003). Fiber optic probes for biomedical optical spectroscopy. *Journal of Biomedical Optics*, 8(1), 121-147.
- 80 Wasserman, S., Snir, M., Dodiuk, H. and Kenig, S. (1988) Transmission and Mechanical Properties of Optical Adhesives. , pp. 667.
- 81 Lu, B., Zheng, S., Quach, B.Q. and Tai, Y. (2010) A study of the autofluorescence of parylene materials for μ TAS applications. *Lab on a Chip*, 10 (14), pp. 1826-1834.

-
- 82 Piruska, A., Nikcevic, I., Lee, S.H., Ahn, C., Heineman, W.R., Limbach, P.A. and Seliskar, C.J. (2005) The autofluorescence of plastic materials and chips measured under laser irradiation. *Lab on a Chip*, 5 (12), pp. 1348-1354.
- 83 C V Horie *Materials for Conservation* page 90 'film formation from solution'
- 84 Dréau, A., Lesik, M., Rondin, L., Spinicelli, P., Arcizet, O., Roch, J. F., & Jacques, V. (2011). Avoiding power broadening in optically detected magnetic resonance of single NV defects for enhanced dc magnetic field sensitivity. *Physical Review B*, 84(19), 195204.
- 85 www.xbitlabs.com
- 86 www.lintech.org/comp-per/10HDDISK.pdf
- 87 Krüger, A., Kataoka, F., Ozawa, M.a.a., Fujino, T., Suzuki, Y., Aleksenskii, A., Vul, A.Y. and Ōsawa, E. (2005) Unusually tight aggregation in detonation nanodiamond: identification and disintegration. *Carbon*, 43 (8), pp. 1722-1730.
- 88 Note: Fabrication of tapered fibre tip using mechanical polishing method. (2011) *Review of scientific instruments*, 82, pp. 086115.
- 89 Fujiwara, M., Toubaru, K., Noda, T., Zhao, H. and Takeuchi, S. (2011) Highly efficient coupling of photons from nanoemitters into single-mode optical fibers. *Nano letters*, 11 (10), pp. 4362-4365.